



Dissertation

Multiscale Modelling of Advanced Hard Magnets (Mehrskalenmodellierung moderner Hartmagnete)

Ausgeführt zum Zwecke der Erlangung des akademischen Grades eines

Doktors der technischen Wissenschaften

unter der Leitung von

Univ. Prof. Dipl.-Ing. Dr. techn. Josef Fidler

Institut für Festkörperphysik / E138

eingereicht an der Technischen Universität Wien

Fakultät für Physik

von

Peter Toson, MSc

Matrikelnummer 1228967

Rotenhofgasse 21 / Hof 1

1100 Wien

Wien, am 04.11.2015

Peter Toson

Erklärung zur Verfassung der Arbeit

Peter Toson, MSc
Rotenhofgasse 21 / Hof 1
1100 Wien

Hiermit erkläre ich, dass ich diese Arbeit selbstständig verfasst habe, dass ich die verwendeten Quellen und Hilfsmittel vollständig angegeben habe und dass ich die Stellen der Arbeit – einschließlich Tabellen, Karten und Abbildungen –, die anderen Werken oder dem Internet im Wortlaut oder dem Sinn nach entnommen sind, auf jeden Fall unter der Angabe der Quelle als Entlehnung kenntlich gemacht habe.

Ort, Datum

Peter Toson, MSc

Kurzfassung

Hartmagnetische Materialien haben zahlreiche Anwendungen in Alltagsgeräten, in der Medizin, in der Energietechnik, sowie in der Elektronik und Spintronik. Die Seltene-Erd-Magnete zeichnen sich durch ausgezeichnete intrinsische Eigenschaften (magnetokristalline Anisotropie, Sättigungsmagnetisierung) aus, die zu hohen Koerzitivfeldern, Remanenzen und Energiedichteprodukten führen. Das kurz- und langfristige Angebotsrisiko der Seltenen Erden, speziell der schweren Seltenen Erden wie Dy und Tb, motivieren die Suche nach Methoden zur Reduktion des Seltenen-Erd-Anteils oder nach komplett Seltenen-Erd-freien Alternativen.

Das Ziel des geförderten europäischen ROMEO Forschungsprojektes war es, die magnetischen Eigenschaften von $\text{Nd}_2\text{Fe}_{14}\text{B}$ Magneten ohne Zusatz von schweren Seltenen-Erd Elementen wie Dy, Tb durch Optimierung der Kornstruktur und der Korngrenzen zu verbessern. Das Ziel des REFREPERMAG Projektes war die Suche nach neuen, Seltenen-Erd-freien magnetischen Phasen und die Entwicklung nanostrukturierter Magnete auf Eisen und Kobalt-Basis.

Im Rahmen dieser Dissertation wurden für beide Projekte Simulationen durchgeführt, um die theoretischen Grenzen dieser Ansätze zu beleuchten und Voraussagen der endgültigen Materialeigenschaften zu machen. Die hier vorgestellten Ergebnisse lieferten so einen wesentlichen Beitrag für den Erfolg dieser Forschungsprojekte und wurden in wissenschaftlichen Fachzeitschriften publiziert.

Diese Dissertation beschreibt einen Mehrskalen-Ansatz der computergestützten Materialentwicklung. Die intrinsischen Materialeigenschaften von Seltenen-Erd-freien Alternativen wurden auf Basis der Dichtefunktionaltheorie (DFT) berechnet. Mithilfe der DFT kann der Ursprung der intrinsischen Eigenschaften verstanden und Vorschläge zur Verbesserung bestehender oder neuartiger Materialien gemacht werden, zum Beispiel durch Optimierung des c/a Verhältnisses.

Die uniaxiale magnetokristalline Anisotropie-Energie für $(\text{Fe}_{0.6}\text{Co}_{0.4})_2\text{B}$ beträgt $1.4\text{MJ}/\text{m}^3$ obwohl die Anisotropie der Legierungen Fe_2B und Co_2B planar ist. Die Temperaturabhängigkeit der Anisotropie von MnBi wurde berechnet und die Anisotropie kann mit einem c/a Verhältnis von 1.375 optimiert werden ($2.0 - 2.3\text{MJ}/\text{m}^3$, abhängig von der Größe der Einheitszelle).

Die intrinsischen Eigenschaften aus den DFT Berechnungen dienen als Eingabe für die mikromagnetischen Simulationen. Simulationen basierend auf der Finiten

Element Methode von realistischen Korn- und Nanostrukturen wurden durchgeführt, um die inkohärenten Ummagnetisierungsprozesse und deren Auswirkungen auf die makroskopischen Hysterese-Eigenschaften zu berechnen.

Der erste Teil der mikromagnetischen Simulationen dient der Optimierung von $\text{Nd}_2\text{Fe}_{14}\text{B}$ Magneten, die mit dem Schmelzschleuderverfahren (melt spinning) hergestellt wurden. Basierend auf den Ergebnissen von TEM Untersuchungen in der Literatur wurden Finite Element-Modelle von realistischen Kornstrukturen mit Hilfe eines eigens implementierten Algorithmus erstellt. Simulationen von Korn- und Plättchenstrukturen mit unterschiedlicher Größe, Materialparametern in Körnern und Korngrenzen und unterschiedlichen Verteilungen der leichten Richtungen in den hartmagnetischen Körnern wurden durchgeführt.

Die Ergebnisse zeigen, dass die indirekte Kopplung der Körner über ferro- und para-magnetische Korngrenzen verantwortlich für die Reduktion der Koerzitivität gegenüber dem Anisotropiefeld ist (Brown'sches Paradox). Durch die Entkopplung der Körner mit nicht-magnetischen Korngrenzen könnten die Hysterese-Eigenschaften von $\text{Nd}_2\text{Fe}_{14}\text{B}$ Magneten bedeutend verbessert werden. Mit ferro- bzw. paramagnetischen Korngrenzen erreicht das Koerzitivfeld 25% bzw. 36% des Anisotropiefeldes, mit nichtmagnetischen Korngrenzen könnte dieser Wert auf 72% erhöht werden.

Der zweite Teil der mikromagnetischen Simulationen beschäftigt sich mit dem Aufbau von nanostrukturierten Magneten mit Nanoteilchen. Mikromagnetische Simulationen von isolierten, zylindrischen Nanoteilchen wurden durchgeführt um ihre Form und Seitenverhältnis zu optimieren. Der zweite Schritt ist die Simulation von zwei interagierenden Nanoteilchen um die Auswirkungen des magnetostatischen Austauschs auf die Hysterese-Eigenschaften zu untersuchen. Ein Modell von perfekt ausgerichteten Nanoteilchen (Matrix-Modell) wurde erstellt, um die theoretischen Grenzen (Koerzitivfeld, Energiedichteprodukt) von nanostrukturierten Magneten zu erforschen.

Ein Algorithmus basierend auf Gravitation und Kollisionskräften wurde entwickelt, um mikromagnetische Modelle von realistisch gepackten Nanoteilchenstrukturen zu erstellen. Die Auswirkungen von Misorientierung und Packungsdichte auf das Koerzitivfeld, die Remanenz und das Energiedichteprodukt wurden untersucht. Beide Modelle – Matrix-Modelle und gepackte Strukturen – beschreiben experimentell herstellbare Nanostrukturen: Regelmäßige Matrizen können mit Elektro-Deposition

von hartmagnetischen Materialien in porösen Aluminiumoxid-Schablonen hergestellt werden; gepackte Strukturen beschreiben die Verdichtung von Nanoteilchen-Pulver, dass mittels Nasschemie-Synthese hergestellt wurde. Die Simulationsergebnisse von beiden Modellen stimmen gut mit den experimentell gemessenen Werten überein. Energiedichteprodukte von bis zu 200 kJ/m^3 können erreicht werden, ein 5-fach höherer Wert verglichen zu konventionellen Hartferriten (40 kJ/m^3)

Abstract

Permanent magnetic materials are found in many everyday devices and have applications in medicine, energy engineering and microsensoric and spintronic devices. The rare-earth $\text{Nd}_2\text{Fe}_{14}\text{B}$ alloy has outstanding intrinsic properties (magnetocrystalline anisotropy, saturation magnetization) leading to high coercive fields and energy density products. However, rare earths, especially heavy rare earths such as Dy and Tb, are under high short- and long-term supply risk. The search for rare-earth lean or free alternatives is therefore of great scientific and economic interest.

The goal of the European funded ROMEO research project was the improvement of $\text{Nd}_2\text{Fe}_{14}\text{B}$ magnets without heavy rare-earth elements (Dy, Tb) by optimizing the grain structure and grain boundary engineering. The REFREEMAG project searched for novel, rare-earth free magnetic phases and developed nanostructured permanent magnets on iron and cobalt basis.

In the course of this thesis, simulations have been performed for both projects in order to explore the theoretical limits of these approaches and to predict the properties of the final materials. The results presented in this work provided an essential contribution to the success of the two research projects and have been published in scientific journals.

This thesis describes a multiscale approach to computational material design. Density functional theory (DFT) calculations on rare-earth free candidate materials have been performed in order to obtain the intrinsic material properties. DFT is a valuable tool to understand the origin of the intrinsic properties and is able to give guidelines to improve existing or novel materials, for example by optimization of the tetragonal distortion (c/a ratio).

The uniaxial magnetocrystalline anisotropy energy of $(\text{Fe}_{0.6}\text{Co}_{0.4})_2\text{B}$ is $1.4 \text{ MJ}/\text{m}^3$, although the Fe_2B and Co_2B alloys have negative anisotropy energies describing in-plane anisotropy. The temperature dependence of anisotropy of MnBi has been calculated and the anisotropy is optimized by a c/a ratio of 1.375 reaching values between 2.0 and $2.3 \text{ MJ}/\text{m}^3$, depending on the unit cell volume.

The obtained intrinsic properties act as input for micromagnetic simulations. Simulations based on the finite element method have been performed on realistic

grain and nanostructures in order to calculate the incoherent reversal processes leading to the macroscopically observed hysteresis properties.

The first part of micromagnetic simulations is about grain structure optimization of melt-spun $\text{Nd}_2\text{Fe}_{14}\text{B}$ magnets. Based on the results of TEM studies found in literature, an algorithm that creates finite element models realistic grain / grain boundary structures has been implemented. Micromagnetic simulations have been performed on grain and platelet structures with varying grain size, grain and grain boundary properties and easy axis distribution in the hard magnetic grains.

The results show that the indirect coupling of grains over ferro- and paramagnetic grain boundaries reduces the coercive field significantly and causes Brown's paradox. The simulations show that decoupling the grains with non-magnetic grain boundaries would increase the coercivity of $\text{Nd}_2\text{Fe}_{14}\text{B}$ magnets substantially. With ferro- and paramagnetic grain boundaries the coercive field reaches 25% and 36% of the anisotropy field, respectively. This value is increased to 72% with non-magnetic grain boundaries.

The second part of micromagnetic simulations describes a bottom-up approach to create composite nanostructured permanent magnets. Micromagnetic simulations on single, cylindrical nanorods have been performed to optimize the shape and aspect ratio. In a second step, the magnetostatic interactions and between nanorods and their influence on the coercivity have been examined. A model of regular nanorod arrangements has been created to explore the theoretical limits of coercivity and energy density product in nano-composite magnets.

A packing algorithm based on gravity and collision forces has been implemented to create models of realistically packed nanorods in order to examine the losses in remanence, coercivity and energy density product due to the misalignment and packing of nanorods.

Both models describe structures an experimental production route. Regular nanorod matrices are created by electrodeposition of the magnetic material in a porous aluminium oxide template. Irregularly packed nanorods are produced by compaction of nanorod powder synthesized with a wet chemistry process. The simulation results of both models are in good agreement with experimental measurements. Energy density products of up to 200 kJ/m^3 are obtained, a five-fold increase compared to conventional hard ferrites (40 kJ/m^3)

Acknowledgments

The financial support of the European Commission's Seventh Framework Programme under grand no. 280670 (REFREEPERMAG [141]) and 309729 (ROMEO [140]) is acknowledged. The computational results presented have been achieved by using the Vienna Scientific Cluster VSC-2.

I want to thank the following Open Source and Freeware tools:

- The L^AT_EX[30, 31] distribution *MiKTeX* [143],
- the GUI *TeXnicCenter* [56],
- the crystal structure tool *VESTA* [95],
- the Voronoi solver *voro++* [84],
- the *bullet physics library* [101],
- the pre- and post-processing platform *Salome* [80] and
- the visualization software *ParaView* [134].

Contents

1. Introduction	1
1.1. Motivation	1
1.2. Permanent Magnetism	3
1.3. Overview of Permanent Magnetic Materials	6
2. Theoretical Background	8
2.1. Density Functional Theory	8
2.1.1. From the Schrödinger to the Kohn-Sham Equation	8
2.1.2. The Wien2k Package	10
2.2. Magnetic Energies	13
2.2.1. Zeeman Energy	13
2.2.2. Exchange Energy	13
2.2.2.1. Calculating Exchange Stiffness with Wien2k	14
2.2.3. Magnetocrystalline Anisotropy Energy	15
2.2.3.1. Phenomenological Description	15
2.2.3.2. Microscopic Origin of Magnetocrystalline Anisotropy	19
2.2.3.3. Calculating Anisotropy Energies with Wien2k	20
2.2.4. Magnetostatic Interaction and Shape Anisotropy	22
2.3. Finite Element Micromagnetics	24
2.3.1. Static and Dynamic Micromagnetism	24
2.3.2. Finite Element Method	26
2.3.2.1. Weak Formulation	26
2.3.2.2. Basis Functions	26
2.3.2.3. Constructing a System of Linear Equations	28
3. DFT Calculations of Hard Magnetic Phases	31
3.1. MnAl	31
3.1.1. The L10 structure	31
3.1.2. Results and Discussion	32
3.2. LTP MnBi	35
3.2.1. MnBi at 0K	37
3.2.1.1. Lattice Parameters	37
3.2.1.2. Magnetocrystalline anisotropy	37
3.2.2. Magnetic Moments	37

3.2.3.	Temperature Dependence of MAE	38
3.2.4.	Conclusion	38
3.3.	Fe-Co-B	40
3.3.1.	Binary alloys	40
3.3.2.	Virtual Crystal Approximation	42
3.3.3.	Results	43
4.	Microstructural Optimization of Nd-Fe-B Magnets	46
4.1.	Introduction	46
4.2.	Micromagnetic Modelling	47
4.2.1.	Experimental Input and Dimensioning	47
4.2.2.	Model Creation	48
4.3.	Results and Discussion	51
4.3.1.	Grains without Grain Boundary	51
4.3.1.1.	Perfect Exchange Coupling	51
4.3.1.2.	Influence of Grain Size	53
4.3.2.	Grains with Grain Boundary	53
4.3.3.	Platelets with and without Grain Boundary	55
4.3.4.	Microstructural Parameter Analysis	56
4.3.5.	Importance of Magnetocrystalline Anisotropy	59
4.4.	Conclusion	60
5.	Micromagnetic Modelling of Nanostructured Permanent Magnets	61
5.1.	Single Nanorods	61
5.1.1.	Analytical Considerations	61
5.1.1.1.	Coherent Rotation	61
5.1.1.2.	Curling and Buckling	63
5.1.2.	Micromagnetic Simulations	65
5.1.3.	Influence of Aspect Ratio	68
5.2.	Regular Nanorod Arrangements	70
5.2.1.	Magnetostatic Interaction Between Nanorods	70
5.2.2.	Influence of Packing Density	72
5.2.3.	Using Novel Materials	75
5.3.	Irregularly Packed Nanorods	78
5.3.1.	Model Creation	78
5.3.1.1.	Packing of Nanorods	78

5.3.1.2. Meshing	80
5.3.2. Results and Discussion	84
5.4. Thermal Stability	90
5.5. Further Optimization	92
5.5.1. Optimizing the Nanorod Shape	92
5.5.2. Magnetic Hardening with Antiferromagnetic Caps	93
5.5.2.1. Micromagnetic Model	94
5.5.2.2. Results and Discussion	94
6. Conclusion	99
A. List of Figures	i
B. List of Tables	iii
C. References	iv

1. Introduction

1.1. Motivation

Many everyday devices contain permanent magnets: cars, hard disc drives, loudspeakers, and microphones. Besides that, permanent magnets have a wide range of applications in medicine and industry: magnetic resonance imaging (MRI), motors, sensors, and power generators [92]. The global market for permanent magnets is estimated at USD 15.1 billion in 2013 and is expected to increase to USD 22.9 billion in 2018 with a compound annual growth rate of 8.7% [122]. 9% of the global magnet production are rare-earth magnets, but they generate 65% of the global revenue. However, rare earths, especially heavy rare earths like Dy and Tb, are under a high short- and long-term supply risk [98]. The search for ways to reduce the usage of rare-earths in permanent magnets or completely rare-earth free alternatives is therefore of great scientific and economic interest.

The macroscopic magnetic properties highly depend on the crystalline micro-structure [32, 97]. By optimizing the micro-structure it is possible to improve the magnetic properties of rare earth magnets without the need of heavy rare earth dopants [129]. Micromagnetic simulations on realistic grain structures based on TEM investigations [29, 35, 132] have been performed in order to give guidelines to create optimal grain structures. In addition, ab-initio calculations on rare-earth free alternatives have been performed.

Nano-structured materials are an interesting candidate to produce rare-earth free permanent magnets [99, 104, 114]. A possible prototype are structures of elongated cylindrical Co nanorods with the crystallographic c axis parallel to the long cylinder axis. The idea is to exploit both magnetocrystalline and shape anisotropy to increase the coercive field.

There are several possible ways to optimize this material. The magnetic properties of a single nanorod are optimized by tuning diameter, height and aspect ratio. It is possible to seal the nanorods' tips with an antiferromagnetically coupled material with high uniaxial anisotropy. Optimizing the shape of the tips reduce the demagnetizing field and prevent nucleation.

After a single nanorod has been optimized, the interactions between nanorods have been examined. The most simple model consists of two parallel nanorods to study

the influence of the distance between the nanorods on the coercivity. There are two production routes for nanorods leading to different structures: Regular matrices of nanorods are produced by filling alumina templates with Co via electrodeposition [96, 111]. Irregular arrangements of nanorods are created by packing and aligning nanostructured powder created by a polyol process [85, 120].

In this work, finite element micromagnetics has been utilized to model all of the mentioned structures to optimize the geometric properties and to predict the resulting macroscopic magnetic properties. Another, drastically different approach is the use of novel materials in the nano structure. The intrinsic magnetic properties such as magnetocrystalline anisotropy and saturation magnetisation have been calculated ab-initio calculations based on the density functional theory (DFT). The results from the atomistic DFT calculations act as input for the mesoscopic micromagnetic simulations leading to a multi-scale approach in computational material design (see fig. 1).

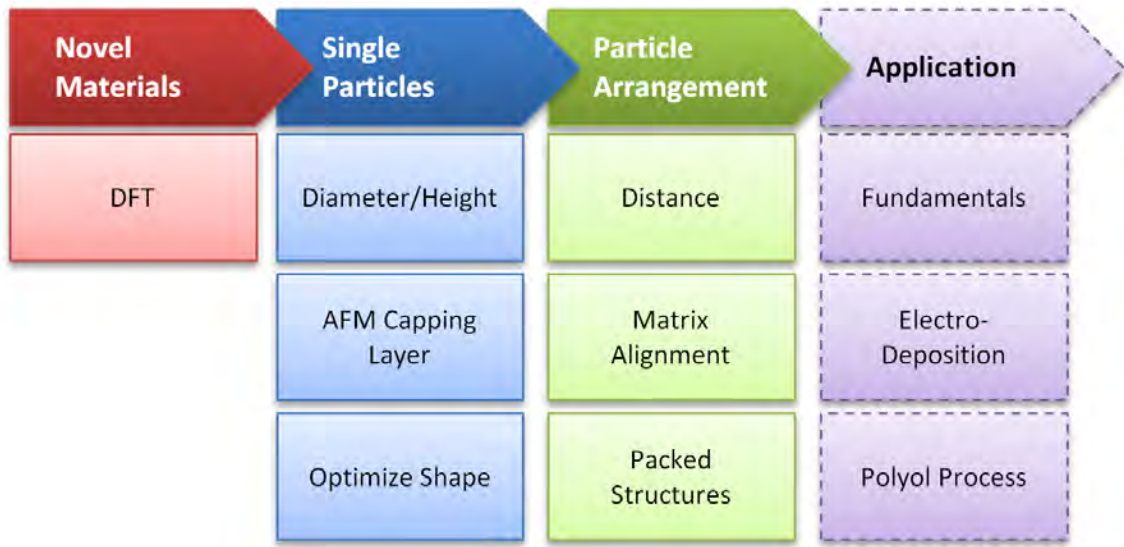


Fig. 1: Multiscale computational material design of nano-structured permanent magnets

1.2. Permanent Magnetism

Ferromagnetic materials can store their own magnetization M or polarization $J = \mu_0 M$ and create their own persistent magnetic field. The most important tool to characterize permanent magnets is the hysteresis loop. The M - H (or J - H) loop plots the magnetization (or polarization) over the external magnetic field H_{ext} . It is also common to plot the total magnetic flux density $B = \mu_0 H + J$ through the magnet over the external field (B - H loop).

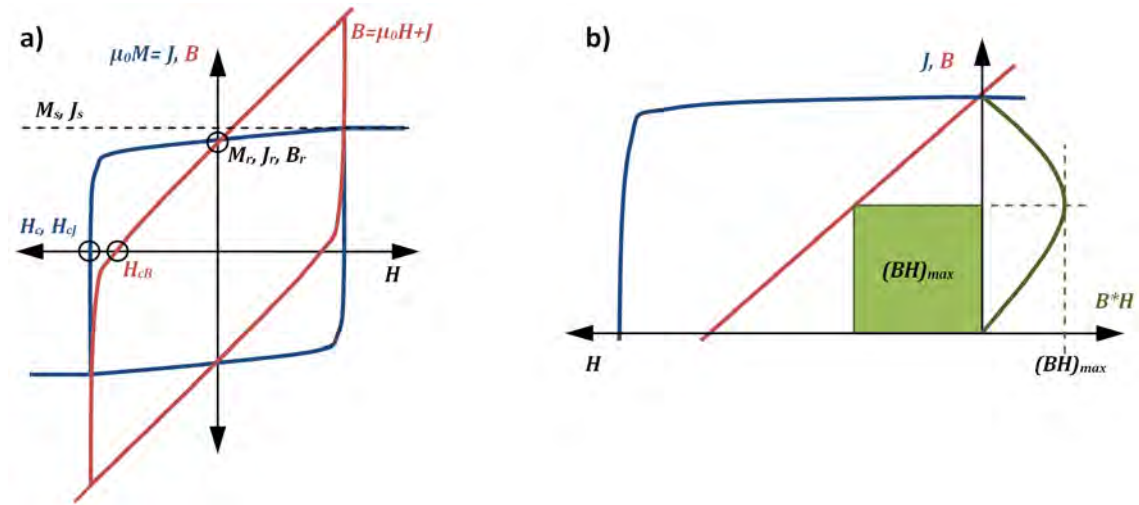


Fig. 2: (a) Characteristic points on the M - H and B - H loop. (b) Calculation of the energy density product $(BH)_{max}$

Characteristic points in the hysteresis loop are (see fig. 2a)

- M_s saturation magnetization, the highest magnetization induced in the magnet with the help of an external field
- J_s : saturation polarization, analogous to M_s
- M_r : remanence magnetization, the remaining magnetization in the magnet without an magnetic field
- J_r, B_r : remanence polarization, analogous to M_r . Because the external field is zero at the remanent point, the remanence polarization is equivalent to the remanence flux density
- H_c, H_{cJ} : coercive field, the external field that is necessary to demagnetize the magnet. More formally, the point where the mean magnetization parallel to the external field direction is zero.

- H_{cB} : coercive field that is necessary to set the total flux density through the magnet to zero

Soft magnetic materials have a narrow hysteresis loop (small coercivity) and are used in transformers to keep the losses in the magnet low. Permanent or hard magnetic materials have high coercivity and are able to retain their magnetization even in external fields directed opposite to the magnetization. The energy density product $(BH)_{max}$ describes the ability of a magnetic material to store magnetic energy and be calculated from the hysteresis loop (see fig 2b). A high energy density product is important for high performance applications such as power generation and electro motors, but also for miniaturization because with high energy density products it is possible to store the same magnetic energy in a smaller magnet (loudspeakers, hard disk drives, microsensoric devices). Assuming perfectly rectangular hysteresis loops, an estimation of the maximum possible energy product is given by:

$$(BH)_{max}^{theo} = \frac{J_s^2}{4\mu_0} = \frac{\mu_0 M_s^2}{4} \quad (1.1)$$

It is possible to refine the formula if H_c and B_r are known [123, 147]. The dependence of the energy density product on the coercivity given by equation (1.2) is shown in fig. 3.

$$(BH)_{max} \approx \begin{cases} B_r^2/4\mu_0 & \text{if } \mu_0 H_c \geq B_r/2 \\ (B_r - \mu_0 H_c)H_c & \text{if } \mu_0 H_c \leq B_r/2 \end{cases} \quad (1.2)$$

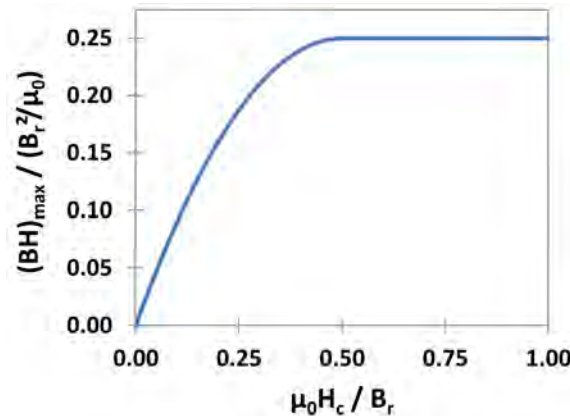


Fig. 3: Dependence of the theoretical energy density product $(BH)_{max}$ on the coercive field H_c expressed as function of the remanence B_r

Magnetic materials have a preferred direction of magnetization, the so-called easy axis. Because this effect is caused by the crystal structure of the material it is called magnetocrystalline anisotropy. The magnetocrystalline anisotropy is described by one or multiple anisotropy constants $K_1 \dots K_n$. For further information on the definition of the anisotropy constants, see chapter 2.2.3.

Stoner and Wohlfarth analytically calculated the coercivity of magnetic materials based on the intrinsic properties J_s and K_1 by assuming an ellipsoidal, single domain particle and coherent rotation as reversal mechanism [9, 10]. The key finding is the anisotropy field

$$H_A = \frac{2K_1}{J_s} \quad (1.3)$$

as measure of the coercivity. Considering the demagnetizing field (chapter 2.2.4) of an elongated particle, the coercivity is expressed by

$$H_c = \frac{2K_1}{J_s} - (N_{\parallel} - N_{\perp}) \cdot M_s \quad (1.4)$$

Stoner and Wolfarth also calculated the dependence of the *switching* field H_{sw} on the angle θ between easy axis and external field

$$H_{sw} = \frac{(1 - t^2 + t^4)^{1/2}}{1 + t^2} \quad \text{with} \quad t = \tan^{1/3} \theta \quad (1.5)$$

In literature, the terms switching field and coercive field are often used interchangeably [81, 116], there is a subtle difference: The coercive field is the field where the magnetization is zero, the switching field is the field where the "jump" in magnetization occurs (more formally, the field where the derivative dM/dH is maximal). While the two definitions lead to equal fields for low misorientation angles θ , for $\theta > 45^\circ$ the switching field is higher than the coercive field (see fig. 4).

Due to the idealized conditions assumed in the Stoner-Wohlfarth model, the anisotropy field H_A is referred as the upper theoretical limit of coercivity in literature. The coercivity of sintered magnets is typically limited to 40% of the anisotropy field (Brown's Paradox) [105]. This is also confirmed by micromagnetic simulations of grain structures (chapter 4). However, chapter 5 shows that it is possible to compensate this loss with the shape anisotropy term $(N_{\parallel} - N_{\perp})M_s$ and

that coercivities higher than the anisotropy field are realized in both theory and experiment.

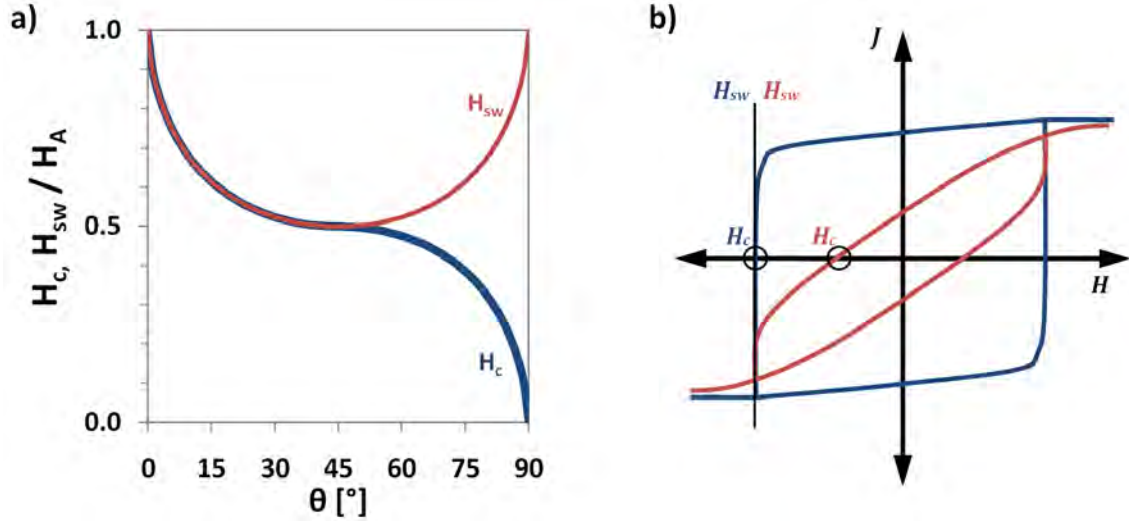


Fig. 4: (a) Angular dependance of switching field H_{sw} and coercive field H_c according to the Stoner-Wohlfarth model. (b) Two hysteresis loops with the same switching field, but different coercive fields

1.3. Overview of Permanent Magnetic Materials

The oldest known magnetic materials are so-called lodestones (naturally magnetised magnetite Fe_3O_4) and have been described by antique Greece, India and China. Iron and its oxides have been the only known magnetic material for a long time. The development of magnetic steels have coined the terms *hard* and *soft magnetic* because of the higher coercivity of the mechanically hard steels compared to the softer pure iron [105]. A more formal definition of hard and soft magnetic materials is based on the coercive field: hard or permanent magnets have coercivities above 250mT ; soft magnets have coercivities in the order of 1mT or below [81].

Most ferrites have a low saturation magnetization due to the metal-oxide bonds and a low magnetocrystalline anisotropy because of the cubic crystal structure. Hexagonal hard ferrites are an exception and are cheap but moderately performing permanent magnets. Hard ferrites have a $MO \cdot 6\text{Fe}_3\text{O}_4$ (sum formula $M\text{Fe}_{12}\text{O}_{19}$) structure where M is a metal, usually Sr or Ba. The non-magnetic MO oxides build a hexagonally closed packed lattice. The magnetic smaller iron oxides are

placed in the interstitial positions of the hexagonal MO lattice, leading to a high magnetocrystalline anisotropy [54].

Another class of magnetic materials with high magnetocrystalline anisotropy are alloys with a tetragonal $L1_0$ structure. In the 1930s, FePt and CoPt magnets have been discovered and had the best permanent magnetic properties available until the 1950s. These platinum alloys are very expensive but are also highly corrosion resistant and are still commonly used in magnetic recording. A newer compound with $L1_0$ structure is MnAl. The MnAl $L1_0$ phase metastable and some carbon is added during production to stabilize the phase [88, 107].

AlNiCo magnets are based on the Mishima alloy ($Fe_{0.58}Ni_{0.30}Al_{0.12}$, discovered in 1931) which showed surprisingly high coercivity. The addition of Co, Cu and Ti increased the coercivity and energy density product further. The microstructure of AlNiCo magnets consist of elongated hard magnetic, FeCo-rich precipitates embedded in a soft magnetic, AlNi-rich phase. The coercivity of AlNiCo magnets is not based magnetocrystalline anisotropy, but on the shape anisotropy of the hard magnetic precipitates [15, 105].

In the 1940s elongated single domain particles (ESD) of Fe, Co and FeCo have been successfully synthesized and pressed to permanent magnets under the commercial name *Lodex*. Historically, the later discovery of rare-earth permanent magnets based on $SmCo_5$ and $Nd_2Fe_{14}B$ (see intrinsic properties in table 1) made the comparatively expensive ESD production unattractive. The supply shortage of rare earth metals in 2011 caused the funding of research programs to reduce the rare-earth content in permanent magnets and to develop rare-earth free alternatives. The rare-earth free nano-structured magnets discussed in this thesis are based on ESD magnets.

Structure	Material	$K_1[MJ/m^3]$	$J_s[T]$	$A[pJ/m]$	$T_C[K]$	Ref.
hcp	Co	0.45	1.76	13	1360	[82]
$L1_0$	FePt	6.60	1.43	11	750	[59]
$L1_0$	CoPt	4.90	1.01	10	840	[105]
$L1_0$	MnAl	1.70	0.70	10	650	[59]
AuCu	MnBi	0.90	0.73	12	633	[105]
	$BaFe_{12}O_{19}$	0.33	0.48	6	740	[105]
	$SmCo_5$	17.20	1.07	12	1020	[105]
	$Nd_2Fe_{14}B$	4.90	1.61	8	588	[105]

Table 1: Intrinsic Properties of Hard Magnetic Materials with Uniaxial Anisotropy

2. Theoretical Background

This chapter is not meant to give a complete, in-depth description of density functional theory (DFT), micromagnetism and numerical methods, as it would go far beyond the scope of this thesis. Rather, section 2.1.1 tries to motivate why DFT calculations are used and to give a general idea how the Wien2k code works. Section 2.2 is the link between the ab-initio and the micromagnetic world and explains with examples how the intrinsic material parameters that act as input for micromagnetic simulations are calculated by DFT methods. Section 2.3 introduces the Landau-Lifshitz-Gilbert equation and explains the way from differential equations to a set of linear equations.

Sing and Nordström [77] wrote a great introduction into the LAPW method and the official Wien2k guide by Blaha et al. [60] is a thorough reference for Wien2k users. The micromagnetic energy terms and their atomistic origin are explained by Skomski [81]. For the implementation of finite element element micromagnetics, see references [55, 68, 78].

2.1. Density Functional Theory

2.1.1. From the Schrödinger to the Kohn-Sham Equation

In order to calculate the intrinsic magnetic properties, the electronic structure of the magnetic material has to be calculated by solving the Schrödinger equation for each electron. The most basic form is the stationary free electron Schrödinger equation [2]:

$$\left(-\frac{\hbar^2}{2m_e} \nabla^2 + V(r) \right) \Psi = E \Psi \quad (2.1)$$

In crystalline solids, the potential $V(r)$ is periodic ($V(r) = V(r + T)$ with a translation vector T) which means that it is enough to consider a single unit cell when calculating the electronic structure. Under a periodic potential, the electrons' wave functions are Bloch Functions in the form

$$\Psi(r) = e^{ikr} \cdot u(r) \quad (2.2)$$

with a lattice-periodic function $u(r) = u(r + T)$ and a phase factor e^{ikr} [3]. Every wave vector k has a corresponding wave vector in the first Brillouin zone: $k = k + G$ with the reciprocal lattice vector G [25].

A further common approximation is the distinction between core and valence electrons. The core electrons are considered as a part of the potential $V(r)$ and the Schrödinger equation is only solved for the valence electrons. For iron (two Fe atoms per unit cell) this reduces the number of electrons from 52 to 16. Considering crystal symmetries this number is reduced to 8 because the two Fe atoms are equivalent.

While 8 electrons seems a manageable number, there are two problems. Firstly there are many magnetic materials with a higher number of atoms per unit cell than iron ($\text{Nd}_2\text{Fe}_{14}\text{B}$ for example) and secondly, the many-electron problem cannot be solved *exactly* due to the interaction between the electrons [4].

This is where the density functional theory (DFT) comes in. Hohenberg and Kohn showed that the total energy of a many-electron system is a functional of a continuous electron density ρ [18]:

$$E_{tot} = \int V(r) \rho(r) \cdot dr + F[\rho] \quad (2.3)$$

Kohn and Sham refined the functional by splitting it into the kinetic energy T_0 , the influence of the external potential $V(r)$, the Coulomb repulsion between the electrons and the exchange correlation functional E_{xc} [19]:

$$E_{tot} = T_0[\rho] + \int V(r) \rho(r) \cdot dr + \frac{1}{2} \int \frac{\rho(r)\rho(r')}{|r' - r|} \cdot dr' dr + E_{xc}[\rho] \quad (2.4)$$

This leads to the Kohn-Sham equation, a Schrödinger-esque equation on the continuous electron density. The Kohn-Sham equation is an eigenvalue problem to find the energy ε_i for each Kohn-Sham orbital φ_i

$$\left(-\frac{\hbar^2}{2m_e} \nabla^2 + V_{eff}(r) \right) \varphi_i = \varepsilon_i \varphi_i \quad (2.5)$$

The Kohn-Sham equation has to be solved in a self-consistent manner. Based on an initial guess of the electron density ρ the effective potential V_{eff} has to be calculated.

Solving the Kohn-Sham equation with the potential V_{eff} yields the eigenvalues ε_i and eigenfunctions φ_i . The new electron density is given by

$$\rho = \sum_i |\varphi_i|^2 \quad (2.6)$$

This electron density acts as input for a new cycle until self-consistency is reached.

2.1.2. The Wien2k Package

Wien2k is a full-potential, linearised augmented plane wave code [60] that solves the self-consistency problem (2.5). Wien2k decomposes the space into non-overlapping atomic spheres and an interstitial region (see fig. 5). Inside the spheres the full atomic potential is taken into account - inclusive the $1/r^2$ singularity. This singularity causes many oscillations of the atomic functions and are difficult to converge. The advantage of full-potential calculations over faster solvable pseudo-potential methods is the higher precision of the results [60, 77, 136] (see fig. 6).

In the interstitial region the potential is nearly constant which means that the wave functions are plane waves. At the border of the the atomic spheres, the plane waves are augmented in order to create a continuous transition between atomic wave functions and the plane waves.

By default, the Wien2k code treats the core states fully relativistic and takes scalar relativistic effects for the valence states into account. Relativistic effects such as spin-orbit coupling and orbital contraction in heavier elements are treated within the framework of the perturbation theory on a fully converged scalar-relativistic calculation.

Although the density functional theory is analytically proven to be exact, the exact form of the exchange correlation functional $E_{xc}[\rho]$ in equation (2.4) is still unknown [77]. Wien2k offers multiple approximations for this functional. The simplest functional is the Local Density Approximation (LDA) in the form of

$$E_{xc}[\rho] \approx E_{xc}^{LDA} = \int \rho(r) \varepsilon_{xc}[\rho(r)] \cdot dr \quad (2.7)$$

The functional $\varepsilon_{xc}[\rho(r)]$ of a free electron gas is proportional to $\rho(r)^{1/3}$, Wien2k uses a more sophisticated LDA functional formulated by Perdew and Wang [40].

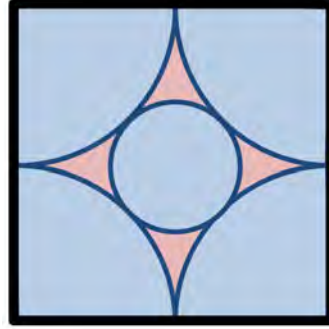


Fig. 5: Decomposition of the unit cell into touching spheres (blue) and an interstitial region (red)

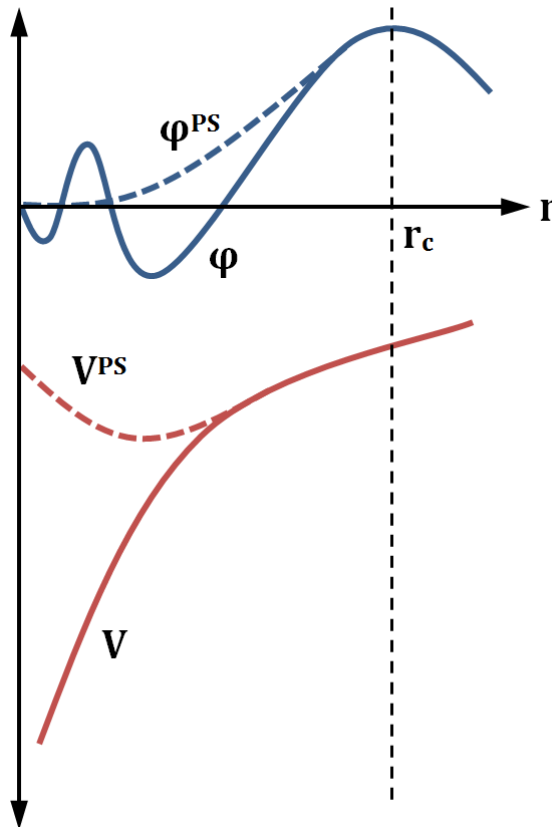


Fig. 6: The pseudo-potential V^{PS} is a good approximation of the full potential V outside the core radius r_c but eliminates the $1/r^2$ singularity. The resulting wave functions φ^{PS} are in good agreement with all-electron wave functions outside r_c but show no oscillations near the core.

Another important class of exchange correlation functionals are the Generalized Gradient Approximations (GGA) which take not only the electron density but also its derivative into account:

$$E_{xc}[\rho] \approx E_{xc}^{GGA} = \int \rho(r) F[\rho(r), \nabla \rho(r)] \cdot dr \quad (2.8)$$

There are multiple GGA functionals implemented in Wien2k, Blaha et al. [60] recommend the formulation of Perdew, Burke and Ernzerhof (PBE-GGA [47]) as well-balanced, general purpose GGA.

The Wien2k package allows the ab-initio calculation of mechanical, optical and magnetic properties of crystalline solids. In this thesis, the focus lies on the calculation of intrinsic magnetic properties that act as input for the micromagnetic simulations, summarized in chapter 3:

- the saturation magnetization M_s (magnetic moment per unit cell volume)
- the exchange stiffness constant A (see examples in section 2.2.2.1, p. 14)
- the magnetocrystalline anisotropy energy, a measure of the anisotropy constant K_1 (method explained in section 2.2.3.3, p. 20)

Another common application is the calculation of the ferromagnetic Curie temperature T_C (for example in [117]).

2.2. Magnetic Energies

2.2.1. Zeeman Energy

The Zeeman energy is the energy of a magnetic moment \mathbf{m} in an external field \mathbf{H} and is given by

$$E_Z = -\mu_0 \cdot \mathbf{m} \cdot \mathbf{H} \quad (2.9)$$

The Zeeman energy is minimal, if the moment is aligned parallel to the external field and has a maximum, if the moment is aligned antiparallel to the external field. This causes the Zeeman split of spin-up and spin-down electron energies with $E = \pm \mu_0 \mu_B H$. The macroscopic Zeeman energy is calculated by summation of the energies per moment or by an volume integral over a continuous magnetization $\mathbf{M} = \frac{1}{V} \sum \mathbf{m}$:

$$E_Z = -\mu_0 \int \mathbf{M}(\mathbf{r}) \mathbf{H}(\mathbf{r}) \cdot dV \quad (2.10)$$

2.2.2. Exchange Energy

The most fundamental mechanism to explain spontaneous magnetization and ferromagnetism is the exchange interaction between spins. According to the Heisenberg model, the exchange energy E_{ex} is expressed as

$$E_{ex} = -\frac{1}{2} \sum_{i \neq j} J_{ij} \cdot \mathbf{s}_i \cdot \mathbf{s}_j \quad (2.11)$$

where J_{ij} is the exchange integral between the electron spins \mathbf{s}_i and \mathbf{s}_j . The spin configuration depends on the sign of the exchange integral: If J_{ij} is positive, the spins are aligned parallel (ferromagnetic configuration) and if J_{ij} is negative, the spins are aligned antiparallel (antiferromagnetic configuration). If $J_{ij} = 0$, there is no exchange between spins which corresponds to para- or diamagnetic materials.

Although the exchange integrals are anisotropic, the exchange energy is approximated by a single, isotropic exchange stiffness constant A in continuum theory:

$$E_{ex} = A \int (\nabla \cdot \mathbf{s})^2 \cdot dV \quad (2.12)$$

The exchange energy term is minimized, if the magnetisation is homogenous and the divergence is zero in the whole volume.

2.2.2.1. Calculating Exchange Stiffness with Wien2k

The macroscopic exchange stiffness has been determined with DFT calculations. The energy difference between a non-magnetic (MN) and a spin-polarized (SP) configuration is the energy gain due to the exchange interaction: $E_{ex} \approx E_{SP} - E_{MN}$. The exchange integrals are approximated with the exchange stiffness: $J_{ij} \approx A \cdot r_{ij}$, where r_{ij} is the distance between the spins \mathbf{s}_i and \mathbf{s}_j . Substituting these approximations into the Heisenberg exchange and solving for A yields

$$A = 2 (E_{SP} - E_{MN}) \cdot \left(\sum_{i \neq j} r_{ij} \cdot \mathbf{s}_i \cdot \mathbf{s}_j \right)^{-1} \quad (2.13)$$

Name	bcc Fe
Space Group	229 Im-3m
a, b, c	2.860 Å
α, β, γ	90°

Atom	Wyckoff	x	y	z
Fe	2a	0	0	0

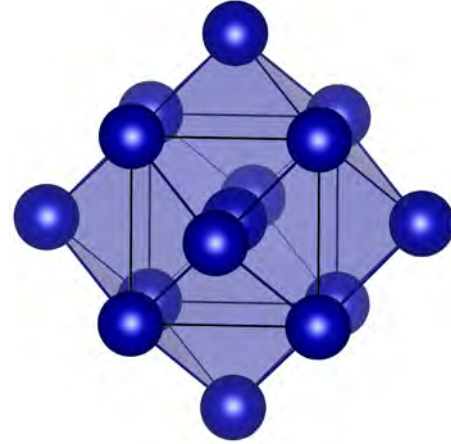


Fig. 7: Lattice parameters, unit cell and atomic environment of bcc Fe

The Wien2k calculations have been performed with 10.000 k-points and the general gradient approximation in the formulism of Perdew, Burke and Ernzerhof (PBE-GGA) as exchange correlation potential. The non-magnetic case has been initialized with `init_lapw -numk 10000` and the self-consistency cycle has been performed with the `run_lapw` script with a convergence criterion of $10^{-9} Ry$. The spin-polarized

configuration has been initialized with `init_lapw -numk 10000` and calculated with the `runsp_lapw` script [60].

The energy difference between non-magnetic and spin-polarized case is $41.4mRy$. The unit cell consists of two equivalent Fe atoms. The atomic environment consists of 14 Fe atoms: 8 at a distance $r_{ij} = 2.477 \text{ \AA}$ and 6 at a distance $r_{ij} = 2.860 \text{ \AA}$ forming a rhombic dodecahedron (see fig 7). Because all spin moments are aligned parallel, all scalar products $\mathbf{s}_i \mathbf{s}_j$ equal +1. The resulting exchange stiffness is $A = 24.4pJ/m$ which is in good agreement with the experimentally measured value $A = 22pJ/m$ [105].

Name	hcp Co
Space Group	194 $P6_3/mmc$
a, b	2.505 \AA
c	4.070 \AA
α, β	90°
γ	120°

Atom	Wyckoff	x	y	z
Co	2c	$1/3$	$2/3$	$1/4$

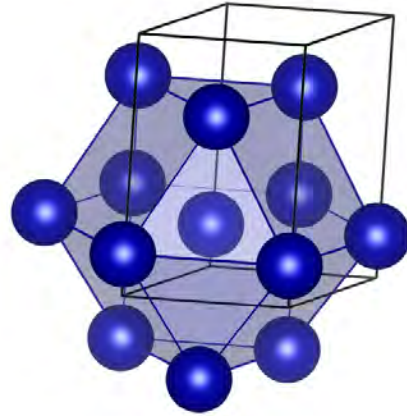


Fig. 8: Lattice parameters, unit cell and atomic environment of hcp Co

The hcp Co unit cell also consists of two equivalent atoms. The atomic environment consists of 6 atoms at a distance $r_{ij} = 2.497 \text{ \AA}$ and 6 atoms at $r_{ij} = 2.505 \text{ \AA}$ forming an anticuboctahedron. The energy difference between non-magnetic and spin-polarized configuration is $37.7mRy$, corresponding to an exchange stiffness of $A = 27.4pJ/m$, experimental values range from 9.9 to $31.0pJ/m$ [59, 105].

2.2.3. Magnetocrystalline Anisotropy Energy

2.2.3.1. Phenomenological Description

Magnetocrystalline anisotropy describes the effect that the energy of a magnet depends on the direction of magnetization with respect to the crystallographic axes. The magnetocrystalline anisotropy is described by anisotropy constants $K_1 \dots K_n$ which are in the order of $10kJ/m^3$ (bcc Fe) to $10MJ/m^3$ (rare-earth permanent

magnets). The exact definition of the anisotropy constants depends on the crystal system. The simplest model to describe this energy difference is uniaxial anisotropy

$$\frac{E_A}{V} = K_1 \sin^2 \theta + K_2 \sin^4 \theta + \dots \quad (2.14)$$

where θ is the polar angle of the magnetisation measured from the crystallographic c axis. The exact anisotropy type depends on the sign of K_1 and K_2 . If both constants are positive the system has an easy axis (the c axis), if both constants are negative the system has an easy plane (the ab plane). For cases with mixed signs the ratio of K_1 to K_2 decide whether the resulting anisotropy is easy axis, easy plane, or easy cone (see fig. 9).

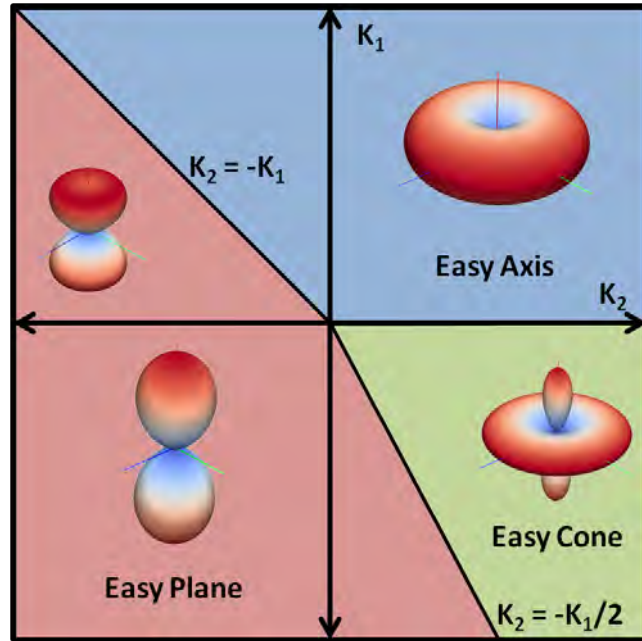


Fig. 9: Anisotropy type depending on the uniaxial anisotropy constants K_1 and K_2 . The inlays show typical energy surfaces.

The uniaxial anisotropy constants K_1 and K_2 are usually accurate enough to describe the anisotropy of hexagonal and tetragonal crystal systems, but they cannot describe an anisotropy in the basal plane. For basal plane anisotropy, a sixth order term in the form

$$\begin{aligned}
& K_{3,hex} \cdot \sin^6 \theta \cdot \cos 6\varphi \\
& \quad \text{or} \\
& K_{3,tet} \cdot \sin^6 \theta \cdot \cos 4\varphi
\end{aligned} \tag{2.15}$$

must be introduced, where φ is the azimuth angle of the magnetization measured from the crystallographic a axis.

For cubic systems it is convenient to use an other definition for the anisotropy constants:

$$\frac{E_A}{V} = K_1 (\alpha^2 \beta^2 + \alpha^2 \gamma^2 + \beta^2 \gamma^2) + K_2 (\alpha^2 \beta^2 \gamma^2) \tag{2.16}$$

where α, β, γ are the direction cosines of the normalized magnetization direction. It is possible to transform the spherical coordinates θ and φ to the direction cosines α, β, γ :

$$\begin{aligned}
\alpha &= \sin \theta \cdot \cos \varphi \\
\beta &= \sin \theta \cdot \sin \varphi \\
\gamma &= \cos \theta
\end{aligned} \tag{2.17}$$

Fig. 10 visualizes the energy surfaces of a single positive and negative K_1 and K_2 terms. If K_1 is positive, the $\langle 100 \rangle$ axes are easy and $\langle 111 \rangle$ axes are hard and vice-versa for negative K_1 values. The $\langle 110 \rangle$ axes are intermediate axes in both cases. If K_2 is positive, the system has 3 easy planes (ab , ac , bc) and hard $\langle 111 \rangle$ axes. If K_2 is negative the $\langle 111 \rangle$ axes are easy and $\langle 100 \rangle$ and $\langle 110 \rangle$ are equally hard axes. Depending on the sign and ratio of K_1 and K_2 all permutations of $\langle 100 \rangle$, $\langle 110 \rangle$, $\langle 111 \rangle$ and easy, intermediate and hard axis are possible (see fig. 11)

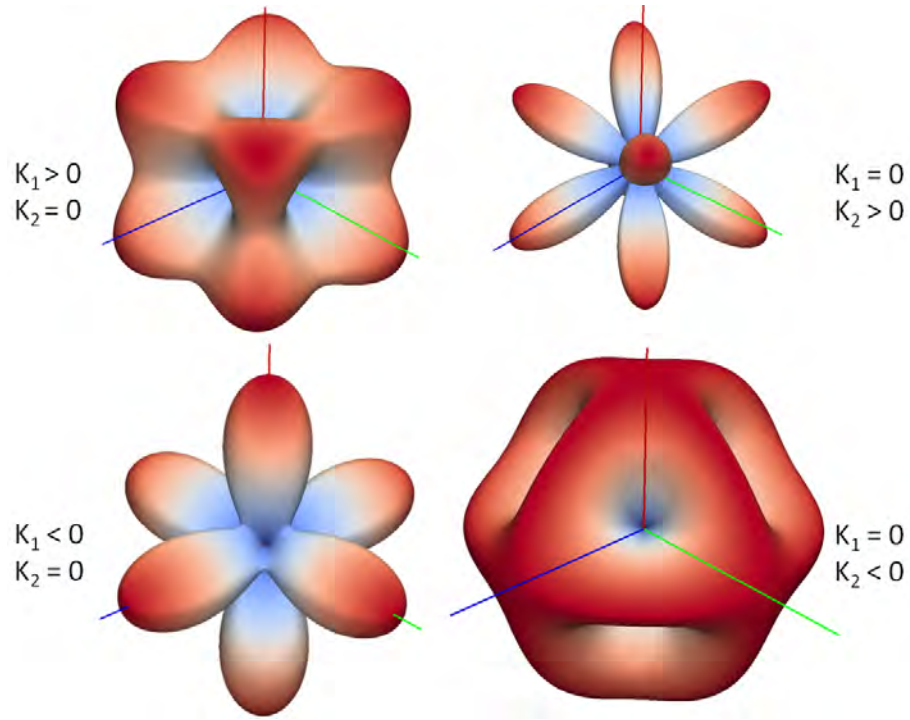


Fig. 10: Energy surfaces for positive and negative cubic anisotropy constants K_1 and K_2

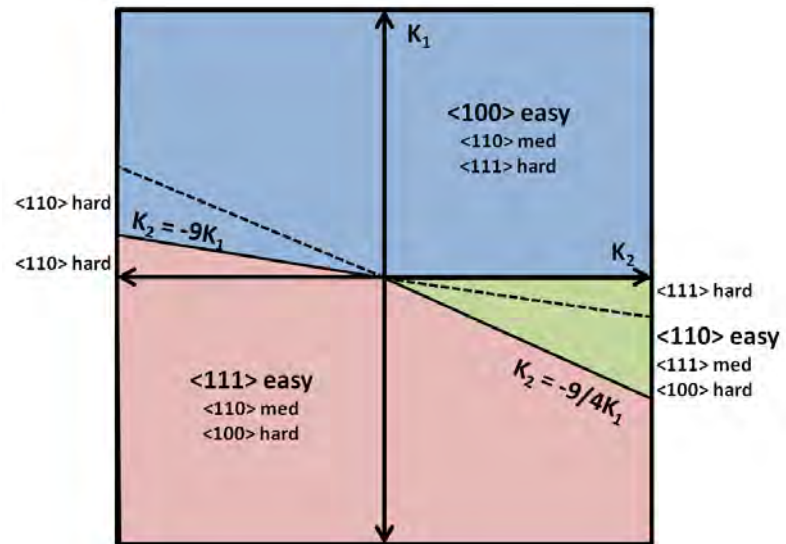


Fig. 11: Easy, intermediate and hard axes in dependence on the cubic anisotropy constants K_1 and K_2

An important quantity derived from the anisotropy constants is the anisotropy field H_A

$$H_A = \frac{2K_1}{J_s} \quad (2.18)$$

The anisotropy field equals the coercive field of an ideal single domain particle with coherent rotation. In practice, only coercivity values between 1% (for as-cast materials) and 40% (highly optimised sintered and annealed magnets) of the anisotropy field are realized (Brown's Paradox). This discrepancy is explained with local nucleations and an inhomogeneous magnetization reversal modes.

The inclusion of higher order anisotropy terms leads to the saturation field H_{sat}

$$H_{sat} = \frac{2 (K_1 + K_2 + \dots)}{J_s} \quad (2.19)$$

which equals the external field necessary to saturate the magnet in the hard direction. However, the coercivity of an ideal uniaxial magnet does not depend on higher-order terms and H_A remains a valid approximation for coercivity.

2.2.3.2. Microscopic Origin of Magnetocrystalline Anisotropy

Magnetocrystalline anisotropy is a consequence of two competing effects: spin-orbit coupling and crystal field interaction. Classically speaking, the spin-orbit coupling is caused by the orbital movement of the electrons around the nucleus. This movement creates a magnetic field which interacts with the electron's spin. However, the movement of the electron is impaired by the crystal field of neighbouring nuclei. In fact, for delocalized d electrons in transition metals the orbital movement is fully quenched and the electrons oscillate in the energy valleys of the crystal field potential. Localized f electrons (rare earths) are not influenced by the crystal field and are able to orbit the nucleus freely. [38]

In free space, all d orbitals have the same energy, but the crystal field splits the energies based on the symmetry of the orbitals - the so-called $e_g - t_{2g}$ split. In a primitive cubic lattice the orbitals pointing directly to a neighbour (e_g symmetry: $x^2 - y^2$, z^2) are energetically unfavourable due to the electrostatic repulsion from neighbouring negative charges. The orbitals with t_{2g} symmetry (xy , yz , xz)

point between the neighbours have lower energy. It is possible that these energy levels are further split by a tetragonal distortion of the lattice, an external field (Zeeman split) or spin-orbit coupling (see fig. 12). These energy splits are the reason that different magnetization directions have different energies and cause the macroscopically observed magnetocrystalline anisotropy. [81]

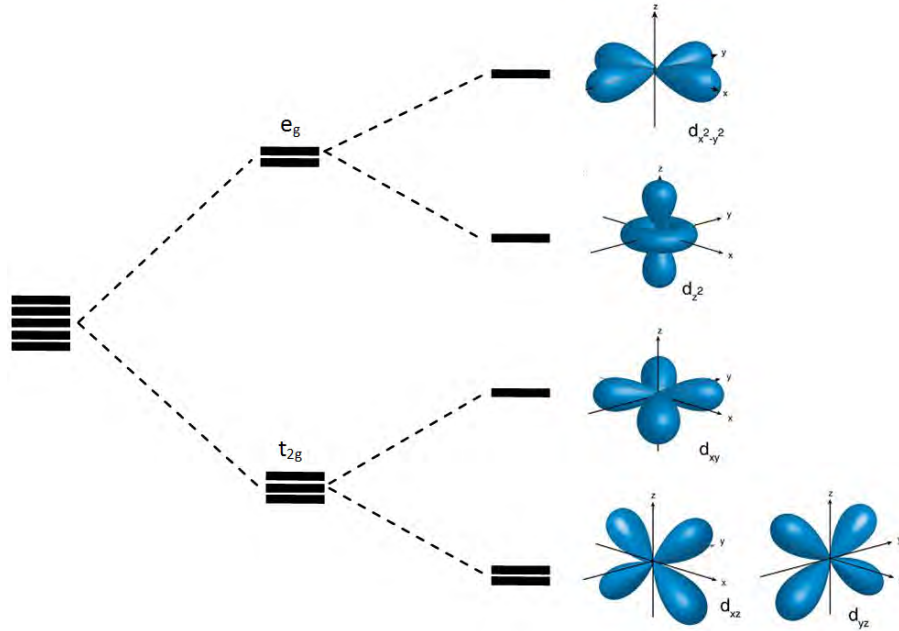


Fig. 12: e_g and t_{2g} split of d orbitals due to crystal field interaction. The energy levels are further split by tetragonal distortion, external fields or spin-orbit coupling

2.2.3.3. Calculating Anisotropy Energies with Wien2k

Because the spin-orbit coupling yields a small perturbation from the total energy, the spin-orbit coupling should be performed on a fully converged spin-polarized calculation. [57, 117, 136, 144]

Technically, the spin-orbit coupling is initialized with the interactive `initso_lapw` script. Because the spin-orbit coupling breaks the symmetry, the script generates a new `*.struct` file with fewer symmetry operations and a lower space group [60].

For example, bcc Fe has a highly symmetric crystal structure and four symmetry operations are shown in fig. 13: three mirror planes (xy, yz, xz) and the 3 fold rotation axis [111]. Adding a magnetization direction breaks some symmetries:

with magnetisation along $[100]$ or $[001]$ the rotation around $[111]$ and mirroring at planes normal to the magnetisation direction are disallowed. The resulting structures are equivalent (they have the same number and type of symmetries) but differ in the exact symmetry operations. With magnetization along $[111]$ all mirror planes are broken, but the rotation around $[111]$ is still allowed.

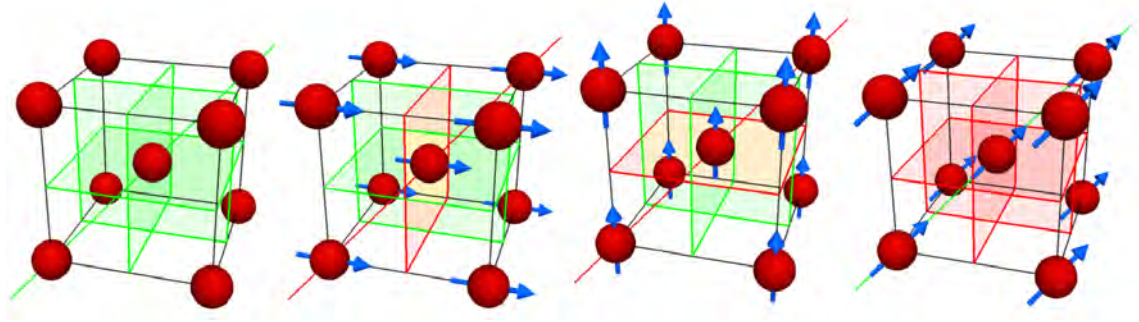


Fig. 13: Symmetry breaking in a bcc crystal due to magnetization directions.

There are multiple strategies to account for the symmetry breaking due to different magnetization directions. The labels *initso_111*, *initso_one* and *initso_all* will be used for quick reference throughout this thesis, but are by no means official names. It is recommended to state the magnetisation direction used for the symmetry breaking and/or the resulting space group in publications.

initso_111 is a popular choice for structures with low symmetry. The idea is to call `initso_lapw` only once for magnetization along the hard axis because that breaks the most symmetry operations. After that, the same structure is used for all magnetization directions and the direction is only changed in the `*.inso` file. However, breaking symmetry by the hard axis does not necessarily break all symmetries for the easy directions (e.g. high-symmetry structures like bcc Fe)

initso_one is the methodically cleanest approach. The spin-polarized calculation is copied multiple times and in each copy the script `initso_lapw` is called once for the different magnetization directions. The advantage is that each direction is calculated with the correct symmetry operations while maintaining the maximum possible symmetry. However, the resulting structures for different directions may have different space groups. This has to be kept in mind while analyzing the results.

initso_all breaks all symmetries by multiple calls of **initso_lapw**. Each subsequent call of **initso_lapw** with a different direction will remove additional allowed symmetry operations. Calling **initso_lapw** for the directions [001], [100], [110] and [111] on a bcc structure will break all symmetry operations except identity and inversion symmetry while keeping all symmetries defined by space group 229 (Im-3m). The same low-symmetry structure is used for all magnetisation directions by changing the direction in the ***.inso** file. The advantage of this method is that the same structure with the lowest common dominator of symmetry operations is consistently used for all magnetization directions. The disadvantage is that higher computational time because of the reduction of symmetry. Due to the higher degrees of freedom the calculation is more difficult to converge and may for some cases even diverge.

Table 2 summarizes the calculation of the magnetocrystalline anisotropy of bcc Fe with different initialisation methods (see fig. 7 in 2.2.2.1 for lattice parameters). All calculations yield the correct magnetic moments, but only **initso_one** and **initso_all** predict the anisotropy correctly (experimental value: $K_1 = 45 - 48 \text{ kJ/m}^3$ $K_2 = 5 - 15 \text{ kJ/m}^3$). Due to the wrong handling of symmetry breaking of the **initso_111** method, the magnetocrystalline anisotropy is an order of magnitude wrong and fails to predict the cubic nature of the anisotropy ($\text{MAE}_{[100]-[001]} \neq 0$)

	initso_111	initso_one	initso_all
$\mu_{Fe} [\mu_B]$	2.22	2.22	2.22
$J_s [T]$	2.217	2.217	2.217
$\text{MAE}_{[100]-[001]} [kJ/m^3]$	-1760	0	0
$\text{MAE}_{[110]-[001]} [kJ/m^3]$	-216	15	18
$\text{MAE}_{[111]-[001]} [kJ/m^3]$	-636	37	30

Table 2: Calculated magnetocrystalline anisotropy energies for bcc Fe.

2.2.4. Magnetostatic Interaction and Shape Anisotropy

The shape anisotropy is based on the long-range dipolar interaction of magnetic moments. The magnetostatic interaction energy for each pair of moments $\mathbf{m}_{i,j}$ at the position $\mathbf{r}_{i,j}$ is given by

$$E_{MS}(i, j) = -\frac{1}{4\pi\mu_0} \cdot \frac{3 \cdot \mathbf{m}_i \mathbf{R}_{ij} \cdot \mathbf{m}_j \mathbf{R}_{ij} - R_{ij}^2 \cdot \mathbf{m}_i \mathbf{m}_j}{R_{ij}^5} \quad (2.20)$$

with $\mathbf{R}_{ij} = \mathbf{r}_i - \mathbf{r}_j$. The total magnetostatic energy is calculated by summation over each pair of magnetic dipoles. In continuum theory the summation over magnetic moments is replaced by an integration of magnetisation over volume. A further simplification is the introduction of an effective self-interaction or demagnetizing field \mathbf{H}_D :

$$E_{MS} = \frac{\mu_0}{2} \cdot \int \mathbf{M}(\mathbf{r}) \cdot \mathbf{H}_D(\mathbf{r}) \cdot dV \quad (2.21)$$

For general cases the demagnetizing field can only be calculated numerically (e.g. with the finite element method), however, an analytical solution for homogeneously magnetized ellipsoids is possible and the total magnetostatic interaction energy is expressed as

$$E_{MS} = \frac{\mu_0}{2} M_s^2 \cdot (N_x \alpha^2 + N_y \beta^2 + N_z \gamma^2) \cdot V \quad (2.22)$$

with the demagnetizing factors N_i and the directional cosines α, β, γ . The sum of the demagnetizing factors equals 1 and they describe the demagnetising field in the respective axis: $H_{D,i} = -N_i M_i$. The limitation to rotational ellipsoids ($N_x = N_y, N_z = 1 - 2N_x$) allows the formulation of a shape anisotropy constant

$$K_{sh} = \frac{\mu_0}{2} M_s^2 \cdot (N_x - N_z) = \frac{\mu_0}{4} M_s^2 \cdot (1 - 3N_z) \quad (2.23)$$

Analogous to the anisotropy field caused by the magnetocrystalline anisotropy, the shape anisotropy contribution H_{sh} to the coercive field is

$$H_{sh} = \frac{2K_{sh}}{J_s} = (N_x - N_z) \cdot M_s \quad (2.24)$$

Theoretical limits for the shape anisotropy factor ($N_x - N_z$) are

- 0 for spheres ($N_x = N_y = N_z = 1/3$)
- +1/2 for indefinitely long cylinders ($N_x = N_y = 1/2, N_z = 0$)
- -1 for indefinitely thin surfaces ($N_x = N_y = 0, N_z = 1$).

Considering both magnetocrystalline and shape anisotropy for the coercive field results in Kronmüller's formula

$$H_c = \alpha \cdot \frac{2K_1}{J_s} - N_{eff} \cdot M_s \quad (2.25)$$

where α is a phenomenological parameter that models the coercivity loss due to incoherent reversal processes in real magnets [33]. Typical values for α range from 0.01 to 0.40 [105].

2.3. Finite Element Micromagnetics

2.3.1. Static and Dynamic Micromagnetism

There are multiple options for computational magnetism. If the magnetisation curve $\mathbf{M}(\mathbf{H})$ is known it is possible to solve Maxwell's equation

$$\begin{aligned} \nabla \cdot \mathbf{B} &= 0 \\ \text{with } \mathbf{B} &= \mu_0(\mathbf{H} + \mathbf{M}) = \mu_0(\mathbf{H} + \mathbf{M}(\mathbf{H})) \end{aligned} \quad (2.26)$$

This approach is suitable for large scale systems, however, all micromagnetic effects are hidden in the material law $\mathbf{M}(\mathbf{H})$. A true micromagnetic approach would be the minimization of the free energy

$$E_{tot} = E_Z + E_{ex} + E_A + E_{MS} \quad (2.27)$$

with the Zeeman energy E_Z , the exchange energy E_{ex} , the magnetocrystalline anisotropy energy E_A and the magnetostatic interaction energy E_{MS} as discussed in chapter 2.2. This approach is known as static micromagnetism. Energy minimisation yields two important relations. Firstly,

$$\frac{\delta E_{tot}}{\delta \mathbf{J}} = \mathbf{H}_{eff} \quad (2.28)$$

which means that every energy term has a corresponding effective field:

$$\mathbf{H}_{eff} = \mathbf{H}_{ext} + \mathbf{H}_{ex} + \mathbf{H}_A + \mathbf{H}_D \quad (2.29)$$

with the (total) effective field \mathbf{H}_{eff} , the external field \mathbf{H}_{ext} , the exchange field \mathbf{H}_{ex} the anisotropy field \mathbf{H}_{A} and the demagnetizing field \mathbf{H}_{D} . Secondly, energy minimization gives a condition for a energy minimum:

$$\mathbf{J} \times \mathbf{H}_{\text{eff}} = 0 \quad (2.30)$$

which means that in an equilibrium state the effective field creates no torque on the magnetic polarization. These findings motivate the formulation of the dynamic Landau-Lifshitz-Gilbert equation

$$\frac{\partial \mathbf{J}}{\partial t} = -|\gamma| \cdot \mathbf{J} \times \mathbf{H}_{\text{eff}} + \frac{\alpha}{J_s} \cdot \mathbf{J} \times \mathbf{J} \times \mathbf{H}_{\text{eff}} \quad (2.31)$$

or equivalently

$$\frac{\partial \mathbf{J}}{\partial t} = -|\gamma| \cdot \mathbf{J} \times \mathbf{H}_{\text{eff}} + \frac{\alpha}{J_s} \cdot \mathbf{J} \times \frac{\partial \mathbf{J}}{\partial t} \quad (2.32)$$

with the gyromagnetic ratio γ and the phenomenological Gilbert damping parameter α . The first term describes the precession of the magnetic polarization around the effective field the second term damps this precession and forces the polarization to align to the effective field (see fig. 14).

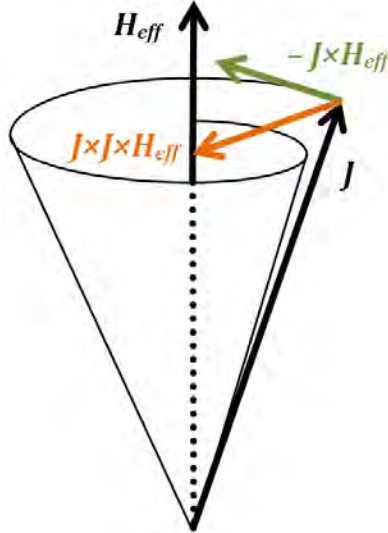


Fig. 14: Precession and damping term in the Landau-Lifshitz-Gilbert equation.

2.3.2. Finite Element Method

2.3.2.1. Weak Formulation

The finite element method for discretizing and solving differential equations is based on the Galerkin Method [64, 65]. Firstly, the strong formulation of a differential equation, e.g. the Poisson problem

$$\begin{aligned} -\Delta u &= f & \text{in } \Omega \\ u &= 0 & \text{on } \partial\Omega \end{aligned} \quad (2.33)$$

with $u = u(x)$ and $f = f(x)$ is converted to the weak formulation. The strong formulation is multiplied by a test function v and integrated over the open region Ω .

$$-\int_{\Omega} \Delta u v \cdot dV = \int_{\Omega} f v \cdot dV \quad (2.34)$$

Using Green's First Identity [63, 64] gives the weak formulation of the Poisson problem

$$\int_{\Omega} \nabla u \nabla v \cdot dV - \int_{\partial\Omega} \nabla u v \cdot \mathbf{n} \cdot dS = \int_{\Omega} f v \cdot dV \quad \forall v = v(x) \quad (2.35)$$

The integral over the boundary $\partial\Omega$ is eliminated or evaluated by boundary conditions. The advantage of the weak formulation is that the solutions $u(x)$ must only be differentiable once as opposed to twice in the strong formulation. It is clear that the solution to the strong formulation is also a solution to the weak formulation, the reverse is not always true. However, the solutions of the weak formulation can approximate the solution of the strong formulation with arbitrary precision [113].

2.3.2.2. Basis Functions

The weak formulation of the Poisson problem requires that equation 2.35 must be true for all test functions $v(x)$. While it is impossible to check all test functions in the infinite-dimensional function space, it is possible to restrict the problem to a finite-dimensional subspace. Examples of subspaces are the space of polynomials (constructed by a Taylor series), the space of periodic functions (constructed by

a Fourier series) or the space of piecewise linear functions (constructed by linear interpolation between supporting points). In a n -dimensional subspace it is sufficient to test with all n basis functions $\varphi_i(x)$ because any function $f_n(x)$ in this subspace is a linear combination of basis functions and coefficients or weights α_i .

$$f(x) \approx f_n(x) = \sum_{i=0}^{n-1} \alpha_i \varphi_i(x) \quad (2.36)$$

The function $f_n(x)$ is an approximation of the exact function $f(x)$ in the infinite-dimensional function space. For example, $f_n(x)$ could be a polynomial of degree $(n - 1)$ with the basis functions

$$\varphi_i(x) = x^i \quad (2.37)$$

Fig. 15 shows a polynomial approximation with two exemplary weighted basis functions $\alpha_i \varphi_i(x)$.

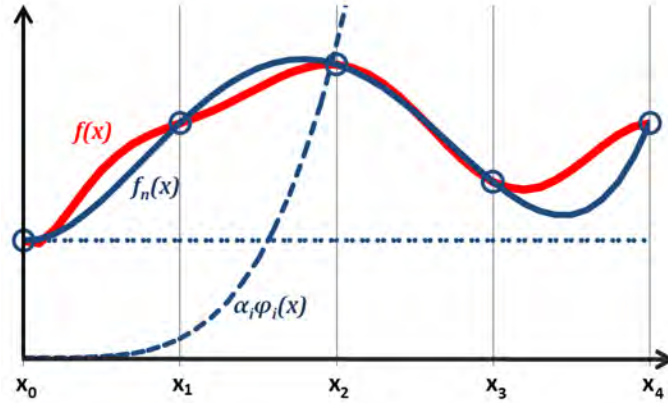


Fig. 15: Exact function $f(x)$ (red) and a polynomial approximation $f_n(x)$ (blue) with two weighted basis functions (dashed).

The finite element method uses the subspace of piecewise linear functions with hat functions as basis. Hat functions φ_i between equidistant supporting points $x_i = i \cdot h$ are defined as

$$\varphi_i(x) = \begin{cases} +\frac{1}{h}x + 1 - i & \text{for } (i-1)h \leq x \leq ih \\ -\frac{1}{h}x + 1 + i & \text{for } ih \leq x \leq (i+1)h \\ 0 & \text{otherwise} \end{cases} \quad (2.38)$$

The hat functions as basis have a couple of nice properties. First of all, they fulfill

$$\varphi_i(x_j) = \delta_{ij} \quad (2.39)$$

for all supporting points x_j . Secondly, there is no need to solve a system of equations to extract the coefficients α_i , because they are directly defined by the supporting points (see fig. 16).

$$\alpha_i = f(x_i) \quad (2.40)$$

Lastly, and most importantly, the hat functions are sufficiently smooth to be used in the weak formulation of the Poisson problem and are differentiable once. The second derivative of hat functions (or piecewise linear functions in general) is constant zero, which means that they are not solutions to the strong formulation of the Poisson problem. Without the weak formulation it would be impossible to approximate the correct solution with piecewise linear functions [113].

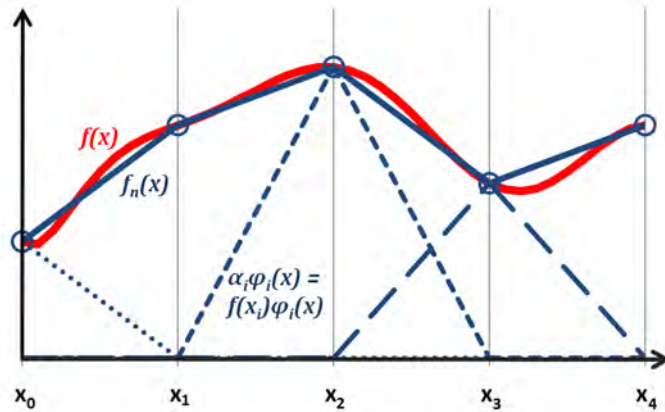


Fig. 16: Exact function $f(x)$ (red) and a piecewise linear approximation $f_n(x)$ (blue) with three weighted basis functions (dashed). The weights are simply the function value $f(x_i)$ at the supporting points.

2.3.2.3. Constructing a System of Linear Equations

With the choice of basis functions it is possible to find a solution to the weak formulation of the Poisson problem. The n basis functions $\varphi_i = \varphi_i(x)$ act as test functions that must fulfill the weak formulation

$$\int_{\Omega} \nabla u \nabla \varphi_i \cdot dV = \int_{\Omega} f \varphi_i \cdot dV \quad i = 1 \dots n \quad (2.41)$$

Furthermore, it is possible to construct the functions u and f with the basis functions. For the unknown function u we need to introduce n unknown weights α_j , whereas the weights for f are simply the function value at the supporting points x_j when using hat functions as basis.

$$\int_{\Omega} \sum_{j=0}^{n-1} \alpha_j \nabla \varphi_j \nabla \varphi_i \cdot dV = \int_{\Omega} \sum_{j=0}^{n-1} f(x_j) \varphi_j \varphi_i \cdot dV \quad i = 1 \dots n \quad (2.42)$$

Exploiting the linearity of the integrals, equations 2.42 are transformed to system of linear equations $\mathbf{A} \cdot \boldsymbol{\alpha} = \mathbf{b}$

$$\underbrace{\begin{pmatrix} \int \nabla \varphi_0 \nabla \varphi_0 & \cdots & \int \nabla \varphi_{n-1} \nabla \varphi_0 \\ \vdots & \ddots & \vdots \\ \int \nabla \varphi_0 \nabla \varphi_{n-1} & \cdots & \int \nabla \varphi_{n-1} \nabla \varphi_{n-1} \end{pmatrix}}_{\mathbf{A}} \cdot \underbrace{\begin{pmatrix} \alpha_0 \\ \vdots \\ \alpha_{n-1} \end{pmatrix}}_{\boldsymbol{\alpha}} = \underbrace{\begin{pmatrix} \sum_j f(x_j) \int \varphi_j \varphi_0 \\ \vdots \\ \sum_j f(x_j) \int \varphi_j \varphi_{n-1} \end{pmatrix}}_{\mathbf{b}} \quad (2.43)$$

Solving this equation yields the coefficients α_j . The weak formulation yields an approximate solution $u_n(x)$ to the exact solution $u(x)$ of the strong formulation:

$$u(x) \approx u_n(x) = \sum_{j=0}^{n-1} \alpha_j \varphi_j(x) \quad (2.44)$$

Because the hat functions are non-zero on a very small range ($\varphi_i(x_j) = \delta_{ij}$) the integrals $\int \varphi_i \varphi_j$ and $\int \nabla \varphi_i \nabla \varphi_j$ are zero except for neighbouring hat functions. Instead of calculating all integrals which are mostly zero anyway, it is more practical to calculate the integrals based on the *finite elements* between the supporting points x_i and fill the corresponding places in the matrix \mathbf{A} . The finite elements are lines defined by two supporting points x_i in a one-dimensional problem, triangles defined by three supporting points in a two-dimensional problem, or tetrahedrons defined by four supporting points in a three-dimensional problem.

The matrix \mathbf{A} is *sparse* (has very few non-zero elements) which is advantageous for numerical solving in both computational time and memory requirements. \mathbf{A} is sparse because of the choice of hat functions as basis which means that this property is independent of the actual problem. A bad choice of basis functions (for example the polynomials in eq 2.37) would result in a fully filled (or *dense*) matrix [113].

Depending on the problem the matrix \mathbf{A} may also be symmetric, which further cuts computational time and memory requirement in half. This is the case for the Poisson problem but not for the Landau-Lifshitz-Gilbert equation solved in computational micromagnetics.

3. DFT Calculations of Hard Magnetic Phases

3.1. MnAl

The $L1_0$ or τ phase is a highly-ordered phase of the Al-Mn system with promising magnetic properties. Although it has been known since the 1960's [16, 17, 39] it has gotten attention again in recent years [88, 117]. In bulk, the phase is only meta-stable [51], but it is possible to stabilize the phase in thin films or by adding small dopants such as carbon to the bulk material [107].

The intrinsic magnetic properties of $L1_0$ MnAl have been calculated with Wien2k [60] using 10000k-points and PBE-GGA [47] as exchange correlation potential. The aim of these calculations is to replicate theoretical and experimental results to verify the correct usage of Wien2k.

3.1.1. The $L1_0$ structure

The $L1_0$ structure (prototype AuCu) is a highly ordered tetragonal structure consisting of alternating monoatomic layers of Mn and Al. The same structure can be described by a face centered and body centered unit cell, which are equivalent with the transformation $a_{fct} = \sqrt{2} \cdot a_{bct}$ (see fig. 17)

Both unit cell choices have the same space group (123, $P4/mmm$), however, Pearson assigned different symbols and structure prototypes to the configurations (body centered: tP2, HgMn, face centered: tP4, AuCu [39]).

Atom	Wyckoff	x	y	z
Al1	1a	0	0	0
Al2	1c	1/2	1/2	0
Mn	2e	0	1/2	1/2

Atom	Wyckoff	x	y	z
Al	1a	0	0	0
Mn	1d	1/2	1/2	1/2

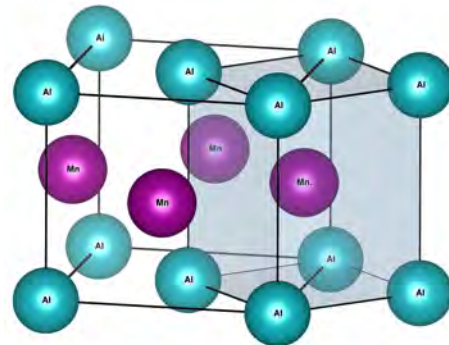


Fig. 17: Atomic positions of body centered and face centered unit cell choices of $L1_0$ MnAl

3.1.2. Results and Discussion

The first set of lattice parameters are taken from a thin film experiment [107]. The authors chose the body centered configuration with $a = 2.77 \text{ \AA}$ and $c = 3.54 \text{ \AA}$ ($c/a = 1.278$). Wien2k calculations with 10000 k-Points in the first Brillouin zone PBE-GGA [47] as exchange correlation functional. After convergence was reached with a criterion of $\Delta E = 10^{-9} Ry$ in a scalar-relativistic calculation, the spin-orbit coupling has been introduced with the *initso_one* method (for details see section 2.2.3.3, p. 21)

Table 3 summarizes the spin moments per atom in the unit cell. The macroscopic saturation polarization is calculated by

$$J_s = \mu_0 \frac{\mu_{u.c.}}{V_{u.c.}} \quad (3.1)$$

with the magnetic moment per unit cell $\mu_{u.c.}$ and the unit cell volume $V_{u.c.}$. The small fluctuations of magnetic moment for different spin-orbit directions are caused numerical error. The main contribution to the magnetic moment comes from the Mn atoms, whereas the Al atoms only exhibit a small magnetic moment aligned antiparallel to the Mn moments. Density matrix calculations make it possible to decompose the total moments into its orbital contributions and show that the Mn-d electrons are responsible for the magnetic moment in MnAl (see table 4). By comparing the total energies of fully converged simulations with different spin-orbit directions, the magnetocrystalline anisotropy energy (MAE) is determined to be 2.09 MJ/m^3 (see table 5).

To verify the results and that both configurations are indeed equivalent, the same calculation has been performed on the face centered tetragonal (f.c.t) unit cell choice with $a_{fct} = \sqrt{2} \cdot a_{bct} = 3.92 \text{ \AA}$ and $c_{fct} = c_{bct} = 3.54 \text{ \AA}$. The spin-orbit coupling split the Mn atom at the 2e into two inequivalent positions, but both saturation polarization and magnetocrystalline anisotropy are in good agreement with the body centered unit cell choice (see tables 6 and 7).

The total energies and the absolute energy differences between magnetization directions are by a factor of two higher compared to the body centered unit cell choice, but the MAE per volume stays constant in the face centered structure (see

Spin Moments	sp	so001	so100	so110	so111
Al [$\mu_B/atom$]	-0.0773	-0.0772	-0.0772	-0.0772	-0.0772
Mn [$\mu_B/atom$]	2.4520	2.4519	2.4524	2.4522	2.4521
Interstitial [$\mu_B/u.c.$]	-0.0014	-0.0011	-0.0012	-0.0012	-0.0011
Total [$\mu_B/u.c.$]	2.3733	2.3737	2.3740	2.3738	2.3738
Js [T]	1.022	1.022	1.022	1.022	1.022

Table 3: Spin moments per atom and resulting macroscopic saturation polarization in MnAl (b.c.t.) **sp** is the scalar-relativistic spin-polarized calculation, **soXXX** includes spin orbit coupling in the direction **XXX**.

Spin Moments	s	p	d	f	Sum of Site
Al	-0.0302	-0.0612	0.0098	0.0032	-0.0784
Mn	0.0222	0.0233	2.4041	0.0013	2.4510
SUM of SPI	-0.0081	-0.0378	2.4139	0.0046	

Table 4: Per-orbital contributions to the spin magnetic moment in MnAl (b.c.t.)

	sp	so001	so100	so110	so111
TOT +2802 Ry	-0.99249	-0.99335	-0.99332	-0.99333	-0.99334
MAE [$Ry/u.c.$]			2.612E-05	1.71E-05	7.301E-06
MAE [kJ/m^3]			2.093	1.369	0.585

Table 5: Total Energy (TOT) and magnetocrystalline anisotropy energy (MAE) of MnAl (b.c.t.)

table 6). This is caused by the higher number of atoms in the face centered structure and the higher unit cell volume.

The calculated magnetic moments ($\mu_{Mn} = 2.45\mu_B, \mu_{MnAl} = 2.37\mu_B/f.u.$ are in good agreement with both theoretical and experimental literature values between 2.29 and 2.41 $\mu_B/f.u.$ [42, 88, 107, 117]. The calculated MAE of 2.1 MJ/m^3 is higher than experimental results (1.4 MJ/m^3 [107]) but in good agreement with other calculations (SPR-KKR: 1.95 MJ/m^3 [117], force theorem: 1.98 MJ/m^3 [126], perturbation theory: 2.15 MJ/m^3 [126])

Spin Moments	sp	so001	so100	so110	so111
Al 1 [$\mu_B/atom$]	-0.0778	-0.0777	-0.0777	-0.0777	-0.0777
Al 2 [$\mu_B/atom$]	-0.0778	-0.0777	-0.0777	-0.0777	-0.0777
Mn 1 I [$\mu_B/atom$]	2.4555	2.4534	2.4535	2.4542	2.4541
Mn 1 II [$\mu_B/atom$]		2.4534	2.4535	2.4542	2.4541
Interstitial $\mu_B/u.c.$	-0.0035	-0.0034	-0.0034	-0.0033	-0.0033
Total [$\mu_B/u.c.$]	4.7519	4.7481	4.7481	4.7497	4.7495
Js [T]	1.021	1.021	1.021	1.021	1.021

Table 6: Spin moments per atom and resulting macroscopic saturation polarization in MnAl (f.c.t.)

	sp	so001	so100	so110	so111
TOT +5605Ry	-0.98498522	-0.98669174	-0.986638	-0.986658	-0.986678
MAE [$Ry/u.c.$]			5.37E-05	3.37E-05	1.37E-05
MAE [kJ/m^3]			2.155	1.353	0.551

Table 7: Total Energy (TOT) and magnetocrystalline anisotropy energy (MAE) of MnAl (f.c.t.) **sp** is the scalar-relativistic spin-polarized calculation, **soXXX** includes spin orbit coupling in the direction **XXX**.

3.2. LTP MnBi

The low temperature phase of MnBi is a stable phase of the Bi-Mn system has a couple of interesting properties, that are not yet fully understood. [24, 26, 34, 130]

- At $T = 0K$ it has an in-plane magnetocrystalline anisotropy
- At $T = 80K$ a spin reorientation takes place and the anisotropy changes to uniaxial
- At $T > 80K$ the magnetocrystalline anisotropy increases with increasing temperature
- At $T = 593K$ a first order transition that decreases the c/a ratio takes place
- At $T = 720K$ the LTP decomposes into a high-temperature phase and Bi

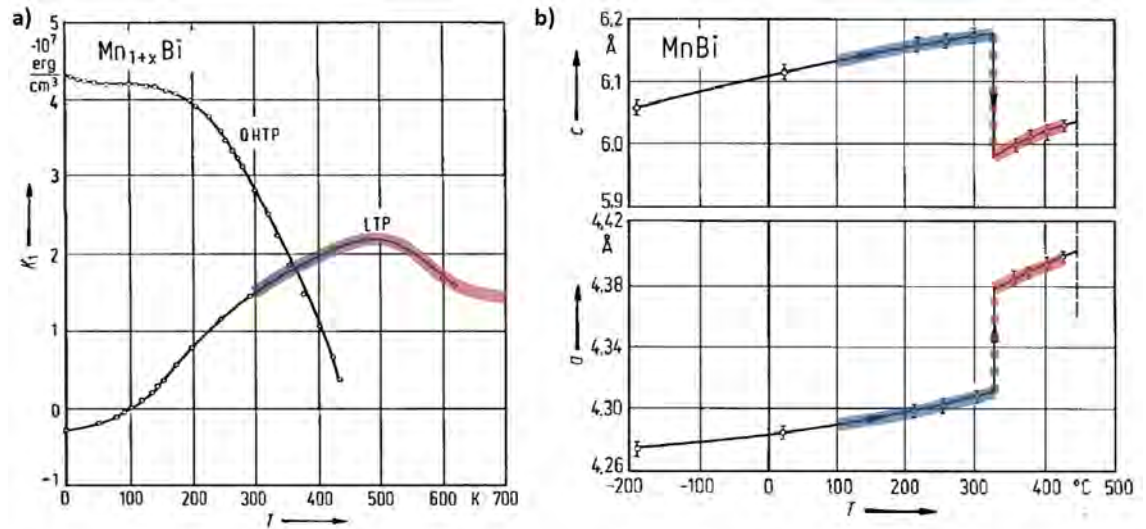


Fig. 18: Magnetocrystalline anisotropy constant (a) and lattice parameters (b) as function of temperature, based on [34] and [144]. The color gradient shows the investigated region (see fig. 21).

The moderate saturation polarization combined with the increasing magnetocrystalline anisotropy make it an interesting material for high temperature applications. These properties motivate a systematic study of the magnetic properties of MnBi as function of the lattice parameters [144].

LTP MnBi has a hexagonal closely packed structure with altering mono-atomic Mn and Bi layers in **ABAC** stacking. The **A** layers have the Wyckoff position 2a, the **B** and **C** stacks have Wyckoff positions 2c (see fig. 19). It is noteworthy that the

2a and 2c sites have different atomic environments (see fig. 20). This means, that exchanging the positions of Mn and Bi in the structure lead to different systems. To distinguish the configurations, the system with Mn at the origin (2a site) will be called *MnBi* and the system with Bi at the origin will be called *BiMn* throughout the thesis. Both configurations are mentioned in the literature (*MnBi*: [26, 39, 109, 130]; *BiMn*: [20, 39, 105]).

Name	LTP MnBi
Space Group	194 P63/mmc
a, b	4.28 Å
c	6.11 Å
α, β	90°
γ	120°

Atom	Wyckoff	x	y	z
Mn	2a	0	0	0
Bi	2c	1/3	2/3	1/4

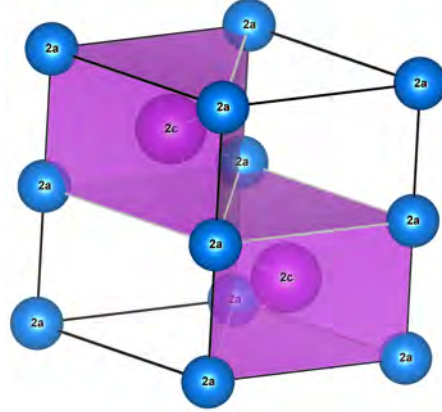


Fig. 19: Lattice parameters and unit cell of LTP MnBi [26]

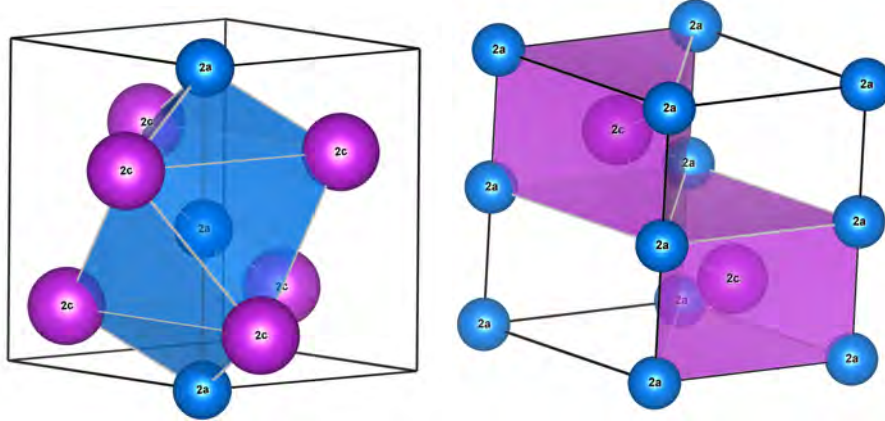


Fig. 20: Atomic Environments of the 2a and 2c sites in space group 194

3.2.1. MnBi at 0K

3.2.1.1. Lattice Parameters

Wien2k calculations have been performed with 10000 k-points and PBE-GGA [47] as exchange correlation functional. After convergence of a scalar-relativistic calculation (criterion: $\Delta E = 10^{-9} Ry$, relativistic effects (spin-orbit coupling with *initso_one* [p. 21] and orbital contraction of Bi-s states by local orbitals) have been included.

The equilibrium lattice parameters have been calculated by minimizing the total energy as function of volume (with constant c/a ratio) and then function of c/a ratio (with constant volume). The effects of spin-orbit coupling and orbital contraction have been included in the calculation of lattice parameters. The calculated lattice parameters $a = 4.3408 \text{ \AA}$ and $c = 5.7142 \text{ \AA}$ deviate from experimental results ([24, 20, 34, 39], see also figs. 18 and 19) but are in good agreement with other DFT calculations ([57, 130]).

3.2.1.2. Magnetocrystalline anisotropy

The magnetocrystalline anisotropy energy (MAE) was calculated as difference of total energy between two fully converged calculations including relativistic effects. For the *MnBi* system the calculated MAE of $-0.11 MJ/m^3$ [144] is higher then the experimentally measured value of $-0.2 MJ/m^3$ [34, 109] but better than previous DFT calculations ($-2.1 MJ/m^3$ [53, 130]). However, the value of $-2.1 MJ/m^3$ has been reproduced by using the *initso_111* initialization method.

Calculations on the *BiMn* configuration showed a MAE of $+1.55 MJ/m^3$ which corresponds to a uniaxial anisotropy that is not found experimentally at low temperatures. Only the *MnBi* system describes the low temperature behavior of LTP MnBi correctly.

3.2.2. Magnetic Moments

The *MnBi* system has a total spin magnetic moment of $3.72 \mu_B / f.u.$; the main contribution are the Mn-d states with $3.68 \mu_B$. The spin-moments of Bi are aligned anti-parallel to the Mn moments lowering the total magnetic moment (see table 8).

These values are in agreement with other DFT calculations, but are lower than the experimental values in the range of $\mu_{Mn} = 3.82 - 4.25\mu_B$ [109, 130].

Considering the orbital contributions as well ($\mu_{Mn,orb} = 0.07\mu_B$), it is possible to reach the lower bound of experimental results without the need of a phenomenological Hubbard U potential (LDA+U [67], GGA+U [76])

3.2.3. Temperature Dependence of MAE

For the temperature dependence of the intrinsic properties, only lattice expansion has been considered. Other effects (phonons, temperature smearing of bands) have been neglected. The lattice parameters have been varied in the range of lattice parameters found experimentally between $300K$ and $700K$ (see colored region in fig 18). The unit cell volume was in the range between 97 \AA^3 and 101 \AA^3 and the c/a ratio between 1.35 and 1.45.

The MAE of the *MnBi* system stayed negative throughout the examined lattice parameter range. This means that the spin reorientation cannot be explained by lattice expansion alone. However, the *BiMn* system shows MAEs between $1.35 MJ/m^3$ and $2.25 MJ/m^3$ which is the experimentally found K_1 range (compare fig. 18b and 21). The MAE increases with unit cell volume at all c/a ratios, which explains the general trend of increasing K_1 values with temperature. The optimal c/a ratio for maximizing the magnetocrystalline anisotropy is 1.375, which could be realized by dopants [106].

3.2.4. Conclusion

With the help of density functional theory calculations it was possible to verify that exchanging Mn and Bi positions in the unit cell lead indeed to different systems. Both configurations have been reported in literature. The *MnBi* system (Mn at 2a) describes the magnetocrystalline anisotropy and magnetic moments correctly at $0K$. The *BiMn* correctly describe the magnetic moments and the temperature dependence of magnetocrystalline anisotropy above room temperature. The results suggest that the unusual properties of MnBi could be a consequence of a subtle phase transition between *MnBi* and *BiMn* configuration.

	s	p	d	f	sum
Mn	0.05770	0.02721	3.68389	-0.00008	3.76872
Bi	0.02100	-0.15420	0.01055	0.00432	-0.11833
interstitial					0.07154
sum	0.07870	-0.12699	3.69444	0.00424	3.72193

Table 8: Spin Moments of *MnBi* at $T = 0K$ in μ_B

	p	d	f	sum
Bi	-0.00011	0.07802	0.00020	0.07811
Mn	-0.00413	-0.00015	-0.00010	-0.00438
sum	-0.00424	0.07787	0.00010	0.07373

Table 9: Orbital Moments of *MnBi* at $T = 0K$ in μ_B

	s	p	d	f	sum
Bi	0.02437	-0.07656	0.01122	0.00558	-0.03539
Mn	0.08713	0.04057	3.81380	0.00024	3.94174
interstitial					0.28596
sum	0.11150	-0.03599	3.82502	0.00582	4.19231

Table 10: Spin Moments of *BiMn* at $T = 0K$ in μ_B

	p	d	f	sum
Bi	-0.00754	-0.00046	-0.00052	-0.00852
Mn	-0.00171	0.10225	0.00026	0.10080
sum	-0.00925	0.10179	-0.00026	0.09228

Table 11: Orbital Moments of *BiMn* at $T = 0K$ in μ_B

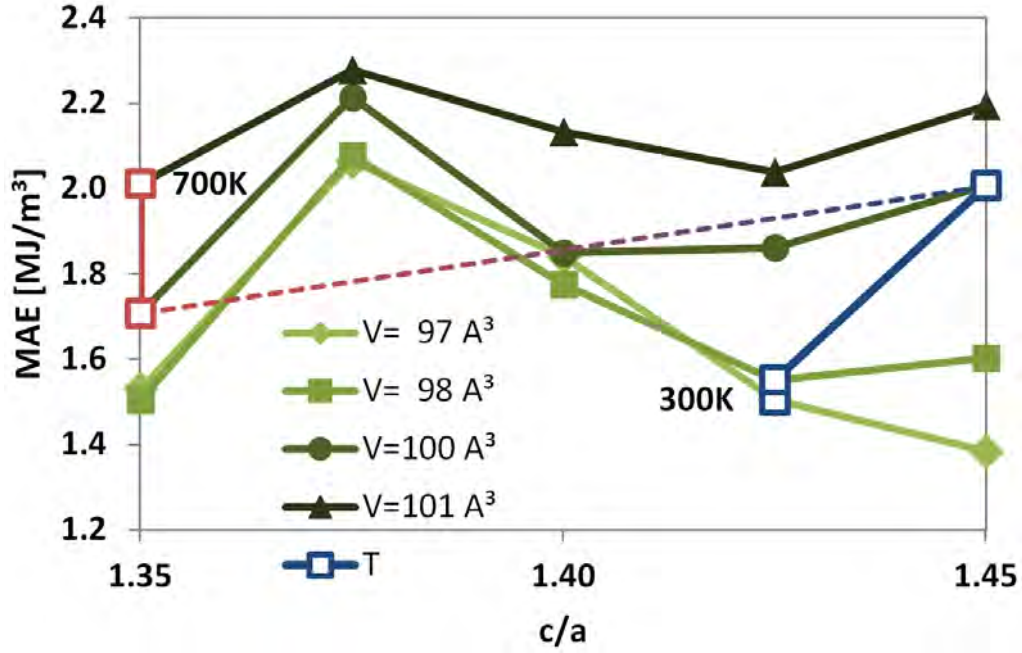


Fig. 21: *BiMn*. Dependence of MAE as function of unit cell volume and c/a ratio. The blue to red line connects the best fits to experimentally found lattice parameters as function of temperature. The dotted region marks the first order phase transition at 593K reducing the c/a ratio

3.3. Fe-Co-B

The $(\text{Fe}_{1-x}\text{Co}_x)_2\text{B}$ ternary alloys are another material that has been known for a long time, but got recently new attention due to the rare earth crisis. Iga [22] measured the $(\text{Fe}_{1-x}\text{Co}_x)_2\text{B}$ system over a wide composition and temperature range. He showed that the ternary $(\text{Fe}_{1-x}\text{Co}_x)_2\text{B}$ alloys with a composition $0.1 \leq x \leq 0.5$ exhibit an uniaxial magnetocrystalline anisotropy although the binaries Fe_2B and Co_2B have in-plane anisotropy. The maximum anisotropy at $x = 0.3$ was later verified in single crystal measurements [127].

3.3.1. Binary alloys

The first step to understand the $(\text{Fe}_{1-x}\text{Co}_x)_2\text{B}$ system is the study of the two parent binary alloys Fe_2B and Co_2B . Experimental lattice parameters were taken from [75] for Fe_2B and [28] for Co_2B (see fig. 23). The equilibrium lattice parameters have been calculated using Wien2k with PBE-GGA [47], 10000 k-points and a

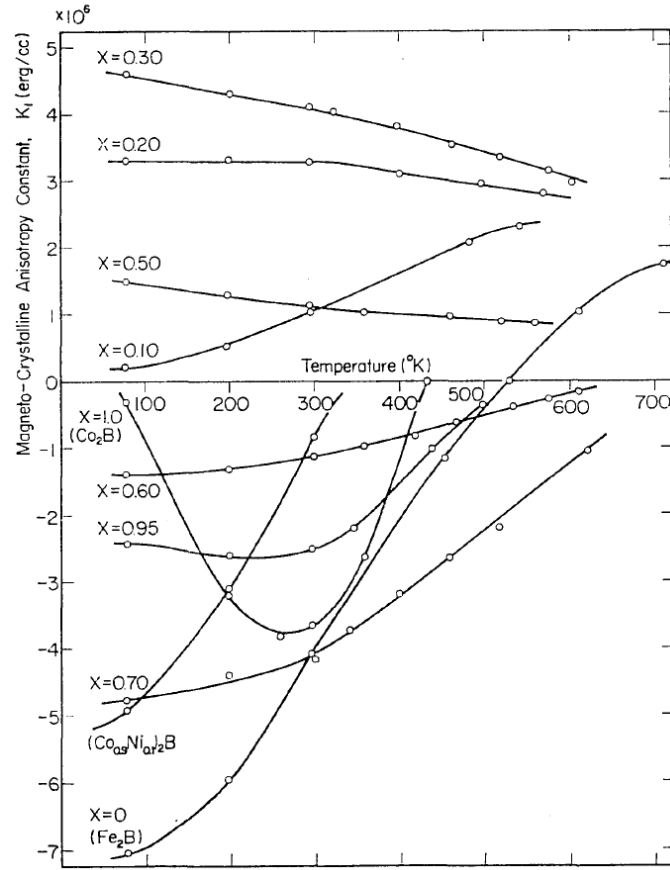


Fig. 22: The temperature dependence of K_1 of $(\text{Fe}_{1-x}\text{Co}_x)_2\text{B}$ alloys reported by [22].
y-axis scale is in 10^6 erg/cm^3 or 0.1 MJ/m^3

Name	Fe_2B	Co_2B
Space Group	140 I4/mcm	
a, b	5.1204 Å	5.014 Å
c	4.2588 Å	4.215 Å
α, β, γ	90°	

Atom	Wyckoff	x	y	z
Fe/Co	8h	1/6	2/3	0
B	4a	0	0	1/4

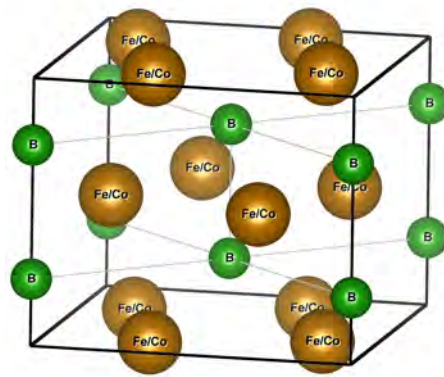


Fig. 23: Lattice parameters and atomic positions for Fe_2B [75] and Co_2B [28]

convergence criterion of $10^{-5} Ry$. The inclusion of spin-orbit effects had no significant influence on the obtained lattice parameters.

The calculated equilibrium lattice parameters for Fe_2B are smaller than the experimental values ($a = 5.0693 \text{ \AA}$, $c = 4.2226 \text{ \AA}$ compared to $a = 5.1204 \text{ \AA}$ and $c = 4.2588 \text{ \AA}$) but the c/a ratio of 0.832 changed only by 0.62%. For Co_2B a lower a lattice parameter but a higher c lattice parameter was found ($a = 4.9617 \text{ \AA}$, $c = 4.2402 \text{ \AA}$ compared to $a = 5.0140 \text{ \AA}$ and $c = 4.2150 \text{ \AA}$) leading to an increase of the c/a ratio by 1.66%. These values are in good agreement with other DFT results [135]

The calculations of the magnetic moments and the magnetocrystalline anisotropy have been performed with a stricter convergence criterion ($\Delta E = 10^{-9} Ry$) and are summarized in table 3.3.1. The spin moments deviate only slightly from the experimental results. The calculations predict the anisotropy type correctly, but underestimate the MAE for Fe_2B and overestimate the MAE for Co_2B . Fixed spin moment calculations revealed that the MAE is very sensitive to changes of the spin moments and forcing the experimentally spin moments in the calculation yield the correct values for MAE [136]

	Fe₂B	Co₂B
Spin Moments		
Fe/Co I [$\mu_B/atom$]	1.961	1.088
Fe/Co II [$\mu_B/atom$]	1.961	1.088
B [$\mu_B/atom$]	-0.112	-0.047
Interstitial [$\mu_B/u.c.$]	-0.197	-0.140
Total [$\mu_B/u.c.$]	7.424	4.117
J_s [T]	1.596	0.924
MAE [100] - [001]		
MAE [$\mu eV/f.u.$]	-58	-132
MAE [MJ/m^3]	-0.344	-0.811

Table 12: Magnetic moment and MAE of Fe_2B and Co_2B

3.3.2. Virtual Crystal Approximation

The Virtual Crystal Approximation (VCA, [5, 6]) allows us to calculate the properties of $(Fe_{1-x}Co_x)_2B$ ternary alloys for an arbitrary composition x in a single unit cell. The lattice parameters and atomic positions are linearly interpolated

between the binaries Fe_2B and Co_2B . Each Fe/Co position is occupied by a virtual atom with a non-integer atomic number $26 + x$. When using Wien2k, the x electrons per Fe/Co atom have to be inserted manually in the `*.in2` file as valence electrons and the occupations in the `*.inc` have to be adopted manually [60].

VCA gives surprisingly good results given how simple the method is. However, it is only possible to use VCA with *neighboring* atoms such as Fe (atomic number 26) and Co (27). Fe-Ni alloys could not be calculated with VCA. As alternatives the coherent potential approximation [23], super cells and special quasirandom structures [37] should be mentioned.

3.3.3. Results

The magnetic properties of the $(\text{Fe}_{1-x}\text{Co}_x)_2\text{B}$ ternary alloys have been calculated with two sets of lattice parameters. The first set of calculations uses the literature lattice parameters of the binary alloys directly and interpolates linearly between them. The second set of calculations finds equilibrium lattice parameters for each ternary composition separately before the magnetic properties are calculated. Table 13 summarizes the lattice parameters. The lattice optimization has also been performed with Perdew’s and Wang’s LDA formulation [40] for comparison, but these values have not been used in follow-up calculations.

The calculated equilibrium unit cells are smaller than the literature values, which is expected when comparing finite temperature measurements with 0K calculations. The Co-rich side shows an increase of c/a ratio that was also predicted for pure Co_2B and is consistent with other DFT calculations [135, 136]. The LDA lattice parameters for Fe_2B are in slightly better agreement than the PBE-GGA values, but LDA underestimates the lattice parameters for all other compositions and overestimates the c/a ratio for the Co-rich side (see fig. 24).

The magnetocrystalline anisotropy energy (MAE) has been calculated as the difference between total energies of fully converged calculations including spin-orbit coupling effects in $[100]$ and $[001]$ direction (*initso_111* method).

The calculations predict the maximum MAE around $x = 0.3$ correctly and the minimum MAE around $x = 0.8$ but fail to exactly quantify the MAE especially on the Co-rich side. SPR-KKR calculations are in better agreement on the Fe-rich side, but completely fail on the Co-rich side [136]. Using the finite-temperature lattice

parameters from literature leads to a better agreement with finite-temperature measurements (see fig. 25).

In conclusion, the virtual crystal approximation is a good tool to archive fast qualitative results, but in order to get good quantitative agreement it is necessary to use more sophisticated and computational intensive methods, as for example super cells and special quasirandom structures [49, 136]

	a, b [Å]			c [Å]		
	lit.	LDA	PBE	lit.	LDA	PBE
Fe2B = 0.0	[75] 5.1204	5.0628	5.0718	[75] 4.2588	4.2384	4.2226
0.2	<i>5.0991</i>	5.0343	5.0533	<i>4.2500</i>	4.1972	4.2159
0.4	<i>5.0778</i>	5.0234	5.0381	<i>4.2413</i>	4.1796	4.2036
0.6	<i>5.0566</i>	5.0166	5.0210	<i>4.2325</i>	4.1651	4.2000
0.8	<i>5.0353</i>	4.9448	4.9867	<i>4.2238</i>	4.2767	4.2414
Co2B = 1.0	[28] 5.0140	4.9523	4.9890	[28] 4.2150	4.2553	4.2402

Table 13: Comparison of literature, LDA, and PBE-GGA lattice parameters for the $(\text{Fe}_{1-x}\text{Co}_x)_2\text{B}$ ternary alloys. The italic lattice parameters are linearly interpolated between the literature values of the binary alloys.

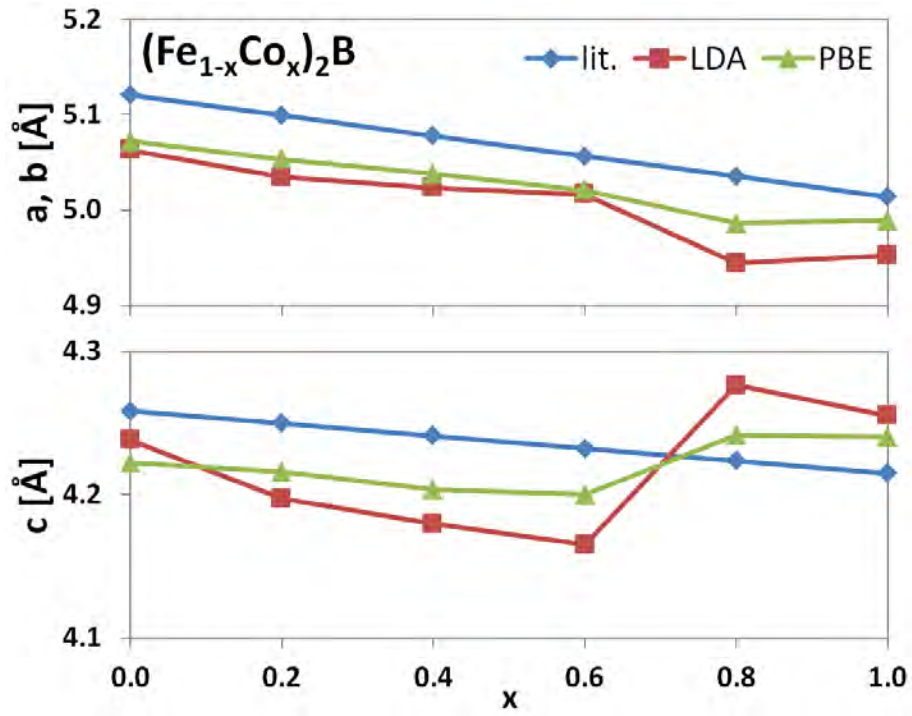


Fig. 24: Literature and calculated lattice parameters of $(\text{Fe}_{1-x}\text{Co}_x)_2\text{B}$

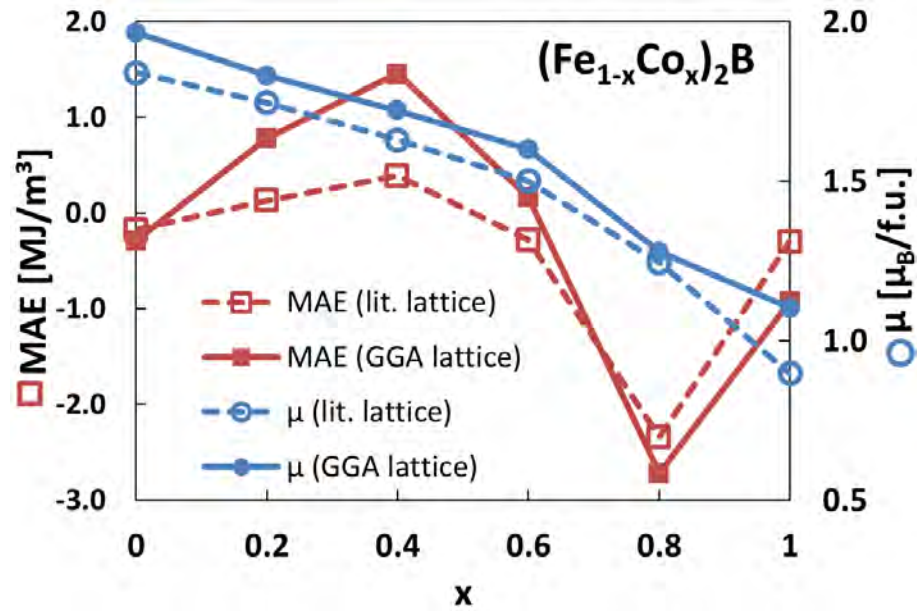


Fig. 25: Calculated MAE (red) and magnetic moments (blue) using the literature lattice parameters (dashed) and equilibrium lattice parameters (solid)

4. Microstructural Optimization of Nd-Fe-B Magnets

4.1. Introduction

Rare earth permanent magnetic materials exhibit outstanding intrinsic properties (high saturation polarization, high magnetocrystalline anisotropy) leading to high coercive fields and energy density products. These properties explain their usage in high energy (motors, generators) and medical applications (magnetic resonance tomography) [140, 141]. The high energy density product is also a key feature for miniaturization (hard disk drives, sensors and microsensoric devices) [59].

The most common rare earth magnetic materials are $\text{Nd}_2\text{Fe}_{14}\text{B}$ and SmCo_5 . Due to its high iron content, $\text{Nd}_2\text{Fe}_{14}\text{B}$ magnets have a high saturation polarization leading to a high energy density product. The disadvantage of $\text{Nd}_2\text{Fe}_{14}\text{B}$ is its relatively low Curie temperature (588 K) making it unsuitable for continuous application at high temperatures. SmCo_5 magnets have a higher Curie temperature (1020 K), higher magnetocrystalline anisotropy (17.2 MJ/m^3 compared to 4.9 MJ/m^3 for $\text{Nd}_2\text{Fe}_{14}\text{B}$) but a lower saturation polarization ($1.07T$ instead of $1.61T$). SmCo_5 is therefore the material to use at high temperatures at the cost of a lower energy density product compared to $\text{Nd}_2\text{Fe}_{14}\text{B}$ [105].

A lot of research effort has been focused on improving the temperature behavior of $\text{Nd}_2\text{Fe}_{14}\text{B}$ by doping the magnet with heavy rare earths such as Dysprosium [32, 110, 137, 138] or Terbium [102, 124]. The doping is performed with a grain boundary diffusion process. The heavy rare earths harden the surface of the grains due to their higher magnetocrystalline anisotropy [115, 133] and suppress nucleation effects and increase coercivity [58, 119]. Due to the supply risk of heavy rare earths, there are also ways to reduce the heavy rare earth content [140] or complete replacements of heavy rare earths [73, 142] under development.

TEM investigations and micromagnetic simulations suggest a strong relationship between the microstructure and the macroscopic properties of $\text{Nd}_2\text{Fe}_{14}\text{B}$ magnets [46, 97, 119, 121, 129, 148, 146]. This motivates the optimization of the microstructure of $\text{Nd}_2\text{Fe}_{14}\text{B}$ magnets with the help of micromagnetic simulations without the need for heavy rare earth dopants.

4.2. Micromagnetic Modelling

4.2.1. Experimental Input and Dimensioning

TEM investigations revealed that typical grain sizes for melt-spun $\text{Nd}_2\text{Fe}_{14}\text{B}$ magnets range from ten to several hundred nanometers [73, 79, 83, 90]. Depending on the production route, the grains can be equiaxed (*grains*) or flat (*platelets*, see fig. 26). Sintered and annealed $\text{Nd}_2\text{Fe}_{14}\text{B}$ magnets have typically grain sizes in the order of several micrometers [94, 102, 132]. The grains are separated by grain boundaries that are Nd-O-rich or Fe-rich with a thicknesses ranging from 5nm up to 30nm [29, 35, 121, 125, 128, 148].

Micromagnetic simulations have been performed on computationally generated, realistic structures with equiaxed *grains* or flat *platelets*. Grain sizes between 10nm and 50nm have been examined. The platelet structures have a mean diameter of 100nm and 20nm thickness.

Micromagnetic models with and without grain boundary region of 5nm have been generated for both *grain* and *platelet* structures. Omitting the grain boundary region describes the limit of perfectly exchange coupled grains.

Three different grain boundary types have been examined: non-magnetic (describing the limit of perfectly exchange decoupling of grains), paramagnetic (Nd-oxides) and ferromagnetic (Fe-rich) [145]. The material parameters are summarized in table 14.

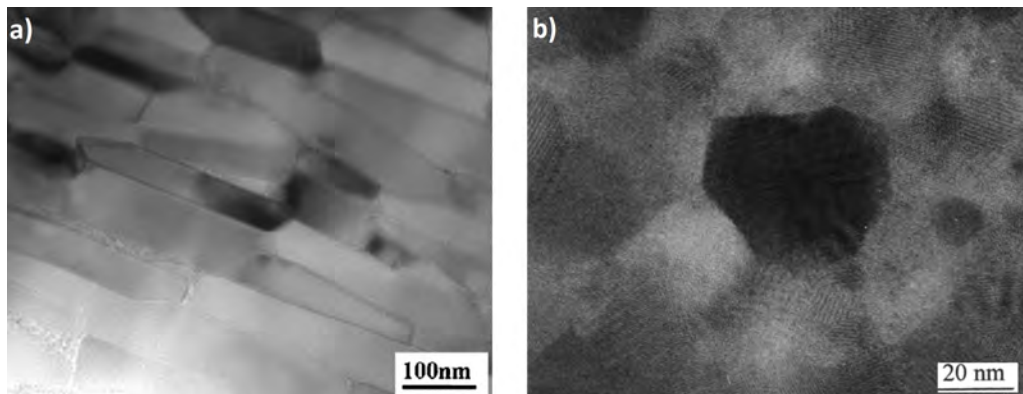


Fig. 26: (a) TEM image of $\text{Nd}_2\text{Fe}_{14}\text{B}$ platelets with 20nm thickness [90]. (b) TEM image of nanocrystalline $\text{Nd}_2\text{Fe}_{14}\text{B}$ [83]

	$\mathbf{K}_1 [MJ/m^3]$	$\mathbf{J}_s [T]$	$\mathbf{A} [pJ/m]$
Nd ₂ Fe ₁₄ B	4.9	1.610	7.700
non-magnetic	0	0.001	0.000
paramagnetic	0	0.750	0.077
ferromagnetic	0	0.750	2.500

Table 14: Material parameters for Nd₂Fe₁₄B grain structures

4.2.2. Model Creation

The micromagnetic grain structure is based on a Voronoi decomposition [1] of the magnetic volume. Each grain is defined by its center, the so-called *seeding-point*. The boundaries of each grain are created by intersecting the bisecting planes of the connection lines of neighbouring seeding points. The Wigner-Seitz cell [7] is a special case of general three dimensional Voronoi constructions.

There are many open source and freeware Voronoi algorithms implemented and published. Both *qhull* [45] and *voro++* [84] have been considered for the creation of the micromagnetic models but *voro++* is more user-friendly and the output is easier to process with Python [71]. The input for *voro++* is a text file containing the seeding points:

```
1  50.0  50.0 50.0
2  150.0  50.0 50.0
3  50.0 150.0 50.0
```

A small helper-script has been implemented to generate the seeding points. The script creates seeding points in a regular grid and applies random displacements to each point. The mean size of the final grains is controlled by the initial distance between seeding points. The script supports three different starting grids for cubic, hexagonal and irregular grains. Fig. 27 shows the *voro++* output for the three grids without random distortion.

The output of *voro++* acts as input for a Salome. Salome is an open source pre- and postprocessing platform with both a graphical and a scripting user interface [80]. A Python script for Salome that creates a finite element mesh for a given Voronoi structure has been implemented.

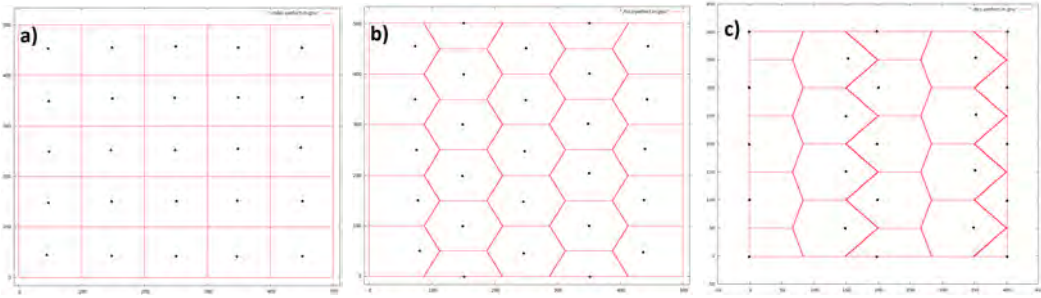


Fig. 27: Voronoi structures with regularly arranged seeding points, top view. a) cubic grid b) hexagonal grid c) irregular grid

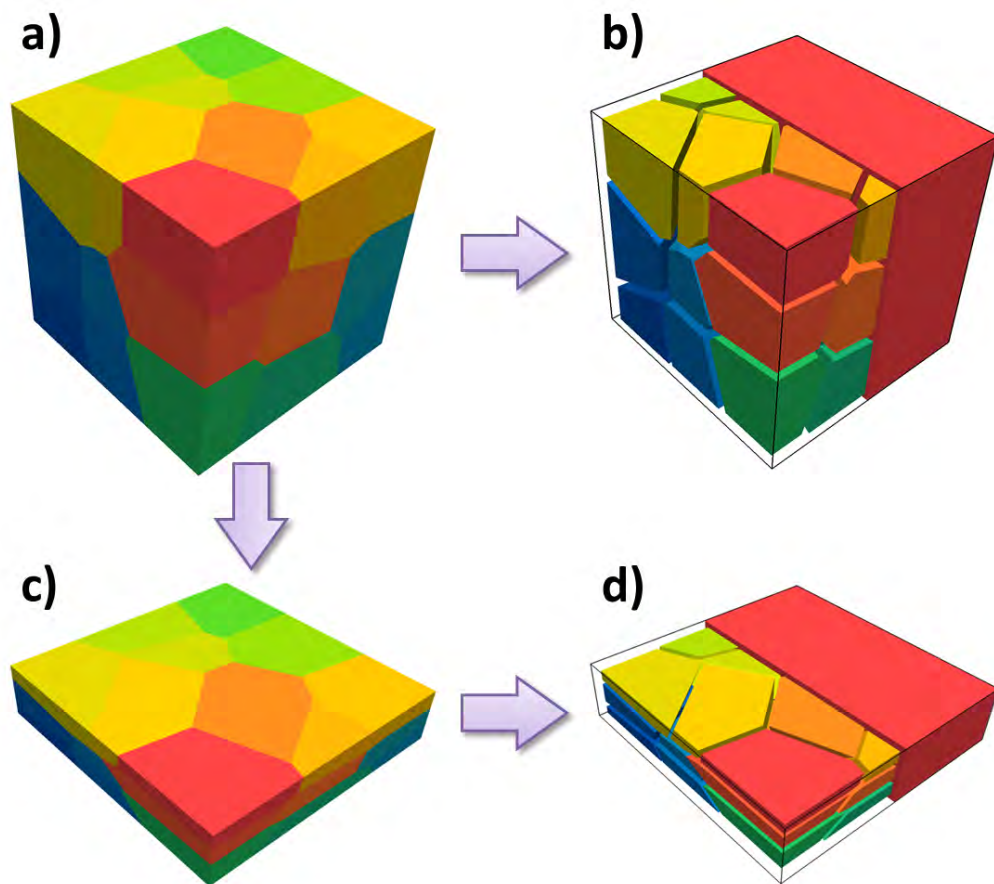


Fig. 28: Creation of grain and platelet structures with and without grain a boundary phase based on the same Voronoi model [145]

The procedure is the following:

1. Read the input from voro++ or qhull results
2. Create a logical grain structure
3. (Optional) Transform the logical grain structure
4. Create Salome vertices, lines, faces and volumes for each grain
5. (Optional) Create a grain boundary
6. Mesh the grain structure

Transformations include the scaling of the whole structure (for creating platelets out of a grain structure) and the shrinking of each grain to create space for the grain boundary.

The grain boundary is constructed by creating a bounding cuboid and Boolean volume operations that cut the grains out of the cuboid. The creation of grain and platelet structures with and without grain boundary is summarized in fig. 28.

All models have been simulated with both oriented and isotropic K_1 distribution. In the oriented model, the polar angle θ follows a Gaussian distribution with a mean misorientation of 7° and a standard deviation of 3° . The isotropic model has a uniform θ distribution between 0° and 90° (see fig. 29). The azimuthal angle φ is uniformly distributed between -180° and $+180^\circ$ in both cases.

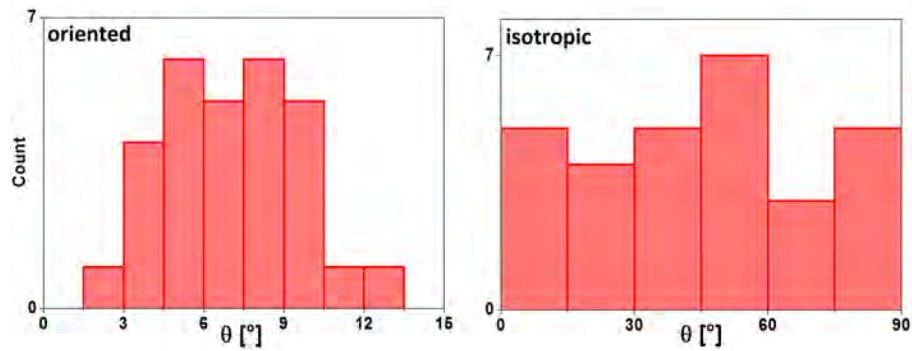


Fig. 29: Oriented and isotropic K_1 distribution

4.3. Results and Discussion

4.3.1. Grains without Grain Boundary

4.3.1.1. Perfect Exchange Coupling

The basic model consists of 30 directly coupled grains with a mean diameter of $50nm$. The 1D mesh size for the finite element model is $2.5nm$ which is below the Bloch domain wall width $\delta_w = 3.9nm$ (see inlay in fig. 30b). The domain wall width is derived from the intrinsic material parameters [81]:

$$\delta_w = \pi \cdot \sqrt{\frac{A}{K_1}} \quad (4.1)$$

It is possible in micromagnetic simulations to switch the calculation of the demagnetizing field off. By comparing simulations with demagnetizing field ($H_{mag} = ON$) and without demagnetizing field ($H_{mag} = OFF$) it is possible to determine the influence of the stray field on the magnetization reversal exactly (see fig. 30a). The demagnetizing field lowers the coercivity of the grain structure by inducing an early nucleation in the hard magnetic grains.

Although the switching seems to occur immediately, the micromagnetic simulations are able to resolve the switching process and reveal complex micromagnetic states during magnetization reversal (see fig. 30).

The coercivity values obtained with demagnetizing field are compared to the predictions of the Stoner-Wolfarth model (see p. 5). The coercive fields of the oriented (*ori*) and isotropic (*iso*) structures are normalized to the anisotropy field of $Nd_2Fe_{14}B$ ($\mu_0 H_A = 2K_1/M_s = 7.65T$) and plotted as horizontal lines in fig. 31. The vertical lines are the mean (dashed) and maximum (solid) misorientation angle θ in the structure.

The results suggest that the weakest grain (and not the mean misorientation) dominates the coercive field in the whole grain structure, if we assume perfect exchange coupling between the grains. The results for the isotropic model are in good agreement with experimental results ($1.0 - 3.6T$ [86, 100, 142]), but the oriented model overestimates the coercivity. Considering the magnetic properties of the grain boundary phase will improve the results for both models.

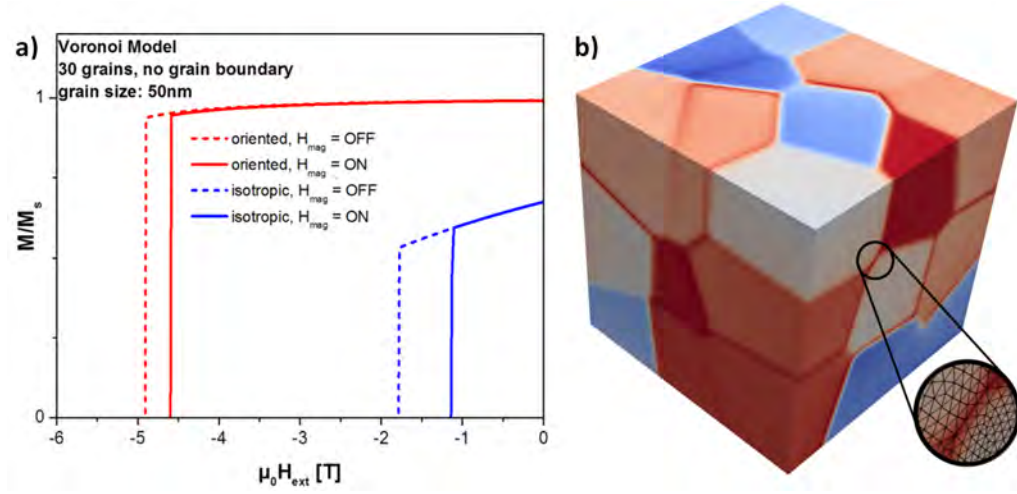


Fig. 30: (a) Demagnetization curves of oriented (red) and isotropic (blue) grain structures with a mean diameter of 50nm. The simulations with demagnetizing field (solid) exhibit lower coercivities than the simulations without (dashed). (b) Micromagnetic state during magnetization reversal of the isotropic model. The inlay shows the finite element discretization [145]

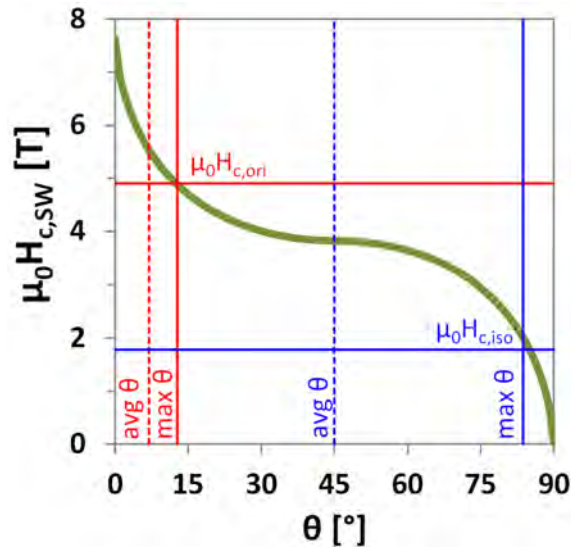


Fig. 31: Coercivity values obtained from micromagnetic simulations (horizontal lines) and mean and maximum misorientation angle θ (vertical lines) compared to the Stoner-Wohlfarth model (green) [10, 145]

4.3.1.2. Influence of Grain Size

By scaling down the structure it is possible to change the grain size while leaving all other parameters such as grain shape, magnetocrystalline anisotropy and easy axis distribution constant. This allows us to determine the influence of grain size on the coercive field separately.

Micromagnetic simulations show that decreasing the mean grain size from 50nm to 20nm increase the coercive field by 14%. Decreasing the size to 10nm increases the coercivity by 18%. Comparing the results with and without demagnetizing field shows that the main contribution to this effect are stray field effects (see fig. 32). At small grain sizes (10nm) the demagnetizing field has even a small, positive contribution to the coercivity.

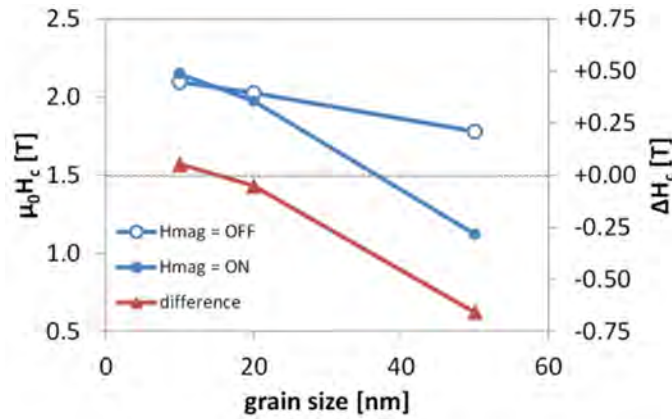


Fig. 32: Dependence of coercivity on grain size with (filled circles) and without (open circles) demagnetizing field. The red line plots the influence of the stray field [145].

4.3.2. Grains with Grain Boundary

The model of perfectly coupled grains can predict the coercivity of isotropic $\text{Nd}_2\text{Fe}_{14}\text{B}$ magnets, but overestimates the coercive field of the oriented model. No real grain structure has perfectly coupled grains. The grains are indirectly coupled over a para- or ferromagnetic grain boundary phase instead.

Based on the Voronoi model with 50nm grains, each grain is shrunk by approximately 2.5nm in each direction leaving space for a 5nm thick grain boundary. In addition to para- and ferromagnetic grain boundaries, calculations with a (nearly)

non-magnetic grain boundary have been performed. These calculations represent the case of perfectly exchange decoupled grains. The grains are only coupled via the long-range dipolar interaction described by the stray field.

The small, non-zero moment in the non-magnetic grain boundary phase in table 14 has numerical reasons. The micromagnetic solver uses *normalized* magnetization vectors. Normalizing them with a total saturation of zero would lead to a singularity [69].

The simulations show that para- and ferromagnetic grain boundaries reduce the coercivity and that ferromagnetic grain boundaries leave the remanence intact. The stray field from the hard magnetic grains is enough to reverse the magnetization of paramagnetic grain boundaries leading to a reduction of the remanent magnetization. However, models with paramagnetic grain boundaries have a higher coercivity than models with ferromagnetic grain boundaries (see fig. 33).

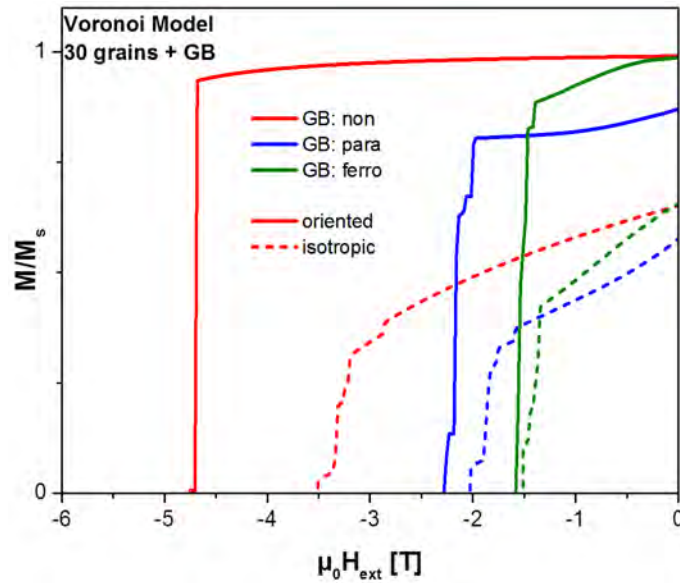


Fig. 33: Demagnetization curves of oriented (solid) and isotropic (dashed) grain structures with a non- (red), para- (blue), and ferromagnetic (green) grain boundary [145].

The oriented and isotropic structures have similar coercive fields, which is consistent with experiments on real $\text{Nd}_2\text{Fe}_{14}\text{B}$ magnets but it seems to contradict the Stoner-Wohlfarth model. However, the truth is that these structures are simply out of scope of the Stoner-Wohlfarth model which only applies to a single domain particle

with a homogenous demagnetizing field (spheres and ellipsoids) [81]. It is actually more surprising that the Stoner-Wohlfarth model correctly predicted the coercivity of the perfectly exchange coupled grains as discussed before.

The simulations show that the models with non-magnetic grain boundaries exhibit the highest coercive field. A way to improve existing $\text{Nd}_2\text{Fe}_{14}\text{B}$ based magnets would be to magnetically decouple the grains by introducing a "non-magnetic" (paramagnetic with nearly zero saturation magnetization) grain boundary phase.

4.3.3. Platelets with and without Grain Boundary

Platelet structures with and without a grain boundary phase have been generated based on the same Voronoi model as the grain structures (see fig. 28). The platelet structures have the same material parameters (table 14) and the same easy axis distributions (see fig. 29) as the grain models. The platelets have a mean diameter of 100nm and a mean thickness of 20nm . The grain boundary is on average 5nm thick.

Both perfect coupling and perfect decoupling maximize the coercivity of the oriented models (see fig. 34a). Para- and ferromagnetic grain boundaries reduce the coercivity by inducing an early nucleation in the hard magnetic platelets. Similar to the grain models, paramagnetic grain boundaries lead to higher coercivity but lower remanence than ferromagnetic grain boundaries. In contrast to the grain structures, ferromagnetic grain boundaries also decrease the remanence of platelet structures because the volume fraction of the grain boundaries is higher in the platelet structures than in the grain structures.

In the isotropic case, the coupling has a lesser effect on the coercivity compared to the oriented platelets (see fig. 34b). The coercivity of the perfectly coupled structure depends on the platelet with the largest misorientation, similar to the findings on the grain structures. Para- and ferromagnetic grain boundaries hardly reduce the coercive field, but decrease remanence and squareness of the hysteresis loop. The only way to improve coercivity in the isotropic case is the magnetic decoupling of the platelets.

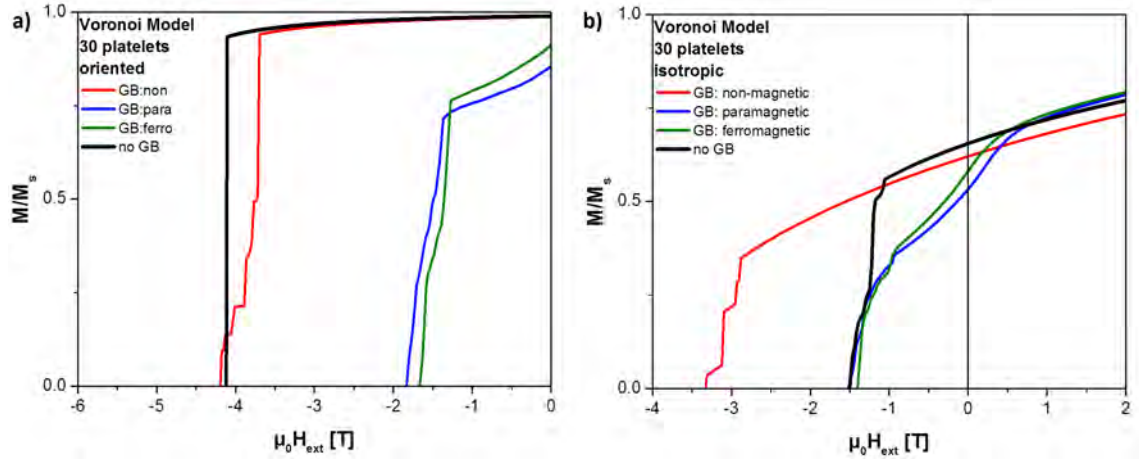


Fig. 34: Demagnetization curves of (a) oriented and (b) isotropic platelet structures with perfect exchange coupling (no grain boundary, black), perfect exchange decoupling (non-magnetic grain boundaries, red), para- (blue) and ferromagnetic (green) grain boundaries.

4.3.4. Microstructural Parameter Analysis

Kronmüller's equation (4.2) is a phenomenological model to describe the experimentally measured coercivity of magnets [33]. The parameter α describes the effective reduction of the anisotropy field due to misorientation and interaction between grains, the parameter N_{eff} is the effective demagnetization factor.

$$H_c = \alpha \cdot H_A - N_{eff} \cdot M_s \quad (4.2)$$

Usually the microstructural parameters α and N_{eff} are obtained by linear fitting experimental data in a so-called *Kronmüller plot* (for example in [41, 43, 112]) but the ability to switch off the calculation of the demagnetizing field makes it possible to calculate the microstructural parameters exactly:

$$\begin{aligned} H_{c,OFF} &= \alpha \cdot H_A - \overbrace{N_{eff}}^{=0} \cdot M_s \Rightarrow \alpha = \frac{H_{c,OFF}}{H_A} \\ H_{c,ON} &= \underbrace{\alpha \cdot H_A}_{H_{c,OFF}} - N_{eff} \cdot M_s \Rightarrow N_{eff} = \frac{H_{c,OFF} - H_{c,ON}}{H_A} \end{aligned} \quad (4.3)$$

Table 15 summarizes the coercive field obtained from grain and platelet models and table 16 extracted α and N_{eff} from these results.

	oriented			isotropic		
	$H_{c,OFF}$	$H_{c,ON}$	ΔH_c	$H_{c,OFF}$	$H_{c,ON}$	ΔH_c
grains						
<i>no GB</i>	4.909	4.597	-0.312	1.787	1.139	-0.648
<i>GB:non</i>	5.537	4.756	-0.781	3.846	3.512	-0.334
<i>GB:para</i>	2.744	2.282	-0.462	2.379	2.031	-0.348
<i>GB:ferro</i>	1.922	1.581	-0.341	1.879	1.513	-0.366
platelets						
<i>no GB</i>	4.980	4.140	-0.840	1.865	1.499	-0.366
<i>GB:non</i>	5.538	4.192	-1.346	3.846	3.327	-0.519
<i>GB:para</i>	2.308	1.830	-0.478	1.742	1.523	-0.219
<i>GB:ferro</i>	2.107	1.669	-0.438	1.714	1.399	-0.315

Table 15: Summary of grain and platelet structures. $H_{c,OFF}$ is the coercivity obtained when the calculation of the stray field is switched off, $H_{c,ON}$ is the result of a full micromagnetic simulation. The influence of the stray field is quantified by the difference ΔH_c between these two calculations.

	oriented		isotropic	
	α	N_{eff}	α	N_{eff}
grains				
<i>no GB</i>	0.642	0.194	0.234	0.402
<i>GB:non</i>	0.724	0.485	0.503	0.207
<i>GB:para</i>	0.359	0.287	0.311	0.216
<i>GB:ferro</i>	0.251	0.212	0.246	0.227
platelets				
<i>no GB</i>	0.651	0.522	0.244	0.227
<i>GB:non</i>	0.724	0.836	0.503	0.322
<i>GB:para</i>	0.302	0.297	0.228	0.136
<i>GB:ferro</i>	0.275	0.272	0.224	0.196

Table 16: Microstructural parameters of grain and platelet structures. The parameters are directly calculated from the coercivity values with and without stray field from table 15 with equation (4.3)

The obtained parameters are in good agreement with other theoretical work ($\alpha = 0.2 - 0.3$, $N_{eff} = 0.2 - 2$) [44] but experimental values have a much higher variance. Kou et. al reported $\alpha = 0.59 \dots 0.85$ and $N_{eff} = 1.01 \dots 2.45$ at temperatures below $175K$ and $\alpha = 0.18 \dots 0.26$ and $N_{eff} = -0.61 \dots 0.09$ at temperatures above $220K$ [41]. Bauer et al. showed that increasing the wheel speed in the melt-spinning procedure reduces and that the annealing treatment increases both parameters ($\alpha = 0.88 \dots 1.02$, $N_{eff} = 0.77 \dots 0.95$) [43]. Yu et al. demonstrated that Dy doping increases α from 1.39 to 1.67 and N_{eff} from 1.75 to 2.31 [112].

The variation of the microstructural parameters α and N_{eff} with different grain boundary types is relatively high for the oriented models. This is because they theoretically have high coercivity values due to the small misorientation angles, but suffer high coercivity losses with the introduction of para- and ferromagnetic grain boundaries.

The effective demagnetization parameter N_{eff} for the oriented grain structures is higher compared to the oriented plane structures. This effect is attributed to the negative shape anisotropy contribution of oblate particles [145]. However, the reverse effect is observed at the isotropic models with para- or ferromagnetic grain boundaries: The oblate platelets exhibit lower demagnetization parameters N_{eff} than the round grains.

Changing the easy axis distribution from oriented to isotropic does not only change the parameter α (as expected) but also the effective demagnetization factor N_{eff} . N_{eff} is commonly associated with the shape of the magnetic grains which does not change in the models. However, the isotropic easy axis orientation also changes the micromagnetic magnetization structure at low fields. This change leads to a differently shaped demagnetizing field that is described by a new demagnetization factor N_{eff} .

If para- or ferromagnetic grain boundaries are present, the change from oriented to isotropic distribution lowers both parameters α and N_{eff} . This effect plausibly explains how it is possible that isotropic magnets exhibit a higher coercivity than oriented magnets in experiment.

If the loss due to the misorientation ($\alpha_{ori} > \alpha_{iso}$) is smaller than the gain due to the changed demagnetizing field structure ($-N_{eff,ori} < -N_{eff,iso}$), the overall coercivity of the isotropic magnet is higher. However, we have not seen this effect in our micromagnetic simulations yet.

4.3.5. Importance of Magnetocrystalline Anisotropy

Magnetocrystalline anisotropy is an important factor for the macroscopic coercivity, because it directly increases the anisotropy field. Fig. 35 summarizes the coercivity of oriented and isotropic platelet structures with varying magnetocrystalline anisotropy. Three value for the anisotropy constant K_1 have been examined: 1.64, 3.30, and 4.90 MJ/m^3 , the other material parameters stayed constant.

Due to the complex grain structure and stray field interactions, the coercivity losses are higher than expected from reduction of the anisotropy field. The obtained coercivities are normalized to the corresponding anisotropy field (2.49, 5.02 and 7.65 T) in fig. 35.

Decreasing the anisotropy from 4.9 to 3.3 MJ/m^3 (32%) decreases the coercivity by 43% for oriented and by 40% for isotropic models. Decreasing the anisotropy from 4.9 to 1.64 MJ/m^3 (66%) decreases the coercivity by 88% for oriented and 79% for isotropic models.

For the softest examined material parameter (1.64 MJ/m^3) the coercivity of the isotropic model surpasses the coercivity of the oriented model. In this case the coercivity losses due to the misorientation are compensated by lower losses due to the demagnetizing field structure.

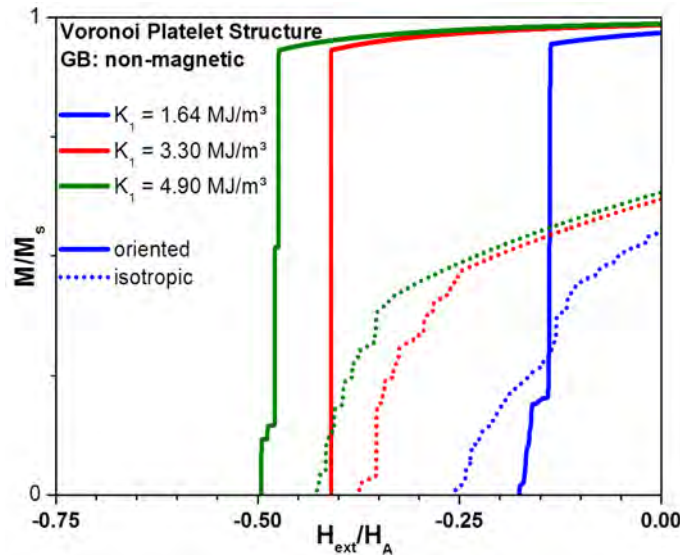


Fig. 35: Normalized coercivity values for different magnetocrystalline anisotropy in oriented and isotropic platelet structures with non-magnetic grain boundaries

4.4. Conclusion

It has been shown that it is possible to quantify and predict the coercive field values of nanocrystalline $\text{Nd}_2\text{Fe}_{14}\text{B}$ magnets by micromagnetic simulations taking into account realistic microstructures. The results are in good agreement with experimentally measured values and micromagnetic simulations are able to quantify the experimentally measured coercivity values of $\text{Nd}_2\text{Fe}_{14}\text{B}$ based magnets. The results suggest that Brown's paradox is a direct consequence of the complex grain structure consisting of hard magnetic grains or platelets separated by para- or ferromagnetic grain boundary phases.

The exchange coupling between the grains and between grains and grain boundaries reduces the coercive field. $\text{Nd}_2\text{Fe}_{14}\text{B}$ magnets could be improved significantly by magnetically decoupling the grains with a "*non-magnetic*" (paramagnetic with very low saturation magnetization by reducing the iron content) grain boundary phase.

Another common paradox result from experiment could be explained: how it is possible that isotropic magnets have higher coercivity than oriented ones. Kronmüller parameter analysis of the simulation results show that the isotropic easy axis distribution indeed reduces the anisotropy field term, however, due to the different magnetization structure in isotropic magnets the structure of the demagnetizing field also changes, which has a positive effect on the coercive field.

This hypothesis has been verified by systematically reducing the magnetocrystalline anisotropy in a simulation of platelet structures, until the stray field effects outweigh the losses due to the misorientation of easy magnetization axes.

5. Micromagnetic Modelling of Nanostructured Permanent Magnets

In the previous chapter the micromagnetic cause of Brown's Paradox has been examined. We found that the grain structure and the grain boundary phases are the reason that only up to 40% of the anisotropy field $H_A = 2K_1/J_s$ are reached as coercivity in real magnets.

The idea of nanostructured magnetic materials is to exploit both shape and magnetocrystalline anisotropy to increase coercivity [15, 61]. The theoretical limits of shape anisotropy effects will be discussed in section 5.1 and compared to simulation results on ideal nanorods. The interaction between two or more nanorods and the limits of the energy density product will be discussed in section 5.2. Section 5.3 contains realistically packed nanorods. The thermal stability of the nanorods are discussed in section 5.4. Two ways to further improve nanostructured permanent magnets are discussed in section 5.5 and the results are concluded in chapter 6.

5.1. Single Nanorods

5.1.1. Analytical Considerations

5.1.1.1. Coherent Rotation

Nanorods are approximately described as an cylindrical single domain particle. The easy axis of magnetization is parallel to the long axis of the particle and perfectly aligned to the external switching field. Assuming coherent rotation as reversal mechanism, the coercive field of an individual particle is expressed as

$$H_c = H_A + H_{sh} = \frac{2K_1}{J_s} + (N_{\perp} - N_{\parallel})M_s \quad (5.1)$$

There is an explicit formula for the demagnetization factors N_{\perp} and N_{\parallel} of ellipsoids. For ellipsoids of revolution with an aspect ratio of n (rotation axis / minor axis) the demagnetization factors are given by [8]:

$$\begin{aligned}
N_{\parallel} &= \frac{1}{n^2 - 1} \cdot \left[\frac{n}{2(n^2 - 1)^{1/2}} \cdot \ln \left(\frac{n + (n^2 - 1)^{1/2}}{n - (n^2 - 1)^{1/2}} \right) - 1 \right] \\
N_{\perp} &= \frac{n}{2(n^2 - 1)} \cdot \left[n - \frac{1}{2(n^2 - 1)^{1/2}} \cdot \ln \left(\frac{n + (n^2 - 1)^{1/2}}{n - (n^2 - 1)^{1/2}} \right) \right]
\end{aligned} \tag{5.2}$$

To evaluate demagnetization factors of cuboids and cylinders, elaborate integrals have to be solved [11, 27] but Sato and Ishii [36] gave approximate solutions for cuboids

$$\begin{aligned}
N_{\parallel} &= \frac{1}{2n - 1} \\
N_{\perp} &= \frac{n}{2n - 1}
\end{aligned} \tag{5.3}$$

and cylinders

$$\begin{aligned}
N_{\parallel} &= \frac{1}{2(2n/\sqrt{\pi}) - 1} \\
N_{\perp} &= \frac{2n/\sqrt{\pi}}{2(2n/\sqrt{\pi}) - 1}
\end{aligned} \tag{5.4}$$

The error of these approximations is at most 6.2% in the range of aspect ratios n between 0.1 and 100. All demagnetization factors fulfill $N_{\parallel} + 2N_{\perp} = 1$ and converge to $N_{\parallel} \rightarrow 0$ and $N_{\perp} \rightarrow 1/2$ for $n \rightarrow \infty$. The theoretical maximum coercivity of an elongated single domain particle is therefore

$$H_{c,max} = \frac{2K_1}{J_s} + \frac{1}{2}M_s \tag{5.5}$$

Anisotropy field and theoretical coercive field for several materials are summarized in table 17.

	anisotropy type	K₁ [kJ/m ³]	K₂ [kJ/m ³]	J_s [T]	μ₀H_A [T]	μ₀H_{c,max} [T]
Fe	cubic	46	15	2.15	0.054	1.129
Ni	cubic	-5	-2	0.61	0.014*	0.319
CoFe	cubic	-15	-0.1	2.45	0.010*	1.235
Fe ₃ O ₄	cubic	-13		0.60	0.036*	0.336
Co	uniaxial	450		1.76	0.643	1.523
MnAl	uniaxial	2150		1.02	5.298	5.808
MnBi min	uniaxial	1350		0.91	3.728	4.183
MnBi max	uniaxial	2250		0.91	6.214	6.669
(Fe _{0.6} Co _{0.4}) ₂ B	uniaxial	1460		1.44	2.548	3.268
Nd ₂ Fe ₁₄ B	uniaxial	4900		1.61	7.649	8.454

Table 17: Anisotropy field and maximum coercive field of an elongated single domain particle for selected materials.

* The anisotropy field for materials with cubic anisotropy and $K_1 < 0$ is $-\frac{4K_1}{3J_s}$ [81]

5.1.1.2. Curling and Buckling

While the assumption of coherent rotation (fig. 36a) is useful to explore the theoretical limits of coercivity, there are losses due to incoherent reversal processes in reality. The most common studied incoherent processes are curling and buckling.

The coercive field for the curling mode (fig. 36b) is given by [66]:

$$H_{c, curl} = \frac{2K_1}{J_s} - N_{\parallel}M_s + 2\pi k \frac{A}{D^2 J_s} \quad (5.6)$$

The parameter k depends on the shape of the nanoparticle and is for our considerations a value between 1.08 (indefinitely long cylinders) and 1.39 (spheres) [13]. Equation (5.6) shows an explicit dependence on the diameter D of the nanoparticle and the exchange stiffness A of the material. The coercive field of the curling mode reversal decreases with increasing diameter, whereas the coercive field of the coherent reversal mode is only dependent on the aspect ratio $n = H/D$.

The coercive field of the buckling mode (fig. 36c) is [66]:

$$H_{c, buck} = \frac{2K_1}{J_s} + \frac{2A}{J_s} \left(\frac{1.84}{R} \right)^2 - \frac{1}{2}M_s(1 - \epsilon[D]) \quad (5.7)$$

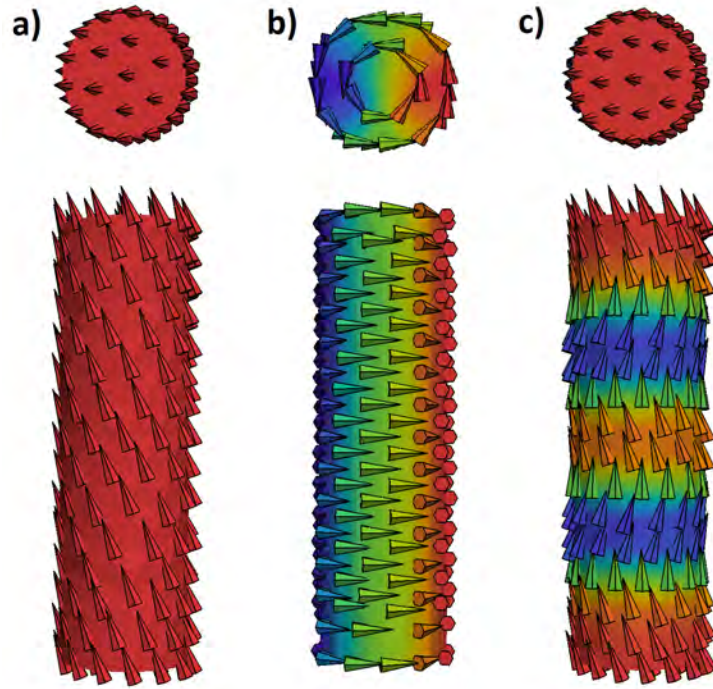


Fig. 36: Schematic illustration of a) coherent rotation, b) curling, c) buckling reversal modes.

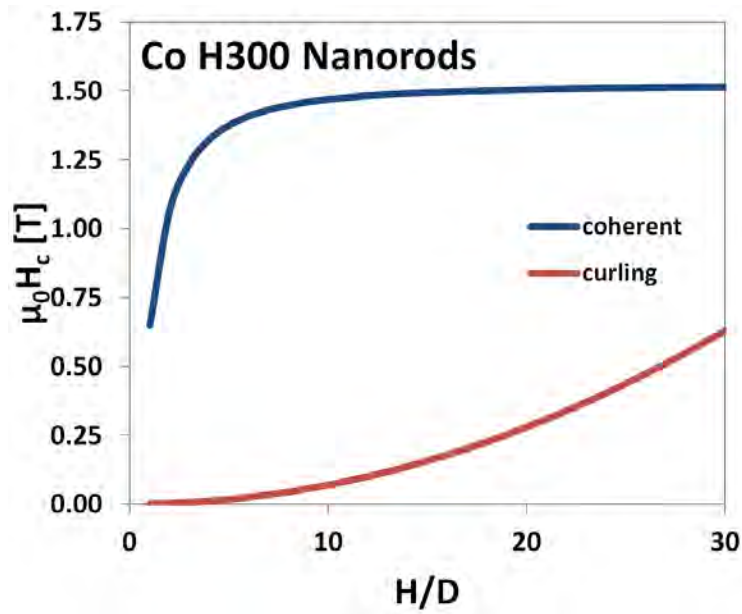


Fig. 37: Analytical coercive fields of coherent rotation (blue) and curling (red) of cylindrical Co nanorods as function of aspect ratio H/D . The height H is held constant at $300nm$.

The parameter $\varepsilon[D]$ models the influence of the alternating surface charges of the buckling magnetization follows a $D^{-2/3}$ law [21].

Figure 37 shows the analytical coercive fields of coherent rotation and curling modes for cylindrical Co nanorods ($K_1 = 450 \text{ kJ/m}^3$, $J_s = 1.76 \text{ T}$, $A = 13 \text{ pJ/m}$) with constant height $H = 300 \text{ nm}$ and varying diameter D and aspect ratio H/D .

The shape anisotropy effect for the coherent reversal mode is already saturated at rather low aspect ratios of around 5 – 10, so nanorods with a length of several hundred of nanometers should have the same coercive fields as nanowires with several micrometers length. The coercive field of the curling reversal mode follows a $1/D^2$ law and approaches zero for $D \rightarrow \infty$ or $H/D \rightarrow 0$ (see fig 37).

5.1.2. Micromagnetic Simulations

Iron and cobalt are inexpensive base materials for producing magnetic nanowires and nanorods [15, 99, 120, 139]. The advantage of Fe and Fe-Co is the higher saturation magnetization, the advantage of Co is the higher and uniaxial magnetocrystalline anisotropy. Micromagnetic simulations on a single, isolated nanorod with diameter $D = 20 \text{ nm}$ and height $H = 400 \text{ nm}$ with different materials show that Co has the highest coercivity of these materials (see fig. 38).

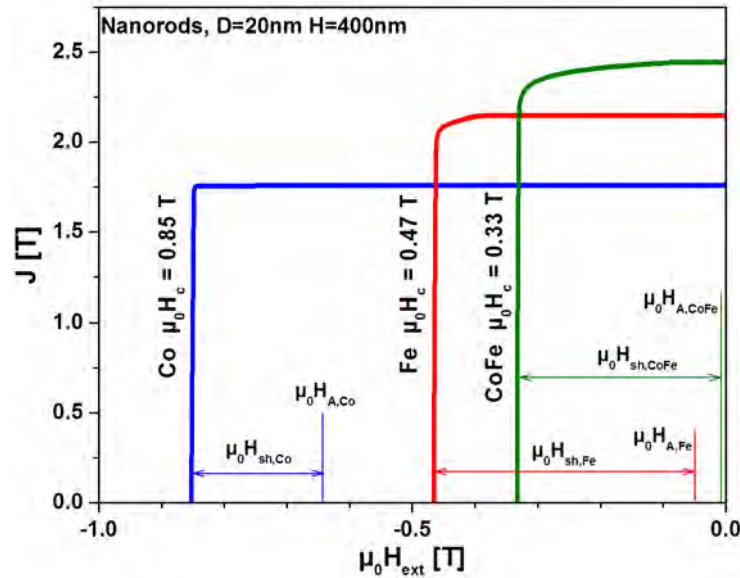


Fig. 38: Anisotropy field H_A and shape anisotropy contribution H_{sh} to the coercivity of Co, Fe and CoFe nanorods

The coercivities obtained from micromagnetic simulations are lower than the analytical results (see table 17) although the shape anisotropy effect should easily be saturated at aspect ratios H/D of 20 (see fig. 37). The reason are incoherent reversal mechanisms. The nucleation starts at the tips of the nanorods as vortex structure. As the external field increases, the vortices form a reversed domain separated by a domain wall. The domain walls move toward the center and annihilate when the magnetization of the nanorod is fully reversed (see fig 39).

Fe nanorods show broader and more stable vortex structures than Co nanorods, because of the cubic anisotropy. The x , y and z axes are equally easy axes and therefore it is more energetically more favorable to align the moments completely in-plane. The rounded demagnetization curves of Fe and CoFe in fig. 38 hint at the formation of the vortex seen in fig. 39.

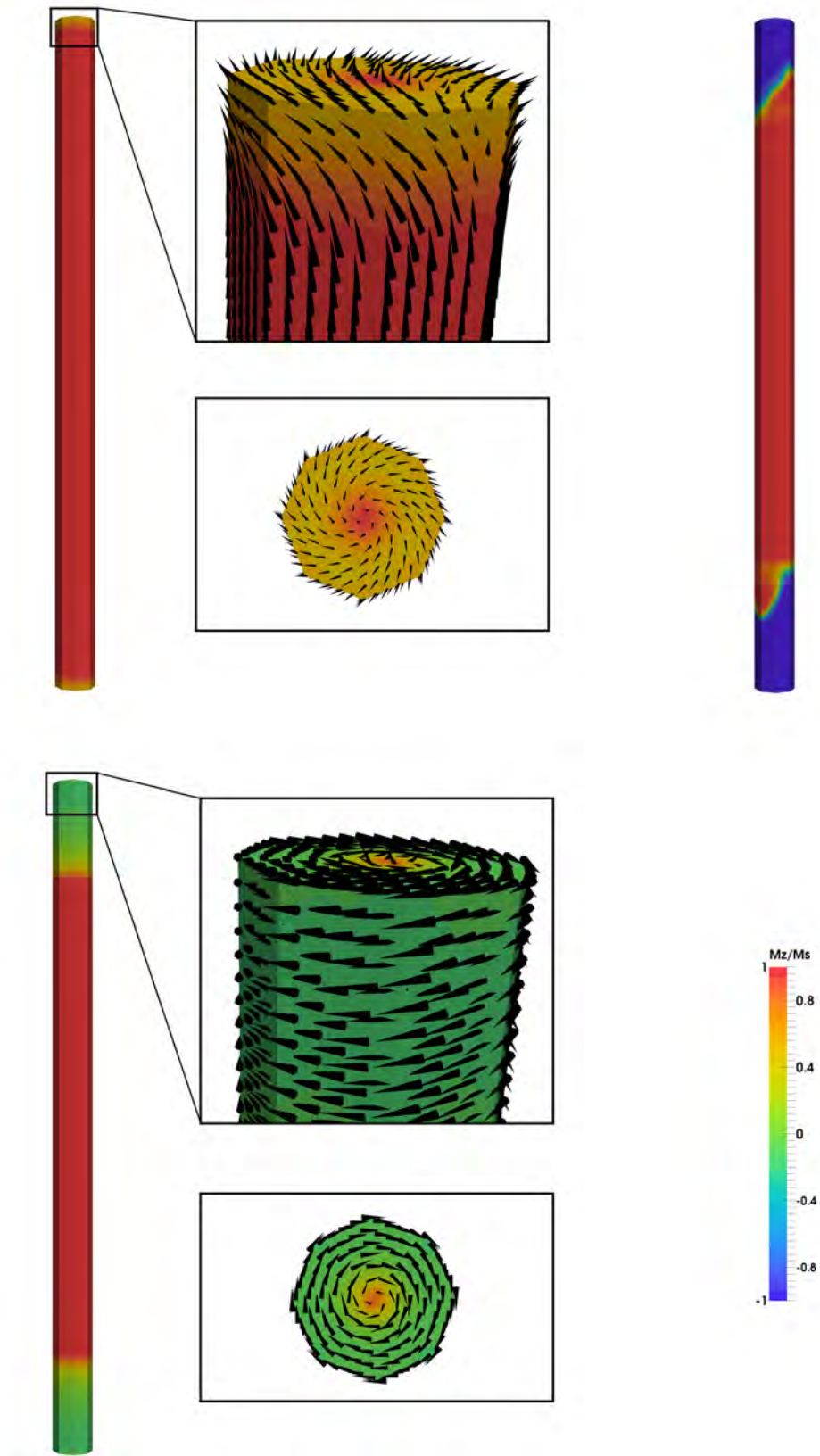


Fig. 39: Incoherent reversal processes in Co (top) and Fe (bottom) nanorods with $D = 30\text{nm}$ and $H = 1000\text{nm}$. The nucleation starts as vortex structure at the tips and ends as domain wall propagation through the nanorod

5.1.3. Influence of Aspect Ratio

Out of the three candidates, Co seems the most promising material because of its high shape and magnetocrystalline anisotropy contribution to coercivity. The next step is optimizing the shape of the nanorod in order to maximize the coercivity.

The simulation result in fig. 38 shows that that only 53% of the maximum possible coercivity is reached although analytically the shape anisotropy contribution saturates around $H/D = 5$.

Simulations of nanorods with $H = 300nm$ on a wider array of aspect ratios H/D have been performed. The results show that increasing the aspect ratio beyond 20 increases the coercivity. The simulation results lay between the theoretical predictions of coherent rotation and the curling mode (see fig 40a), implying that the magnetization reversal is a mixture of these reversal mechanisms as seen in fig. 39.

The next step is the variation of the nanorod height. Micromagnetic simulations on nanorods with height $H = 100, 600nm$ and the same diameters $D = 10, 15, 20, 25, 30, 40, 60nm$ used for $H = 300nm$ have been performed. The results show the paradox behavior that longer nanorods need higher aspect ratios in order to maximize the coercive field (see fig. 40b). However, grouping the same data not by height, but per diameter (fig. 40c) shows that the coercivity depends primarily on the diameter. $D10$ nanorods have a constant coercive field that is higher than the coercivity of $D15$ nanorods over the examined range of aspect ratios. Only nanorods with large diameters $D \geq 40nm$ profit from aspect ratios $H/D > 50$ (fig. 40d).

The reason is the formation of vortices at the tips of the nanorods. As analytically calculated, the vortices nucleate at lower external fields as the diameter increases (equation (5.6), fig. 40a). The curling mode dominates the nucleation process in the nanorods, but not the whole switching process. This is the reason the micromagnetic simulations show this strong relationship between coercivity and diameter, but with higher coercive fields than predicted by the analytical solutions for the curling reversal mode.

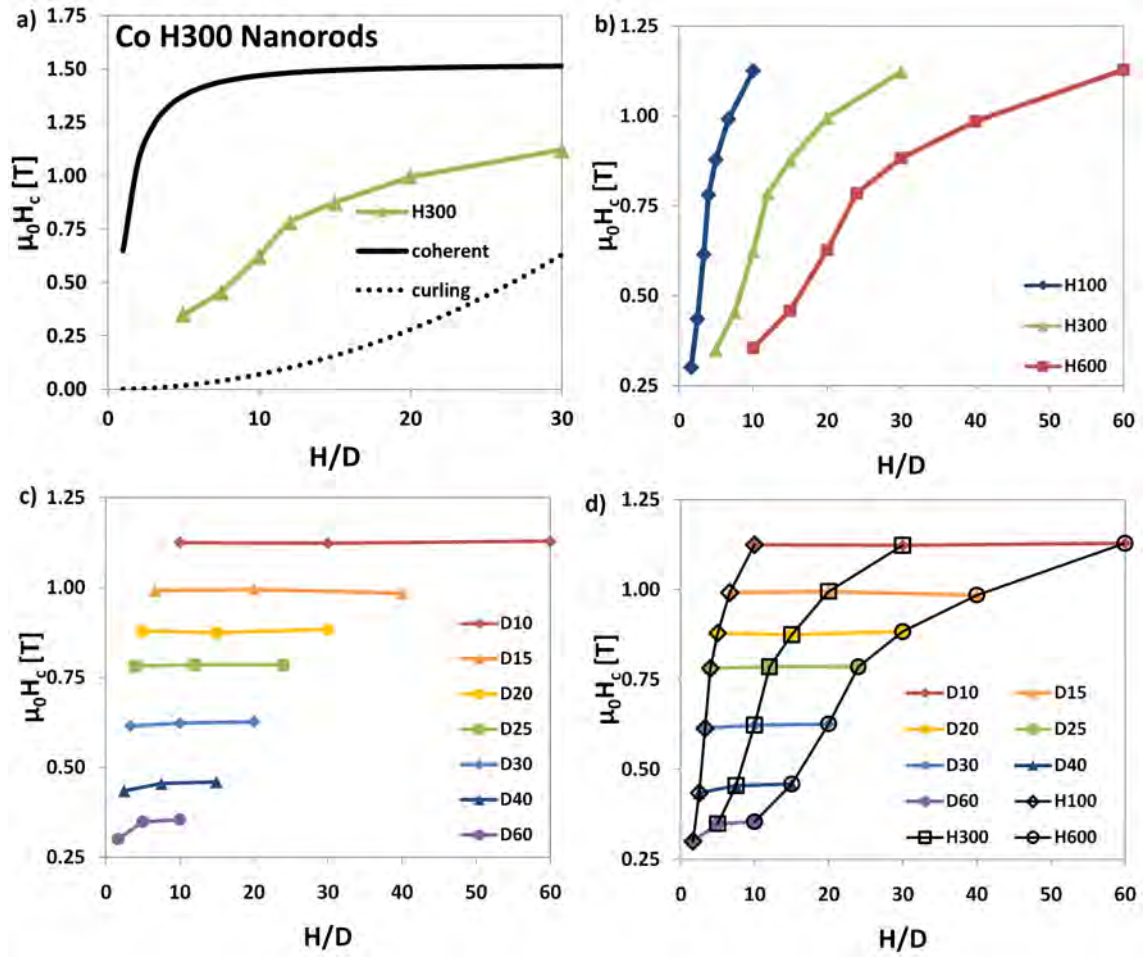


Fig. 40: a) Simulation results of single Co nanorods with height $H = 300\text{nm}$ and different diameters compared to analytical calculations. b) Coercivity of single Co nanorods with different height H and diameter D as function of aspect ratio H/D . c) Same data as in (b), but grouped by diameter instead of height. d) Overlay of (b) and (c).

5.2. Regular Nanorod Arrangements

5.2.1. Magnetostatic Interaction Between Nanorods

After the properties of single, isolated nanorods have been determined, the interactions between nanorods were examined. The simplest case are two nanorods with perfect alignment as shown in fig. 41a. The nanorods with height H and diameter D are displaced by a center-to-center distance d or a surface-to-surface distance $\Delta = d - D$ along the x axis.

The coercive fields of two $D10H100$, $D20H100$ and $D30H100$ nanorods with varying distance Δ are summarized in fig. 41b. The interaction between the nanorods lowers the coercive field and with higher distance between the nanorods the coercive field increases. The value obtained from a single nanorod simulation acts as upper limit for the coercivity.

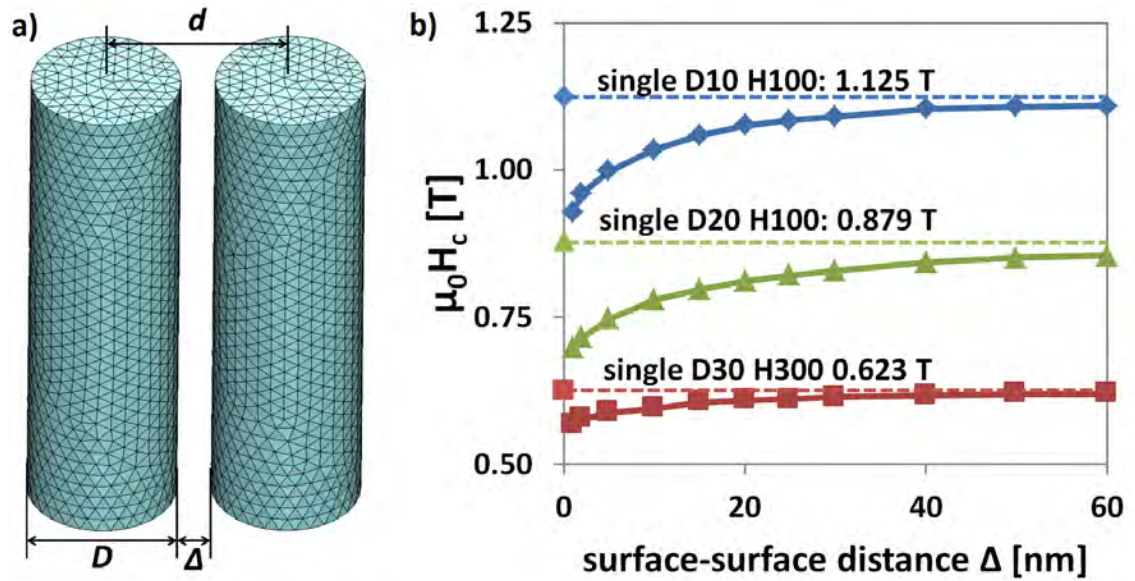


Fig. 41: a) Diameter D , center-center-distance d and surface-surface-distance Δ of two interacting nanorods. b) Coercivity as function of distance Δ of two nanorods with varying diameters.

Nanorods with a lower diameter exhibit higher losses due to the stray field interaction. This can be explained by the fact that two competing factors – the shape anisotropy and stray field – have the same source: the magnetostatic interaction. The coercivity increase for thinner nanorods is higher than for thicker nanorods, therefore the coercivity losses are higher if the shape of the stray field changes.

The role of the magnetostatic interactions has been confirmed in simulations without demagnetizing field calculation. Without the demagnetizing field, all simulations yielded the anisotropy field $\mu_0 H_{A,Co} = 0.64T$ as coercivity, regardless of diameter, height or distance.

The trend that nanorods with a lower diameter have higher coercive fields, but also suffer higher coercive losses due to magnetostatic interactions can be observed over a wider range of nanorod dimensions (see fig. 42).

The nanorod height (and therefore the aspect ratio H/D) has only a minor influence on the coercivity of two interacting nanorods. Increasing the height from $100nm$ to $600nm$ slightly increases the coercivity of the $D40$ nanorods, because the aspect ratio of the $D40H100$ ($H/D = 2.5$) is not sufficient to saturate the shape anisotropy effect (compare fig. 42 a and b).

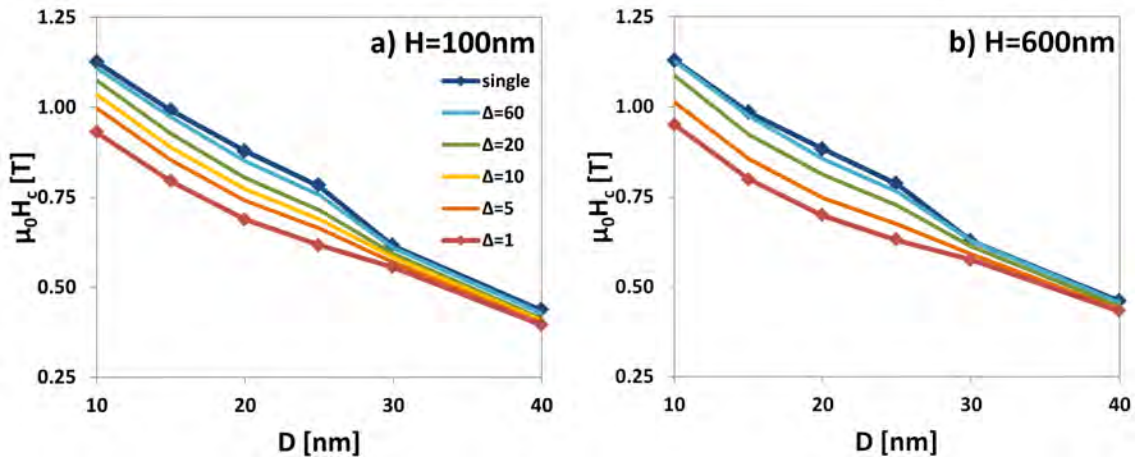


Fig. 42: Coercive field of two interacting Co nanorods with a height of $100nm$ (a) and $600nm$ (b) with varying diameter and surface-surface distance. The distance is color-coded from $1nm$ (red) to $60nm$ (teal); the blue curves are results from a single nanorod and the upper limit of coercivity for indefinite distances.

5.2.2. Influence of Packing Density

After the interactions between two perfectly aligned nanorods has been studied, the next step is to examine an ensemble of many nanorods. In a first approximation we assume the packing of aligned nanorods in a perfect hexagonal or quadratic lattice. Such ensembles can be created by nanolithography or filling porous anodic alumina templates by electro-deposition with a wide range of materials [61, 96, 99, 139].

While this production route is not suitable to create bulk magnets, it has its applications in microsensoric and spintronic devices, bit-patterned recording media and magnetic random access memory [48, 72].

The packing density of a perfect arrangement of nanorods or nanowires is calculated by dividing the area of the nanorod's base circle of the nanorod through the area of the surrounding hexagonal or quadratic cell (see fig. 43):

$$p_{hex} = \frac{D^2\pi}{2d^2\sqrt{3}} \quad p_{quad} = \frac{D^2\pi}{4d^2} \quad (5.8)$$

Example packing densities calculated with (5.8) are found in fig. 43.

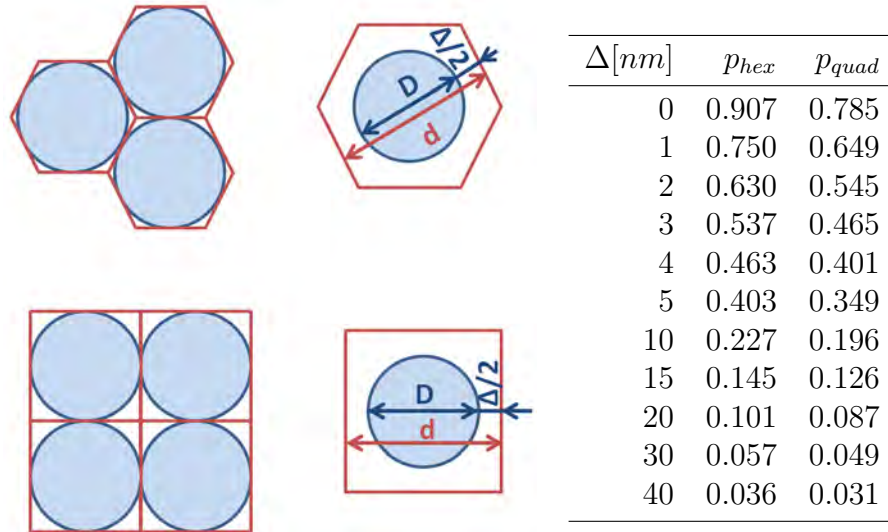


Fig. 43: Calculation of packing density for a regular packing of nanorods in a hexagonal or quadratic grid. The table lists packing densities for $D = 10nm$

Assuming that the coercivity does not change with the number of neighboring nanorods and a perfectly rectangular hysteresis loop, the maximum energy density product is given by [123, 147]:

$$(BH)_{max} \approx \begin{cases} B_r^2/4\mu_0 & \text{if } \mu_0 H_c \geq B_r/2 \\ (B_r - \mu_0 H_c)H_c & \text{if } \mu_0 H_c \leq B_r/2 \end{cases} \quad (5.9)$$

where the flux density at the remanence has to be scaled down by the magnetic volume fraction or packing density p : $B_r = p \cdot J_s$.

Using the dependence of packing density on the distance between nanorods (5.8), the results in the previous section (coercivity as function of distance) have been transformed to coercivity as function of packing density (see fig. 44). The coercivity at $p = 0$ has been obtained from the simulation of a single nanorod, the coercivity at $\Delta = 0$ has been extrapolated from the data with non-zero Δ .

The energy density product $(BH)_{max}$ shows a perfect quadratic behavior as function of packing density p because the condition $\mu_0 H_c \geq B_r/2 = pJ_s/2$ is fulfilled over all distances Δ and packing densities p .

Theoretical calculations only based on shape anisotropy predict the optimal packing density at $p = 2/3$. This optimum moves to higher packing densities if magnetocrystalline anisotropy $K_1 > 0$ is present [89]. However, packing densities in this order would require very small mean distances between nanorods (compressed nanorod powder) or very thin template walls (electro-deposited nanorods).

Realistic packing densities of cylindrical nanorods are in the order of 40 – 60% [87, 104, 114, 147]. At packing densities around 50%, energy density products in the order of $200 \text{ kJ}/\text{m}^3$ are possible to reach in Co-based nanostructured magnets.

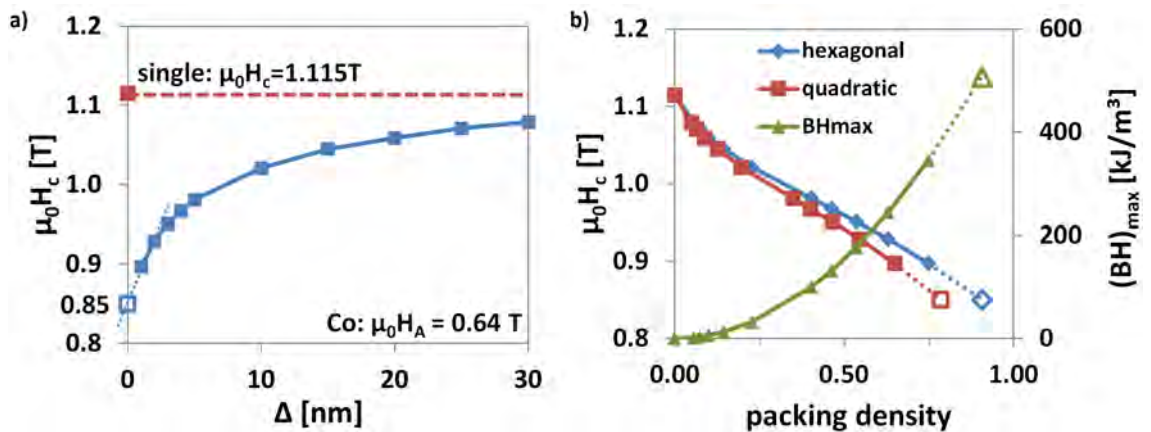


Fig. 44: a) Coercivity of Co *D10H100* nanorods as function of surface-surface-distance Δ . b) Coercivity and predicted maximum energy density product of regularly packed *D10H100* nanorods [147].

To confirm that the distance between nanorods is the key factor that reduces coercivity, micromagnetic simulations on regular matrices of nanorods with hexagonal and quadratic packing have been performed (see fig. 45a). Two different types of models have been created: nanorod matrices with perfect alignment and matrices with a small misalignment. The misalignment angle is measured between the long cylinder axis and the z axis and follows a Gaussian distribution with a standard deviation $\sigma = 1.7^\circ$

Fig. 45b plots the coercive field of the matrix structures consisting of *D20H100* nanorods as function of the inverted surface-surface distance Δ^{-1} . At $\Delta^{-1} = 0$, the value of a single nanorod is shown. The difference between hexagonal and quadratic matrices is negligible and in the same order than misorientations in the order of $\pm 1.7^\circ$.

Plotting the same data as function of the packing density (fig. 45c) shows a split between hexagonal and quadratic packing. This splitting occurs because hexagonal structures have a higher packing density than quadratic structures with the same distance between the nanorods.

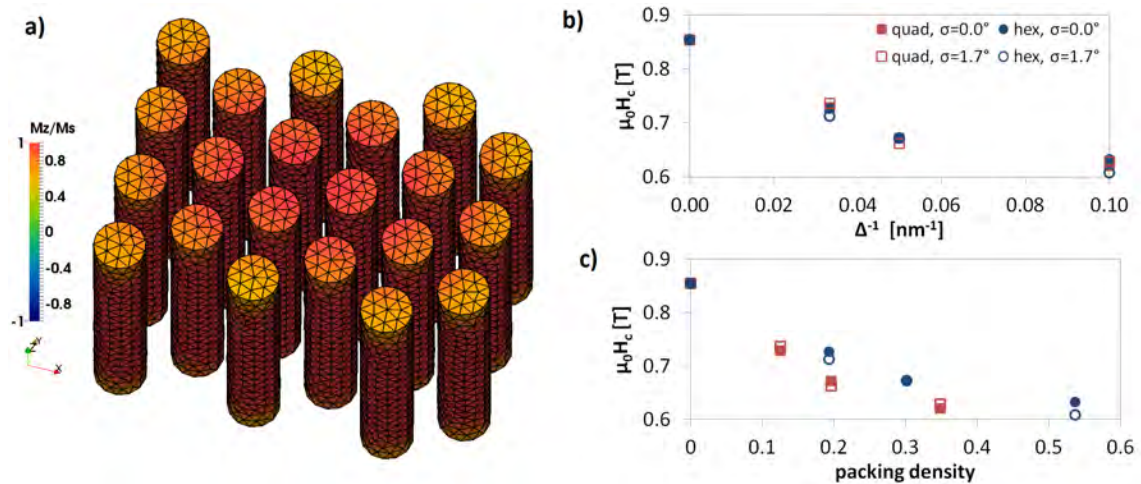


Fig. 45: a) Micromagnetic State of a hexagonal nanorod matrix right before the magnetization reversal in the inner nanorods occurs. b) Coercivities of hexagonal (blue circles) and quadratic (red squares) nanorod matrices with perfect alignment (filled) and small misalignments (open) as function of the inverted surface-surface-distance Δ^{-1} c) Same coercive fields as in (b) but as function of packing density.

In summary, hexagonal nanorod matrices should be preferred because they realize higher coercivities at the same packing density than quadratic matrices. Increasing the packing density by decreasing the distances between the nanorods potentially improves the energy density product, but reduces the coercive field.

The coercive field of *D10* nanorods is high enough to fulfill the condition $\mu_0 H_c > p J_s$ at realistic packing densities around 50%. The *D20* nanorods do not fulfill this condition, which means that the energy density product is not limited by packing density or saturation magnetization, but by the coercive field.

5.2.3. Using Novel Materials

The open question is now how the nanorod or nanowire matrices are improved by using other materials. Micromagnetic simulations on two *D20H100* nanorods with a surface-surface distance $\Delta = 5nm$ (corresponds to a packing density $p = 0.58$ in a hexagonal arrangement) with varying material parameters have been performed. The intrinsic material parameters obtained from the ab-initio calculations presented in chapter 3 and summarized in table 17, p. 63 have been used as input for these simulations. For comparison, simulations on $Nd_2Fe_{14}B$ nanorods have been included as well.

The first two columns in table 18 are theoretical energy density products based on the saturation polarization and packing density:

$$(BH)_{max}^p = \frac{(p \cdot J_s)^2}{4\mu_0} \quad (5.10)$$

The last energy density product in table 18 is based on the simulation results as calculated by equation (5.9). The column "*cond.*" is derived from the condition in equation (5.9):

$$cond. = 2\mu_0 \cdot H_c - p \cdot J_s \quad (5.11)$$

If $cond. < 0$, the energy density product is limited by the coercivity. The energy density product could potentially improved by lowering the diameter of the nanorods (and keeping the packing density constant) or by improving the magnetocrystalline anisotropy of the material without lowering the saturation polarization.

If $cond. > 0$, the energy density product is limited by the packing density or the saturation polarization. While the shape anisotropy of the nanorods improves the coercivity, much of the potential energy density product is lost due to the packing alone (see fig. 46).

With $p = 0.58$ the energy density product of $Nd_2Fe_{14}B$ is limited at $174kJ/m^2$, a value that is below sintered or melt-spun $Nd_2Fe_{14}B$ magnets [86] and has been experimentally reached using Co nanorods [114, 120], which makes this production route with rare-earth containing materials unattractive.

	<i>theory</i>		<i>simulation</i>		
	$(\mathbf{BH})_{\max}^{p=1}$ [kJ/m ³]	$(\mathbf{BH})_{\max}^{p=0.58}$ [kJ/m ³]	$\mu_0 \mathbf{H}_c$ [T]	<i>cond.</i> [T]	$(\mathbf{BH})_{\max}$ [kJ/m ³]
Co	616	208	0.741	0.230	208
MnAl	207	70	5.111	4.815	70
MnBi min	165	55	3.647	3.383	55
MnBi max	165	55	6.031	5.767	55
(Fe _{0.6} Co _{0.4}) ₂ B	413	139	2.376	1.958	139
Nd ₂ Fe ₁₄ B	516	174	7.016	6.548	174

Table 18: Theoretical energy density products of hexagonal *D20H100* nanorod matrices with a surface-surface distance $\Delta = 5nm$ and a packing density $p = 0.58$. Material parameters and predicted coercive fields are summarized in table 17, p. 63

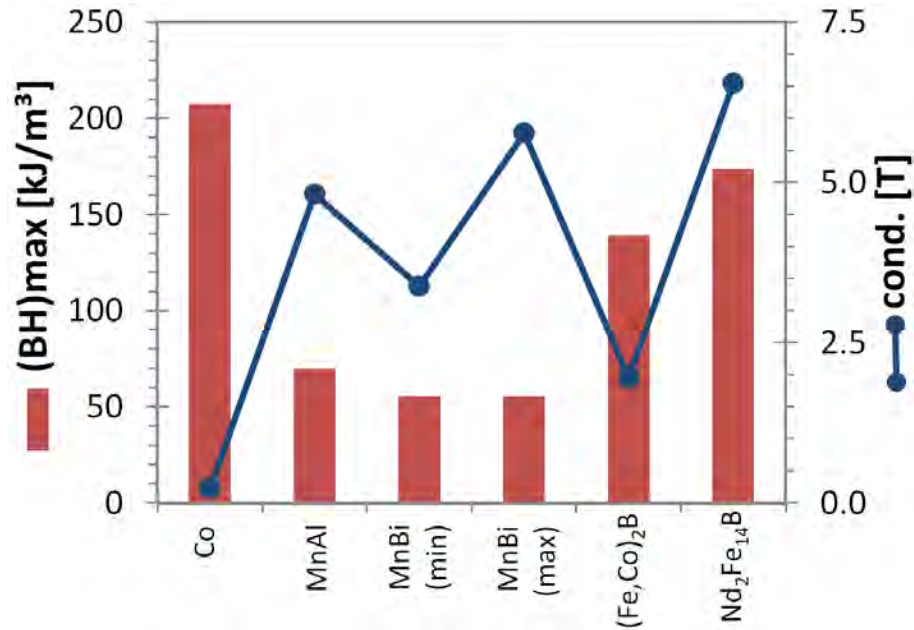


Fig. 46: Energy density products (red) of hexagonal *D20H100* nanorod matrices with a packing density $p = 0.58$ for various materials. The sign of $cond. = 2\mu_0 H_c - pJ_s$ (blue) is an indication of the limiting factor of the energy density product. $cond. > 0$ means that the limiting factors are packing density and/or saturation polarization. Higher values of $cond.$ indicate higher potential increases of the energy density product by increasing the packing density and/or saturation polarization.

5.3. Irregularly Packed Nanorods

The results obtained from micromagnetic models of nanorod matrices are interpreted as a model of nanorods created by electro-deposition and as a study of the upper limits of remanence, coercivity and energy density product of nanostructured permanent magnets.

Besides electro-deposition and lithography there is another approach to create nanorods: wet chemistry. Co-laureate is dissolved in NaOH and 1,2-butanediol and mixed with Ruthenium-Chloride particles that act as nucleation sites. Under the right temperature conditions, hcp Co nanorods crystallize in the solution. The result are single crystal Co nanorods with tunable diameter and height[85]. The nanorods are processed to nanostructured magnets by drying and compacting under a external field [114, 120].

The advantage of this route is that it easier to realize higher packing densities, because this production-route is template-free. The disadvantage is the irregular packing with misalignments lowering the coercive field and remanence [104, 131].

5.3.1. Model Creation

5.3.1.1. Packing of Nanorods

The micromagnetic model is created with a packing algorithm based on the *bullet* physics library [101]. The advantage of the bullet library is that it supports collision detection of basic geometries (cubes and cuboids, spheres and ellipsoids, cylinders) natively and allows easy implementation of custom forces and torques in C++. The library has a strong focus on real-time applications suitable for cross-platform computer games, but it is possibly to sacrifice the real-time capabilities for precision. The bullet physics library has been successfully used for the packing of nanoparticles, for example for granular recording media [87].

The packing algorithm starts with a loose, unaligned arrangement of nanorods (fig. 47a). The nanorods are packed with gravity and collision forces until an equilibrium state has been found (fig. 47b). The positions, normalized orientation vectors, and sizes of the nanorods are written to a simple, semicolon-separated file:

```

pos-x;pos-y;pos-z;ori-x;ori-y;ori-z;size-x;size-y;size-z;
pos-x;pos-y;pos-z;ori-x;ori-y;ori-z;size-x;size-y;size-z;
...
pos-x;pos-y;pos-z;ori-x;ori-y;ori-z;size-x;size-y;size-z;

```

The file format and the bullet physics library support cylinders with elliptic bases. It is noteworthy that in bullet physics the long cylinder axis is described by **size-x**. After the cylinder configuration has been saved, the gravity is inverted until a new equilibrium of forces has been found (fig. 47c). In general, each subsequent structure has a better overall alignment than the structures before.

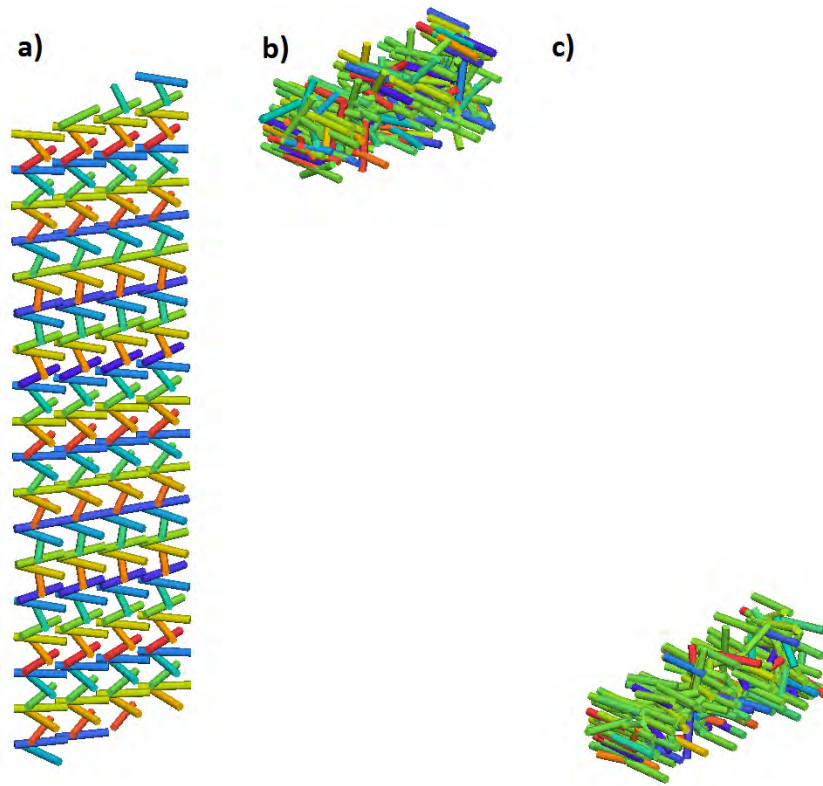


Fig. 47: Packing algorithm based on the bullet physics library. a) Sparse, misaligned starting configuration b) First equilibrium structure c) Second equilibrium structure with better alignment after gravity inversion

Besides performing more gravity inversions, there two other main ways to improve alignment and packing density of the final structure. (1) Using a starting configuration with better alignment. (2) Introducing a torque on each nanorod that aligns the nanorods into the (100) direction. This torque mimics the alignment of magnetic dipoles in an external field.

In order to reduce the influence of the hard wall boundaries on the nanorod structure, the packing algorithm is used on 5000 nanorods. A sub-sample in the order of 200 nanorods is taken from the core packed structure and used as input for the micromagnetic model.

5.3.1.2. Meshing

Two methods to create a mesh of a packed nanorod structures have been implemented. The first implementation is a Python [71] script for Salome [80]. The Salome script reads the nanorod data from the text file and creates cylinders for each entry. The complete structure of nanorods is then meshed at once. The Salome script is also capable of creating the necessary input files for the micromagnetic code FEMME [69]. Particularly important is the `*.krn` file that contains the material parameters. The automatic generation of the `*.krn` file makes it possible to align the easy axis of each nanorod along the long cylinder axis.

The second implementation is a C program called *meshtransform*. *meshtransform* needs a already existing finite element mesh as input and creates multiple copies of the mesh in a single file. The vertices of the mesh are transformed to fit the cylinders in the packed structure. The tetrahedron data has not to be transformed, only their vertex indices increase. The advantage of *meshtransform* over the Salome script is its speed. Meshing structures with 5000 nanorods takes five hours, the same structure can be generated with *meshtransform* in ten seconds. The only disadvantage of *meshtransform* is that it does not check for mesh overlaps so the input data has to be trusted. The micromagnetic simulation on a mesh with overlapping regions will crash.

Both programs use the same transformations to create the mesh of the packed structure. The only difference is that the Salome script applies the transformations on a unit cylinder at the origin and *meshtransform* applies the transformations on each vertex of an already existing cylinder mesh.

The first transformation is a scaling of the mesh to the actual nanorod dimensions. The second transformation is a rotation of the cylinder or mesh into the orientation of the nanorod. The last transformation is a translation of the cylinder to the nanorod's position.

The first step of the rotation is extracting the polar angle θ and the azimuthal angle φ from the orientation vector. These angles can be reused in the generation of the `*.krm` file.

$$\begin{aligned}\theta &= \arccos \frac{z}{\sqrt{x^2 + y^2 + z^2}} \\ \varphi &= \text{atan2}(y, x) = \begin{cases} \frac{\pi}{2} \cdot \text{sgn}(y) & \text{if } x = 0 \\ \arctan \frac{y}{x} & \text{if } x > 0 \\ \arctan \frac{y}{x} + \pi \cdot \text{sgn}(y) & \text{if } x < 0 \end{cases} \end{aligned} \quad (5.12)$$

The $\text{sgn}(x)$ function returns the sign of x and $\text{atan2}(y, x)$ is a helper function available in most programming languages and mathematical libraries that returns angles between $\pm\pi$ in the correct quadrant specified by the coordinates (x, y) .

Geometrically speaking, the polar angle θ describes a rotation around the y axis and the azimuthal angle φ describes a rotation around the z axis. The rotation matrix $R_{\theta, \varphi}$ describing both rotations at once can be calculated by multiplying the two rotation matrices:

$$\begin{aligned} R_{\theta, \varphi} &= \begin{pmatrix} \cos \varphi & -\sin \varphi & 0 \\ \sin \varphi & \cos \varphi & 0 \\ 0 & 0 & 1 \end{pmatrix} \cdot \begin{pmatrix} \cos \theta & 0 & \sin \theta \\ 0 & 1 & 0 \\ -\sin \theta & 0 & \cos \theta \end{pmatrix} \\ &= \begin{pmatrix} \cos \theta \cos \varphi & -\sin \varphi & \sin \theta \cos \varphi \\ \cos \theta \sin \varphi & \cos \varphi & \sin \theta \sin \varphi \\ -\sin \theta & 0 & \cos \theta \end{pmatrix} \end{aligned} \quad (5.13)$$

Transforming the mesh directly has another advantage: it is possible to use different base shapes, such as ellipsoids or prisms, as long as the shape can be inscribed in a cylinder (see fig. 48). The bullet physics library and both meshing programs support the packing of cylinders with a high size distribution (see fig. 49). The implemented packing algorithm can also be used to create packed structures of barium ferrite particles (see fig. 50) used as tape recording media [91, 93].

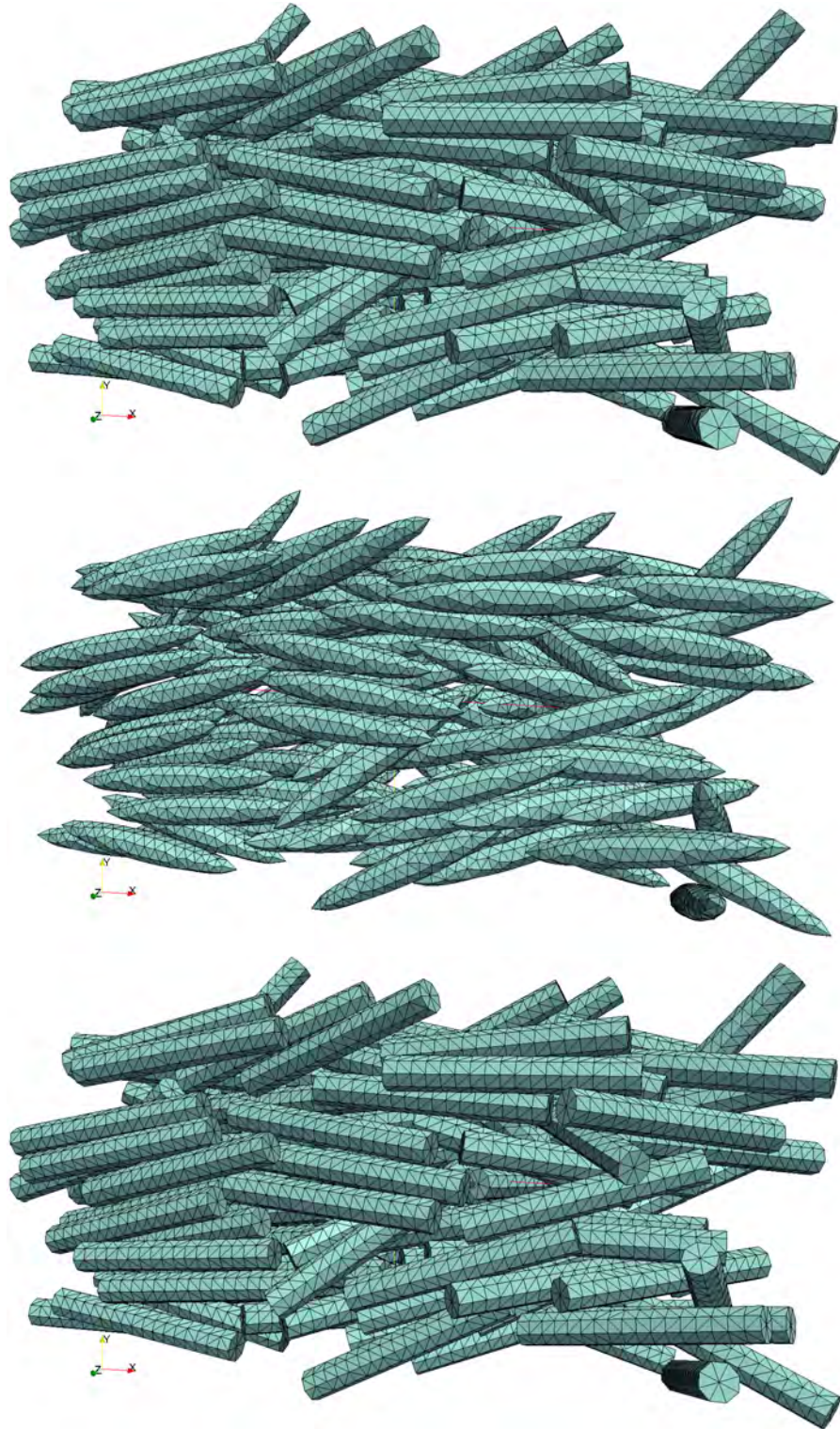


Fig. 48: Finite element mesh of packed cylinders, ellipsoids and prisms based on the same packing simulation of cylinders with $D = 10nm$ and $H = 70nm$.

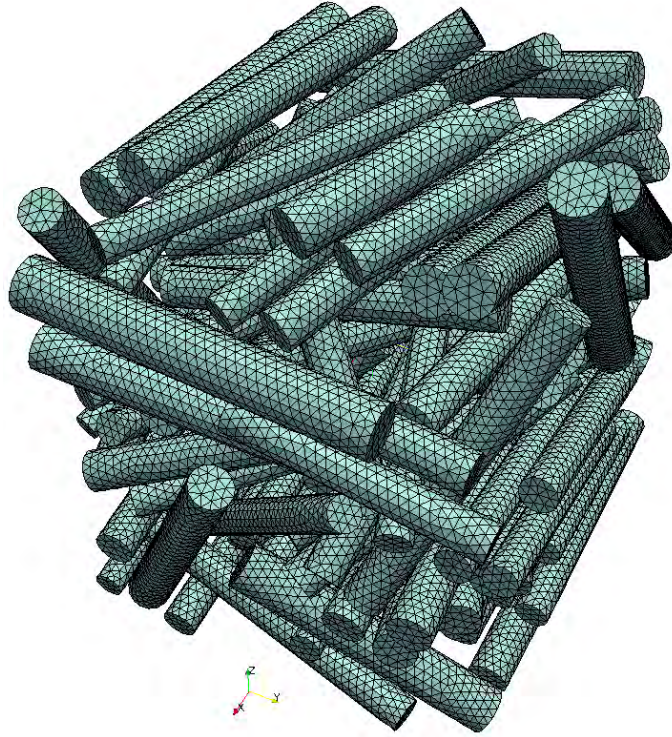


Fig. 49: Packing of cylinders with a high size distribution. Mean diameter and height are $10nm$ and $70nm$, standard deviations of diameter and height are $1nm$ and $10nm$, respectively.

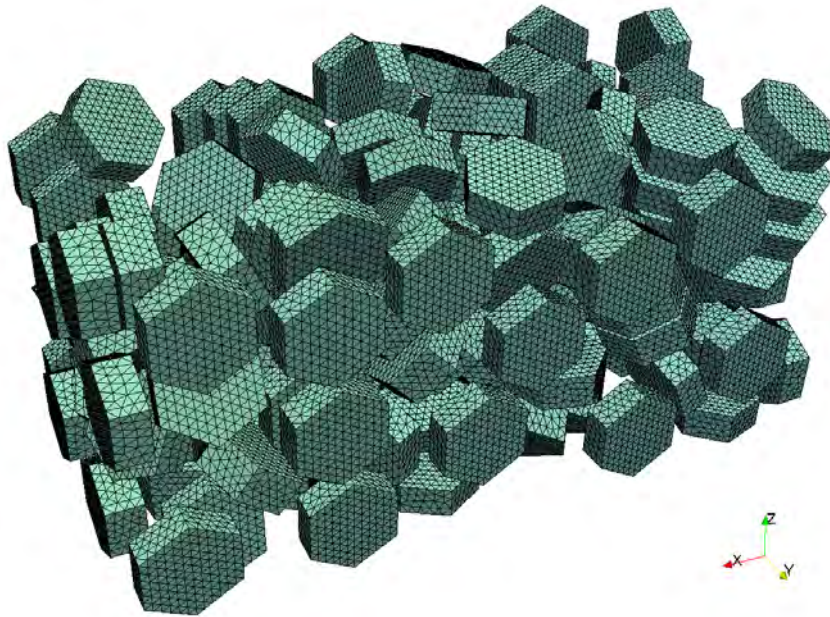


Fig. 50: Packing of hexagonal prisms with $D = 60nm$ and $H = 20nm$.

5.3.2. Results and Discussion

Depending on the starting configuration, the packing algorithm creates nanorod structures with a packing density between 40% and 58%, depending on the starting configuration, the aligning torque and the number of iterations. Fig. 51 shows the evolution of packing density and misalignment of the structure with the number of iterations for different alignment torques.

Fig. 52 shows an example packed structure and the evaluation of the packing density with Paraview [134]. As measurement of misalignment serves the standard deviation of azimuthal angles σ_φ . In a perfectly aligned structure, all nanorods are aligned parallel to the x axis, because the z axis is reserved for the gravity in the bullet physics library.

In general, both packing density and alignment improve with the number of iterations of the algorithm. However, it is possible that the packing density oscillates with the number of iterations, because the nanorod pattern is more beneficial for the "*gravity-up*" than the "*gravity-down*" iteration (or vice-versa, see fig. 51a).

Stronger alignment torques create structures with higher packing density, but also create the problem that the nanorods may interlock causing the oscillating packing density. The alignment of the early iterations is better with a higher alignment torque, but after three iterations the same nanorod alignment can be reached with lower torques as well.

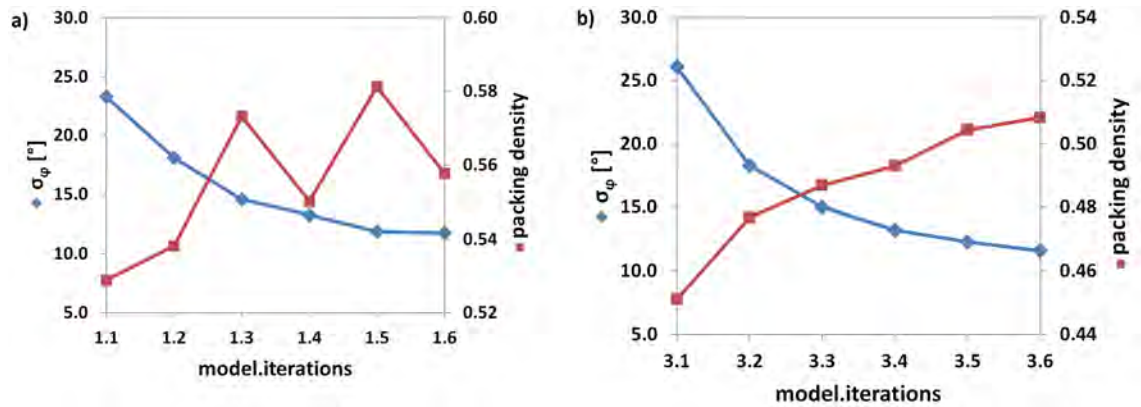


Fig. 51: Evolution of packing density p and misalignment σ_φ as function of the number of iterations. The models use a very misaligned starting configuration and a high (a) or low (b) alignment torque.

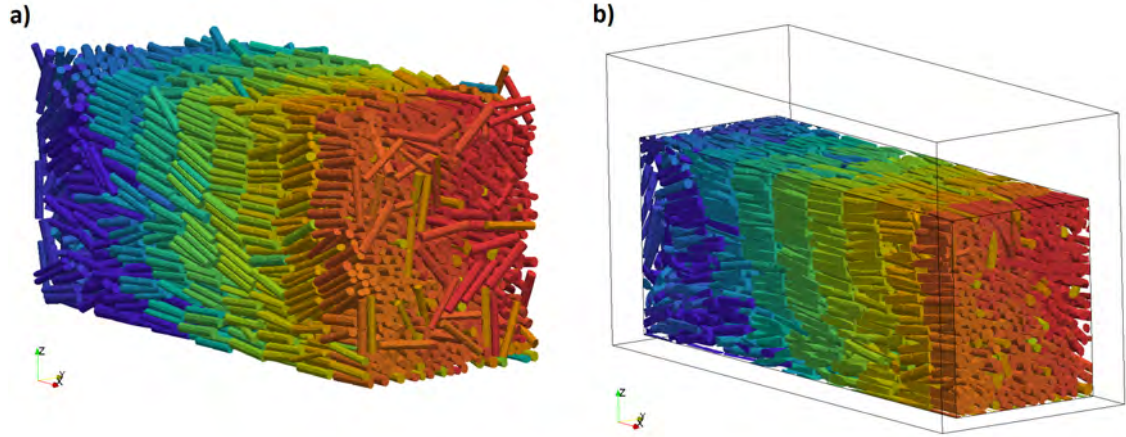


Fig. 52: a) Packed structure containing 4900 nanorods. b) Evaluation of the packing density. A cuboid is cut out of the packed structure to reduce the influence of outliers and the borders of the structure. The magnetic volume fraction of nanorods in this cuboid is automatically determined by *Paraview*.

Three types of micromagnetic simulations have been performed on the packed nanorod structures:

$H_{\text{mag}} = \text{ON}$ is a full micromagnetic simulation including the numerical solution of the demagnetizing field. This simulation type includes all mechanisms contributing to the reversal behavior: magnetostatic (stray field) interactions, magnetocrystalline and shape anisotropy and incoherent reversal processes.

$H_{\text{mag}} = \text{OFF}$ is a micromagnetic simulation omits the calculation of the demagnetizing field and therefore neglects stray field and shape anisotropy effect. The difference of coercive fields between $H_{\text{mag}} = \text{OFF}$ and ON calculations is the gain due to shape anisotropy (Δ_2 in fig. 53b).

macro spin calculations have only one macroscopic magnetic spin per magnetic nanorod. The demagnetizing field is still evaluated in this calculation mode, but all incoherent reversal processes are omitted, because it is not possible to reflect them with a single magnetic moment. The difference to the $H_{\text{mag}} = \text{ON}$ calculation are the losses due to incoherent reversal processes (Δ_1 in fig. 53b).

Micromagnetic simulations on a full packed structure with 4900 nanorods as shown in fig 52 are not feasible due to memory and computational time requirements. Simulations with the $H_{\text{mag}} = \text{ON}$ and OFF modes have been performed on sub-samples of 100 – 250 nanorods (see fig. 53a). However, *macro spin* calculations are

possible on the full structures because the number of magnetic spins is reduced from 390,000 (number of vertices in the structure) to 4900 (number of nanorods).

All calculation modes yield the same value for the remanence, but different coercive fields (see fig. 53b). This makes it possible to obtain a correct remanence value for the full packed structure with the *macro spin* mode. However, the *macro spin* calculations overestimate the coercivity because incoherent reversal processes are neglected.

Fig. 54 summarizes the remanence and coercive fields of packed structures over a wide range of misalignment. There are more remanence values than coercivity values, because the remanence can also be obtained from the full packed structures with 4900 nanorods, whereas a correct coercivity value can only be calculated with $H_{mag} = ON$, which is limited to the sub-samples of 100 – 250 nanorods.

Both remanence and coercivity show a linearly decreasing trend with increasing misalignment σ_φ , the standard deviation of azimuthal angles φ (see fig. 54b). Plotting the same data over the mean misalignment of angles μ_φ shows no clear dependency between μ_φ and remanence and coercivity (see fig. 54a). This is the reason the standard deviation σ_φ was chosen as measure of misalignment of packed structures.

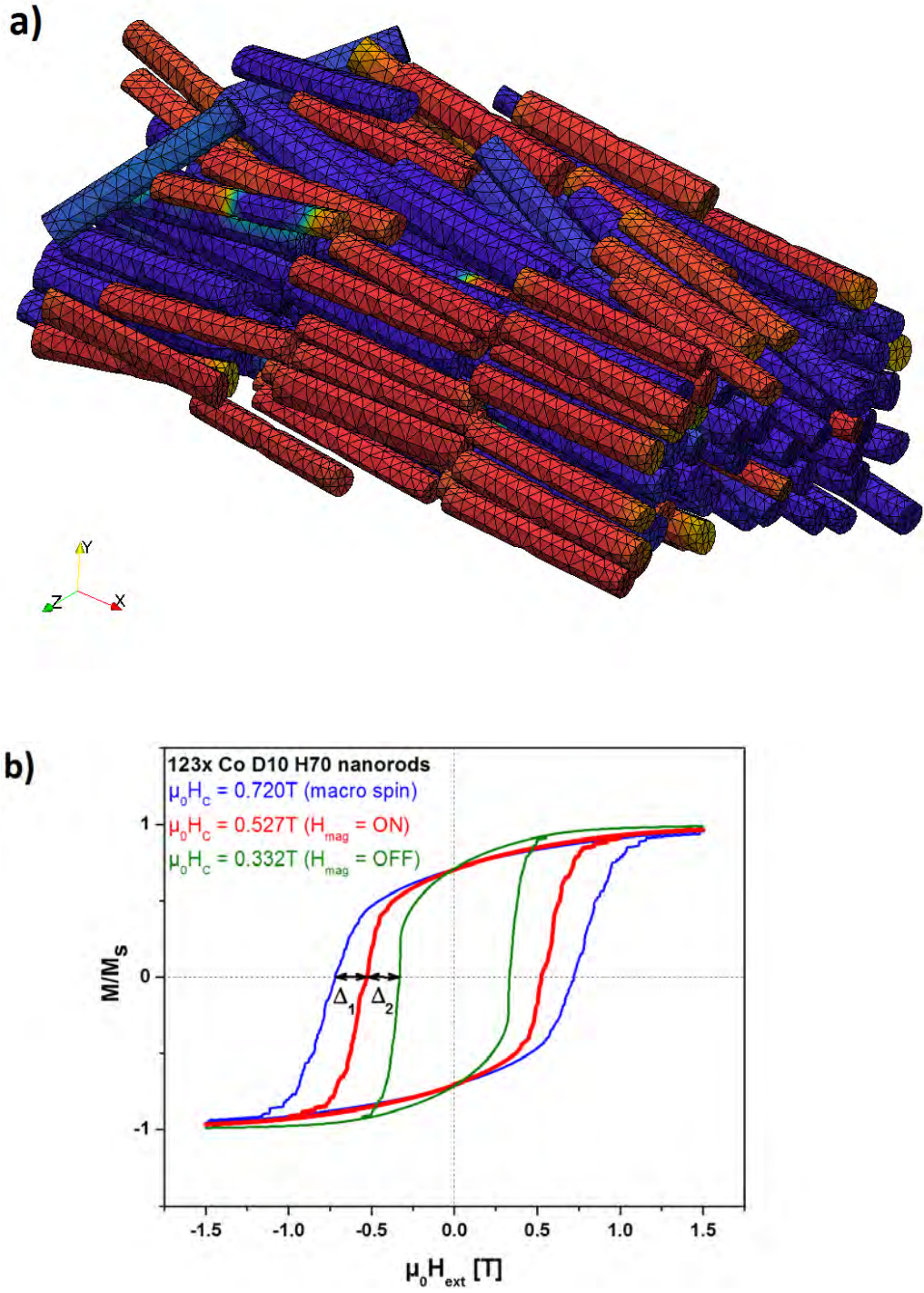


Fig. 53: a) Micromagnetic state during magnetization reversal [147]. b) Hysteresis loop of the structure shown in (a). Different calculation modes make it possible to determine the losses due to incoherent reversal processes (Δ_1) and the gain due to shape anisotropy (Δ_2) [146]

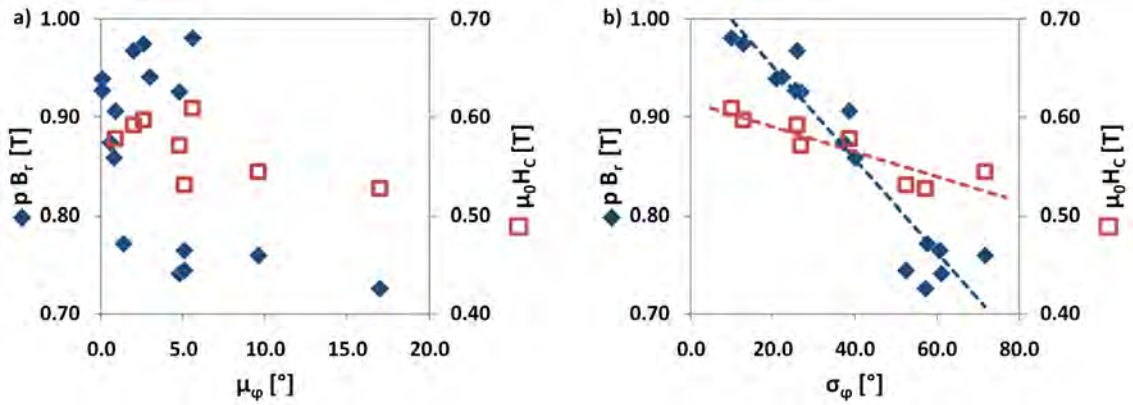


Fig. 54: Remanence and coercivity as function of (a) mean and (b) standard deviation of misalignment angles φ .

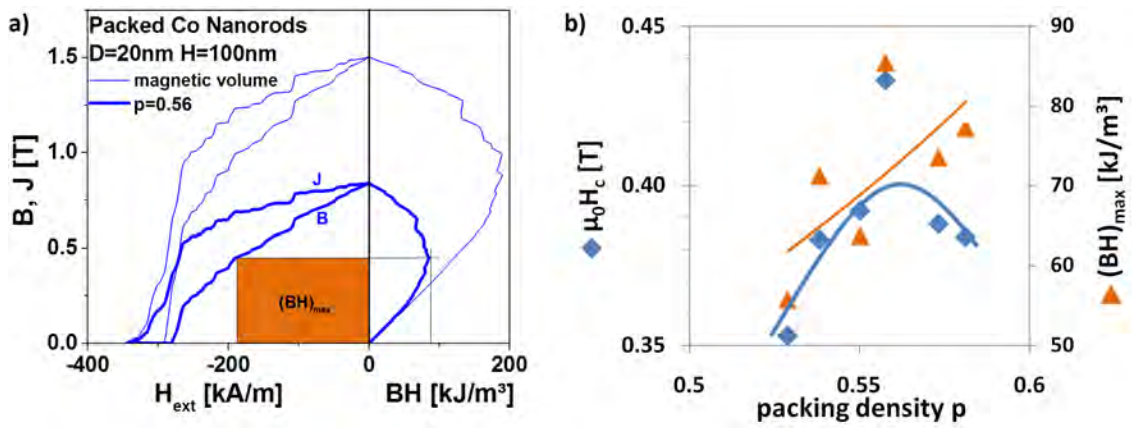


Fig. 55: a) Calculation of the exact energy density product from the demagnetization curve. b) Coercivity and energy density product of packed nanorods as function of packing density. [147]

Fig. 55a shows the exact calculation of the energy density product from the hysteresis loop. The packing density as to be considered in the calculation of the magnetic flux density: $B = \mu_0 \cdot H + p \cdot J$. Otherwise the energy density product would be severely overestimated (thin line).

The energy density product generally increases with the packing density (see fig. 55b). The outlier is a structure with very high coercivity indicating an exceptionally good alignment of the nanorods in this structure.

The coercive field peaks around packing densities $p = 0.56$. The reason are two competing factors: lower packing densities generally mean a higher misalignment of the nanorods lowering the coercivity. Higher packing densities decrease the mean

distance between the nanorods, decreasing the coercivity due to the magnetostatic interaction between the nanorods.

The simulated energy density products in the order of $80 - 100 \text{ kJ/m}^3$ are in good agreement with nanostructured permanent magnets produced by compacting dry nanorod powder [104]. A newer production technique, drying the nanorods and compacting them in an external field in a single step, produces better oriented structures with high packing density and energy density products up to 180 kJ/m^3 [114]. Because of the high orientation in coercivity in these samples, they are better described by a regular arrangement of nanorods with small misalignments discussed in section 5.2.

Experimentally produced nanorods are covered by a small layer of Co oxides. While the Co oxides are antiferromagnetic at low temperatures, they are considered non-magnetic at room temperature, because room temperature lies above the Neel-Temperature of cobalt oxides [108, 118]. The oxide layer acts as spacer between the nanorods which reduces the magnetostatic interactions between the nanorods, improving the coercivity at the cost of packing density of the ferromagnetic material. The oxide layer effectively reduces the diameter of the Co nanorods, increasing the coercivity by suppressing the vortex nucleation at the tips of the nanorods.

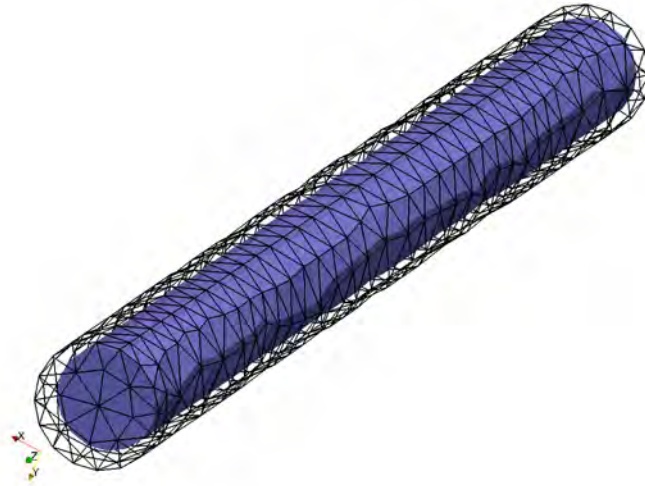


Fig. 56: Micromagnetic model of a Co nanorod covered with an oxide layer. The oxide layer is considered non-magnetic at room temperature. This leaves only the mesh of the Co core in the micromagnetic simulation.

5.4. Thermal Stability

In this chapter, the thermal stability of the nanorods is discussed. An easy approximation compares the magnetocrystalline energy stored in the particle with the thermal energy:

$$\Delta E = K_1 \cdot V = k_B \cdot T \quad (5.14)$$

If $\Delta E > 100k_B T$, the particle is considered thermally stable at temperature T , in the sense that the probability that the thermal activation alone reverses the magnetization in nanorod is negligible in all practical applications, including long-term magnetic storage [62, 131].

Micromagnetic simulations have been performed to obtain exact energy barriers for nanorods. Calculations based on the elastic band method determine the minimum energy path between two, in opposite directions fully saturated micromagnetic states. The energy barrier is the difference between the minimum and maximum energy along the path (see fig. 57).

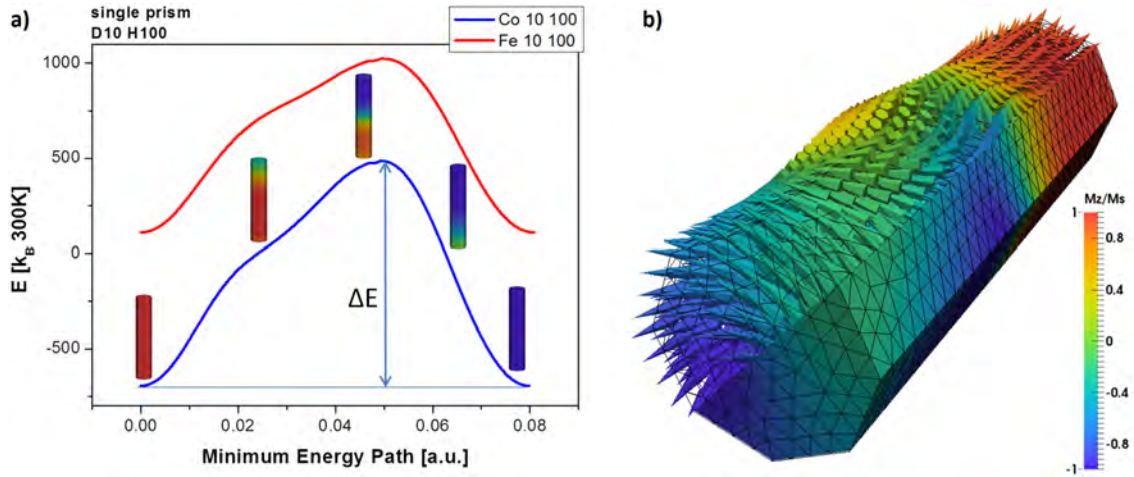


Fig. 57: a) Minimum energy path of a Co (blue) and Fe (red) *D10H100* nanorod from the fully up to the fully down saturated state. The inlays show the micromagnetic configuration of the Co nanorods along the path [131]. b) Complex thermal switching behavior of a Fe nanorod.

The energy barriers for Co and Fe nanorods with dimensions *D10H50*, *D10H100*, *D20H100* and *D30H100* are summarized in fig. 58. Both analytical approximations and micromagnetic simulations predict that the Co nanorods are thermally stable

at room temperature. The linear relationship between particle volume and energy barrier is confirmed by micromagnetic simulations.

The energy barriers for the Fe *D10* nanorods lie below the critical limit of $100k_B T$ which means that they are thermally unstable and unsuitable for hard magnetic applications. The reason is the low magnetocrystalline anisotropy compared to Co. However, the micromagnetic simulations show that the shape anisotropy increases the energy barrier as well.

The shape anisotropy contribution increases the energy barrier of Fe nanorods over the limit of $100k_B T$, making Fe nanorods thermally stable at room temperature as well. The energy barriers of both Co and Fe *D10H50* nanorods satisfy the $100k_B T$ criterion at 900K which is sufficient for most applications even at elevated temperatures (see fig 58).

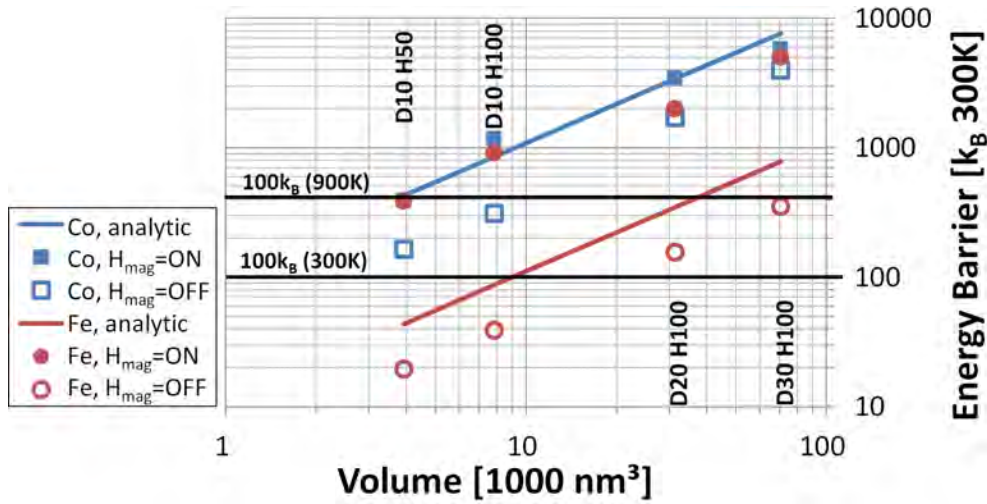


Fig. 58: Energy barriers obtained by analytical and micromagnetic simulations of Fe (red) and Co (blue) nanorods as function of volume. The difference between $H_{mag} = ON$ and OFF simulations indicate that the shape anisotropy also contributes to the thermal stability of the nanorods

5.5. Further Optimization

5.5.1. Optimizing the Nanorod Shape

Until now, we only changed dimensions in order to optimize the magnetic properties of Co nanorods, but kept the cylindrical base shape intact. The flat tip with the sharp edges at the tips of the nanorod promote the formation of vortex nucleations. The question is, how (if at all) does the shape of the nanorod tips influence the magnetic properties?

Micromagnetic simulations on a single *D15H150* have been performed. The cap was rounded by placing a perfect half-sphere on the tips with the same radius as the nanorods itself (*cap 1.0*). In addition, a model with a flatter cap has been created. In this model (*cap 0.5*) the half-sphere has been scaled down by 50% along the *z* axis before assembling it with the nanorod (see fig. 59a).

The results in fig. 59b show that the flat cap has no measurable influence on the coercivity of the nanorod. The perfect spherical cap increases the coercivity by $94mT$ or 9.7%. The round shape decreases the stray field at the tips and the nucleation forms at a higher external field. The result is the observed increase of coercivity.

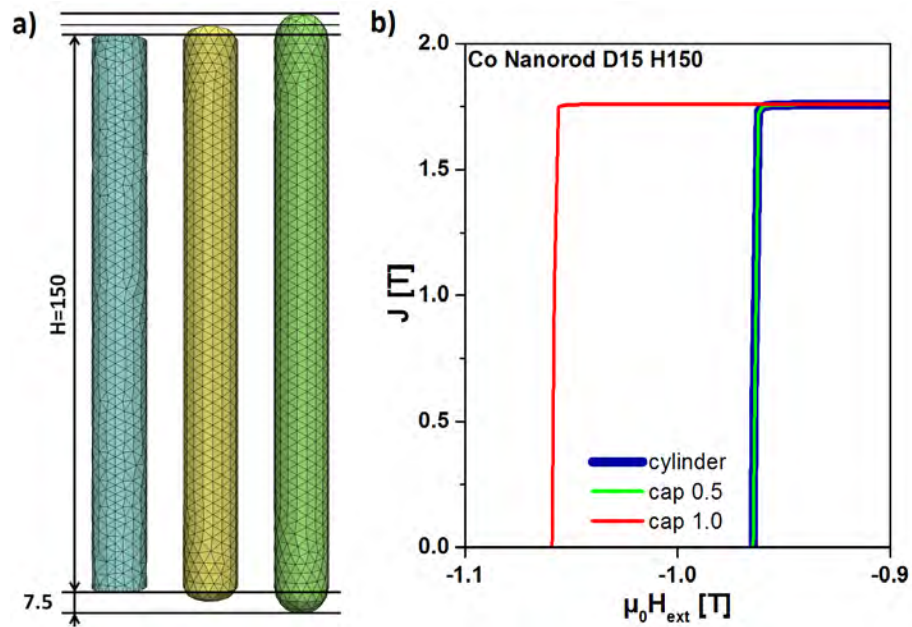


Fig. 59: a) *D15H150* nanorods without a cap, a flat rounded cap and a spherical cap. b) Section of the demagnetization curves of these three models.

The shape of the nanorods is altered by slightly tuning the experimental conditions at the crystallization process of the nanorods. Gandha et al. [120] measured a coercivity of $1.06T$ in packed nanorod structures with a mean diameter of $15nm$. This value lies above the simulated coercive field of a single, cylindrical nanorod ($0.97T$), and the misalignment and the magnetostatic interaction should further decrease the coercivity. Coercive fields above $1T$ in Co *D15* nanorods are explained with the rounded caps reducing the stray field at the tips.

5.5.2. Magnetic Hardening with Antiferromagnetic Caps

Suppressing the nucleation process at the tips of the nanorods is the key to improve coercivity. In the previous sections, the nucleation process has been suppressed by geometrical adjustments: lowering the diameter and rounding the caps of the nanorods. In this section, the nanorods will be magnetically hardened by capping the nanorods with a thin layer of an antiferromagnetic material with high uniaxial anisotropy.

As nanorod material Fe has been chosen because it is cheaper than Co and has a higher saturation polarization leading to a potentially higher energy density product [139]. As shown in fig. 39 (p. 67), the vortex state is more stable for materials with cubic anisotropy compared to uniaxial anisotropy, leading to a higher coercivity loss due to the vortex nucleation.

A wide range of materials come into question for the antiferromagnetic caps. Using an antiferromagnetic material has the additional advantage that the stray field at the tips is completely suppressed because of the zero net magnetization. The metal monoxides are interesting candidates because of the wide range of magnetocrystalline anisotropy: $K_1 = 0.5, 3.1, 27.0 MJ/m^3$ for NiO, FeO, and CoO, respectively [14, 50, 103]. $(Fe_xCo_{1-x})_3O_4$ are ferrimagnetic, but also have an interesting range of magnetocrystalline anisotropy between 0.1 and $0.4 MJ/m^3$ [12].

Micromagnetic simulations have been performed to predict the influence of the antiferromagnetic or ferrimagnetic caps on the hysteresis properties and to give guidelines about necessary capping thickness and beneficial intrinsic properties of the capping material.

5.5.2.1. Micromagnetic Model

The micromagnetic model consists of a *D20H100* iron nanorod, antiferromagnetic capping layers with varying thickness t and a $1nm$ thick interface layer where the antiferromagnetic exchange takes place. The antiferromagnetic coupling over the interface layer is calculated by a mesh-less method that adds the inter-granular exchange the surface vertices \mathbf{r}_i of the cap and the surface vertices \mathbf{r}_j with

$$E_{int,ij} \propto A_{int} \cdot |\mathbf{r}_i - \mathbf{r}_j| \quad (5.15)$$

The interface exchange is typically between 1% and 10% of the bulk exchange [74]. Detailed micromagnetic simulations have been performed on the values $A_{rel} = A_{int}/A_{NR} = -2.5\%$ and -5.0% . The negative sign indicates antiferromagnetic exchange.

The model can be used for both antiferromagnetic caps ($J_{s,cap} = 1mT$, zero saturation would lead to numerical problems) and antiferromagnetically coupled, ferrimagnetic capping layers.

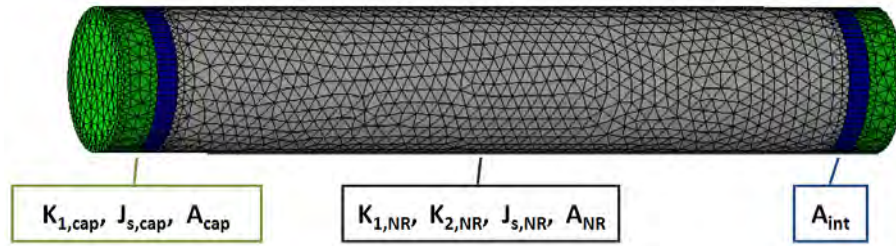


Fig. 60: Micromagnetic model of a nanorod with antiferromagnetically coupled capping layers.

5.5.2.2. Results and Discussion

Fig. 61 shows the hysteresis loop of a Fe *D20H100* nanorod with a $5nm$ thick antiferromagnetic cap with $K_{1,cap} = 100K_{1,NR} = 4600kJ/m^3$ with an interface exchange $A_{int} = -0.1A_{NR} = -2.5pJ/m$. The hysteresis loop is asymmetric or *biased*, which means that the coercive fields in positive and negative field direction (H_c^+ and H_c^-) are not equal. This behaviour is typical for antiferromagnetically coupled systems [52].

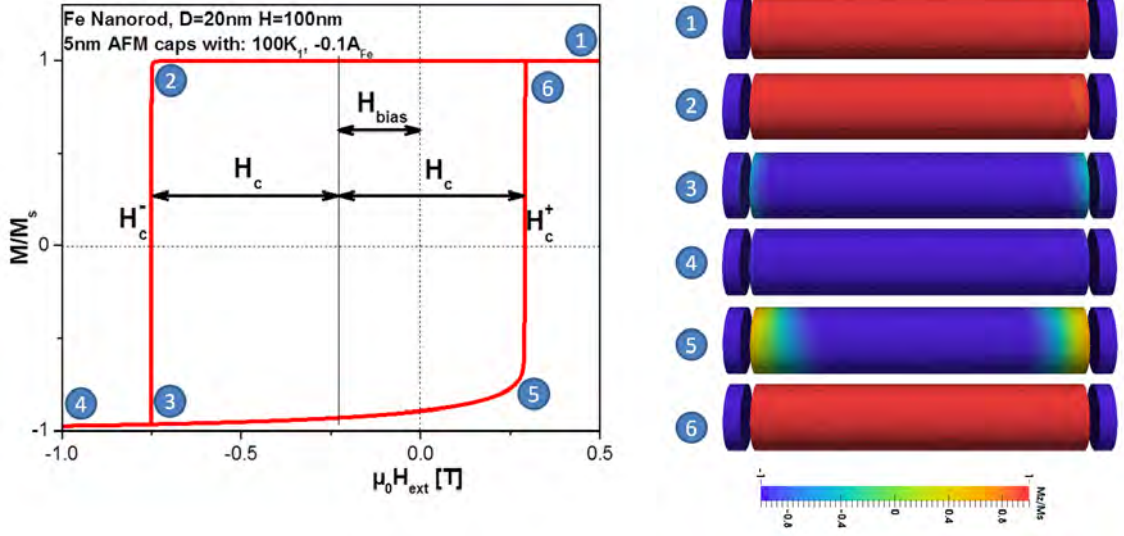


Fig. 61: Hysteresis loop of a Fe $D10H100$ nanorod with 5nm thick antiferromagnetic capping layer and micromagnetic states. The antiferromagnetic exchange introduces a bias field causing a asymmetric hysteresis loop.

The effective coercive field H_c and the bias field H_{bias} are given by

$$\begin{aligned} H_c &= \frac{H_c^+ - H_c^-}{2} \\ H_{bias} &= \frac{H_c^+ + H_c^-}{2} \end{aligned} \quad (5.16)$$

The antiferromagnetic caps suppress the nucleation at the tips of the nanorod and increase the negative coercive field from $-0.47T$ (no caps, see fig. 38, p. 65) to $-0.75T$ (fig. 61, (2)). However, the external field is not strong enough to change the configuration of the antiferromagnetic cap (4). The antiferromagnetic exchange introduces an early nucleation in the nanorod (5) causing a decrease of H_c^+ from $0.47T$ to $0.27T$. Because the gain of H_c^- outweighs the loss of H_c^+ , the effective coercivity increases from $0.47T$ to $0.51T$ or 8.5%.

Given that the intrinsic properties seem to be optimal (high $K_{1,cap}$, high A_{int}) the maximum realistically achievable coercivity increase seems to be 8.5%. However, using the same geometry and interface exchange but lowering the anisotropy of the cap to $K_{1,cap} = 10K_{1,NR} = 460\text{kJ}/\text{m}^3$ gives an unbiased hysteresis loop with

$H_c = H_c^+ = H_c^- = 0.59T$. Doubling the anisotropy constant to $K_{1,cap} = 20K_{1,NR}$ keeps the symmetric hysteresis loop intact and increases the coercivity to $0.66T$.

Fig. 62 summarized the coercivity and the exchange bias field over a wide range of interface exchange ($-A_{int}/A_{NR} = 0 \dots 0.1$) for three different anisotropy constants in the capping layer and three different cap thicknesses. The results show that at low interface exchange values the coercivity barely increases, but an exchange bias field is introduced. After a critical interface exchange is reached, the bias field becomes zero and the capped nanorods exhibit a symmetrical increase of coercivity. For the hardest examined caps ($K_{1,cap} = 100K_{1,NR} = 4600kJ/m^3$), the transition to the unbiased state could not be observed in the realistic range of interface exchange values.

A condition for the introduction of a exchange bias field is given by [52]

$$K_{1,cap} \cdot t_{cap} > J_{int} = \left| \frac{A_{int}}{a} \right| \quad (5.17)$$

where a is the lattice parameter perpendicular to the interface [69]. This means if the magnetocrystalline anisotropy energy in the capping layer is high enough to overcome the interface exchange energy, it is energetically more favorable that the magnetic spins in the nanorods and in the caps rotate independently from each other, causing the exchange bias as seen in fig. 61.

Conversely, if condition (5.17) is not fulfilled, the spins in the cap and the nanorod rotate together, causing the exchange bias field to disappear. This results in a symmetric hysteresis loop with increased coercivity.

Fig. 63 shows another view on this relation. Increasing the anisotropy in the capping layer increases the symmetric coercivity, until the capping layer becomes too hard and is decoupled from the nanorod. The previous coercivity gains are lost and an exchange bias field is introduced.

This critical point depends on the interface exchange and on the cap thickness, which means it is possible to tune the coercivity of the capped nanorods by changing the thickness of the capping layer in experiment.

With the knowledge that too hard caps can actually be harmful for the coercivity, a new way to improve templated CoFe nanowires has been developed. After electrodeposition the alumina template is removed to let the tips of the wires oxidize.

The magnetocrystalline anisotropy of the cobalt ferrites $(\text{Fe}_x\text{Co}_{1-x})_3\text{O}_4$ is in an interesting region, where it is possible to achieve symmetric coercivity increases at medium-low interface exchange. With this method the coercivity of $D20$ and $D40$ nanowires could be increased by 7% and 20%, respectively [139].

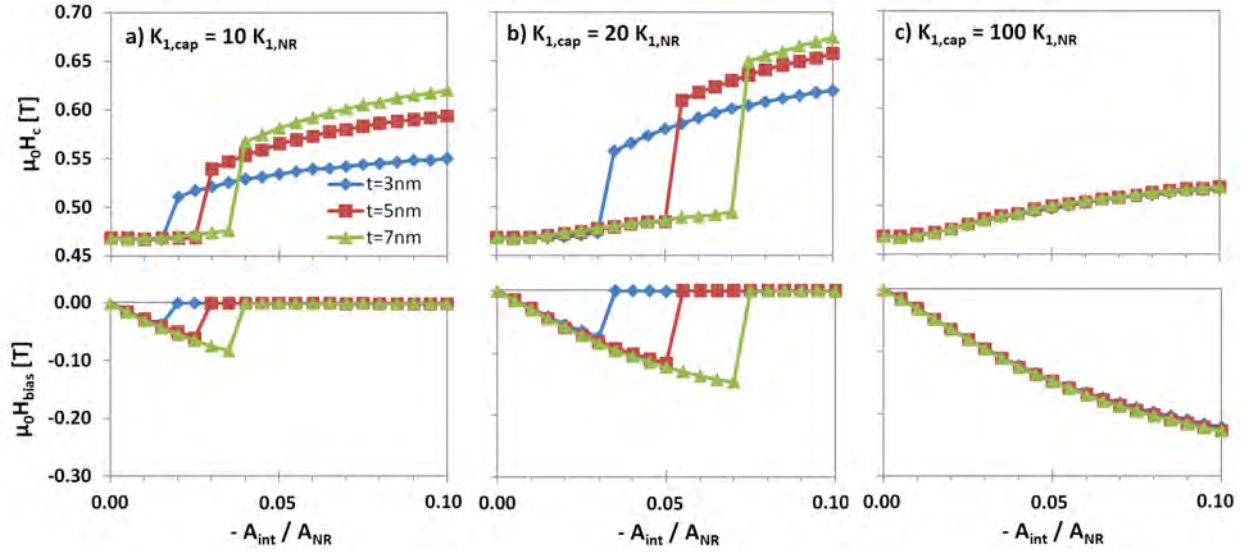


Fig. 62: Coercivity H_c and exchange bias field H_{bias} of a Fe *D20H100* nanorod with antiferromagnetically coupled caps with thickness $t = 3\text{nm}$ (blue), 5nm (red), 7nm (green) as function of the relative interface exchange $-A_{int}/A_{NR}$. The anisotropy constant $K_{1,cap}$ is (a) 10, (b) 20, (c) $100K_{1,NR}$

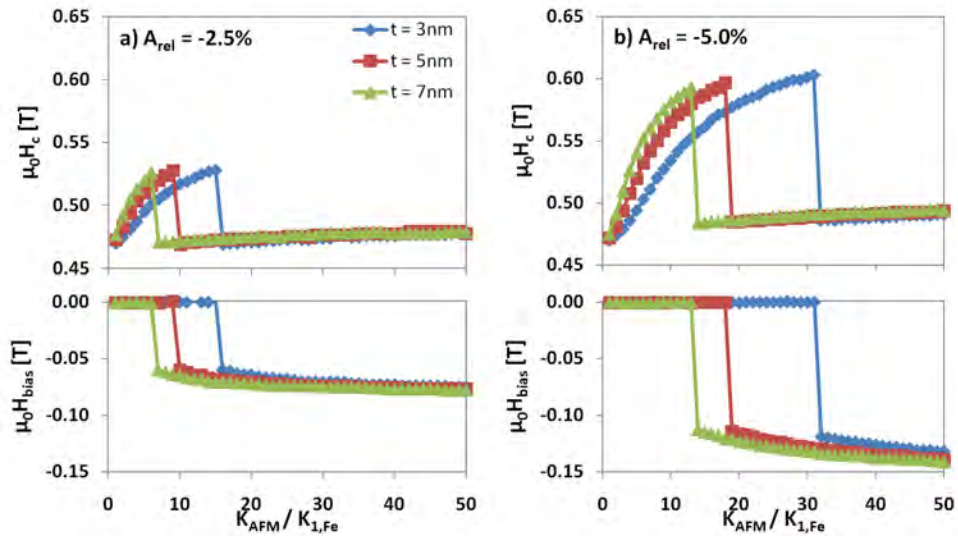


Fig. 63: Coercivity H_c and exchange bias field H_{bias} of a Fe *D20H100* nanorod with antiferromagnetically coupled caps with thickness $t = 3\text{nm}$ (blue), 5nm (red), 7nm (green) as function of the relative anisotropy constant $K_{1,cap}/K_{1,NR}$. The interface exchange constant A_{int} is (a) $-0.025A_{NR}$ and (b) $-0.050A_{NR}$

6. Conclusion

This thesis describes a multiscale modelling approach of the computational material design for novel permanent magnetic materials. It has been demonstrated that it is possible to obtain intrinsic material properties such as saturation polarization, magnetocrystalline anisotropy and exchange stiffness, which are necessary for micromagnetic simulations, with the help of density functional theory (DFT) calculations.

While it is relatively easy to get qualitative results with DFT calculations, it takes effort to achieve results with a high accuracy in order to get a good, quantitative agreement with experiments (for example the magnetocrystalline anisotropy of $(\text{Fe}_{1-x}\text{Co}_x)_2\text{B}$ alloys in section 3.3). The problem is caused by the still unknown form of the exchange-correlation energy functional $E_{xc}[\rho]$.

Improving the approximations of these functionals (local density approximation LDA, generalized gradient approximation GGA) is still a promising field of research and the most recent development are the Meta-GGA methods [70]. Until the exact form of the exchange-correlation functional is revealed, DFT calculations have to rely on experimental input for corrections in special cases (for example LDA/GGA+U [130] and fixed spin moment calculations [136])

Nevertheless, DFT calculations are a valuable tool to understand the origin of unusual material properties (e.g. MnBi calculations in section 3.2) and to give guidelines to optimize existing materials (e.g. the c/a optimization of MnBi and $(\text{Fe}_{1-x}\text{Co}_x)_2\text{B}$ alloys).

With micromagnetic simulations in the mesoscopic scale it is possible to understand the microscopic magnetic reversal mechanisms causing the macroscopically observed hysteresis loop. Although the mathematical foundation (Landau-Lifshitz-Gilbert equation, finite element method) has not changed recently, the micromagnetic simulations are not limited to qualitative predictions and are able to achieve quantitative results if the complex microstructure is taken into account in the computer model.

A major drawback of the micromagnetic simulations are the length scales. To give exact results, the finite element discretization has to be below the Bloch domain wall parameter $\delta_B = \sqrt{\frac{A}{K_1}}$ in the order of $2 - 5\text{nm}$ for hard magnetic materials. Considering typical grain sizes in sintered magnets in the order of several

micrometers, a correct, fine enough discretization takes several billion elements per grain resulting in huge computational time and memory requirements.

These restrictions force the use of simplified models which give qualitative or semi-quantitative results at best and confirm theoretical predictions with not much added value. The perfectly coupled grain structures in section 4.3.1 are an example how simplified models yield nearly the same results as the analytical Stoner-Wolfarth model.

The recent advances in nanotechnology brought the structures to a length scale where exact micromagnetic simulations are feasible. By creating models with realistically shaped grains and grain boundaries, it is possible to give quantitative results.

The micromagnetic simulations revealed that the indirect coupling of grains over para- or ferromagnetic grain boundaries is the driving factor behind Brown's paradox, that only up to 40% of the theoretical anisotropy field are realized as coercivity in real magnets (section 4.3.4).

With the help of the analysis of micromagnetic simulations it was also possible to explain how isotropic magnets exhibit higher coercive fields than oriented magnets. The analysis of the microstructural parameters α and N_{eff} revealed that the isotropic easy axis distribution does not only change the parameter α because of the higher misalignment with respect to the external field, but it also changes the structure of the demagnetizing field described by N_{eff} . The loss in coercivity due to the misalignment is compensated by the lower demagnetizing fields (section 4.3.5).

Micromagnetic simulations on the nanostructured permanent magnets followed a bottom-up approach. From the optimization of single nanorods (section 5.1), examination of the dipolar interaction between nanorods (section 5.2.1), influence of packing density in perfectly aligned nanorod matrices (section 5.2.2) to the realistically packed structures in section 5.3.

The micromagnetic simulations give guidelines for the development of nanostructured permanent magnets and for new ideas and applications, such as the hardening of iron nanorods with antiferromagnetically coupled capping layers (section 5.5.2).

The micromagnetic simulations showed that the elongated nanoparticles are an adequate way to improve coercivity, however, a significant amount of potential

energy density product is lost due to the volume fraction of the magnetic material (section 5.2.3). $\text{Nd}_2\text{Fe}_{14}\text{B}$ would perform similarly to Co in a nanorod-based structure, because the saturation polarization and packing density are the limiting factors, and not the coercivity of the structures.

In the framework of this thesis it has been demonstrated that the multi-scale approach consisting of density functional theory calculations and micromagnetic simulations gives exact quantitative predictions for intrinsic properties and the resulting macroscopically observed hysteresis properties.

A. List of Figures

1.	Multi scale modelling overview	2
2.	Characteristic points of the hysteresis loop	3
3.	Energy Density Product as Function of Coercivity	4
4.	Difference coercive and switching field	6
5.	Atomic spheres and interstitial region	11
6.	Pseudo and full potential	11
7.	bcc Fe: lattice configuration	14
8.	hcp Co: lattice configuration	15
9.	Uniaxial anisotropy constants	16
10.	Energy surfaces for cubic anisotropy	18
11.	Cubic anisotropy constants	18
12.	eg-t2g split due to crystal field	20
13.	Symmetry breaking by spin-orbit coupling	21
14.	LLG terms explained	25
15.	Example: Hat basis functions	27
16.	Example: polynomial basis functions	28
17.	Lattice parameters for MnAl	31
18.	MnBi: experimental data	35
19.	MnBi: lattice configuration	36
20.	Atomic environments in MnBi	36
21.	<i>BiMn</i> MAE over volume and c/a	40
22.	K_1 on $(\text{Fe}_{1-x}\text{Co}_x)_2\text{B}$ alloys by [22]	41
23.	Fe_2B , Co_2B : lattice configuration	41
24.	Literature and calculated lattice parameters of $(\text{Fe}_{1-x}\text{Co}_x)_2\text{B}$	45
25.	$(\text{Fe}_{1-x}\text{Co}_x)_2\text{B}$ Calculated MAE and magnetic moments	45
26.	TEM images of $\text{Nd}_2\text{Fe}_{14}\text{B}$ magnets	47
27.	Voronoi structures with regularly arranged seeding points	49
28.	Creation of grain and platelet structures	49
29.	Oriented and isotropic K_1 distribution	50
30.	Results: Grain structure without grain boundary.	52
31.	Comparison of simulation results to the Stoner-Wohlfarth model	52
32.	Results: Grain size dependence	53
33.	Results: Grain structure with different grain boundary properties	54
34.	Results: Platelet structures with and without grain boundary	56

35.	Results: Variation of K_1	59
36.	Coherent Rotation, Curling and Buckling	64
37.	Analytical Coercive Fields of Coherent Rotation and Curling	64
38.	Coercivity of Single Co, Fe and CoFe Nanorods	65
39.	Incoherent Reversal Processes in Nanorods	67
40.	Micromagnetic Simulations of Single Co Nanorods	69
41.	Finite Element Model and Coercive Field of Two Interacting Nanorods	70
42.	Coercive Field of Two Nanorods with Varying Diameter and Distance	71
43.	Calculation of Packing Density of Regular Packing	72
44.	Predicted Coercivity and Energy Density Product of Nanorod Matrices	73
45.	Model and Coercive Fields of Nanorod Matrices	74
46.	Energy Density Products of Nanorod Matrices	77
47.	Packing Algorithm	79
48.	Packing of Cylinders, Ellipsoids and Prisms	82
49.	Packing of Cylinders with a High Size Distribution	83
50.	Packing of hexagonal prisms with $D = 60nm$ and $H = 20nm$	83
51.	Evolution of Packing Density and Misalignment	84
52.	Evaluation of Packing Density	85
53.	Micromagnetic State and Hysteresis of a Packed Structure	87
54.	Remanence and Coercivity over Mean and Standard Deviation of Angles	88
55.	Energy Density Products of Packed Structures [147]	88
56.	Micromagnetic Model of a Coated Nanorod	89
57.	Minimum Energy Path and Micromagnetic States	90
58.	Energy Barriers of Fe and Co Nanorods	91
59.	Rounded Cylindrical Co Nanorods	92
60.	Micromagnetic Model of a Capped Nanorod	94
61.	Biased Hysteresis Loop and Micromagnetic States	95
62.	Variation of Antiferromagnetic Interface Exchange	98
63.	Variation of Magnetocrystalline Anisotropy in the Capping Layer . .	98

The unit cell visualizations in figures 7, 8, 17, 19, 20, and 23 have been created with the *VESTA* software package [95].

The finite element models, micromagnetic states and 3D illustrations in figures 9, 10, 13, 28, 30, 36, 39, 41, 45, 47, 48, 49, 50, 52, 53, 56, 57, 59, 60, 61 are visualized with *ParaView* [134].

B. List of Tables

1. Intrinsic Properties of Hard Magnetic Materials with Uniaxial Anisotropy	7
2. Calculated magnetocrystalline anisotropy energies for bcc Fe.	22
3. MnAl (bct): Spin moments per atom	33
4. MnAl (bct): Spin moments per orbital	33
5. MnAl (bct): Total energies and MAE	33
6. MnAl (fct): Spin moments per atom	34
7. MnAl (fct): Total energies and MAE	34
8. Spin Moments of <i>MnBi</i> at $T = 0K$ in μ_B	39
9. Orbital Moments of <i>MnBi</i> at $T = 0K$ in μ_B	39
10. Spin Moments of <i>BiMn</i> at $T = 0K$ in μ_B	39
11. Orbital Moments of <i>BiMn</i> at $T = 0K$ in μ_B	39
12. Magnetic moment and MAE of Fe_2B and Co_2B	42
13. $(Fe_{1-x}Co_x)_2B$ Literature and calculated lattice parameters	44
14. Material parameters for $Nd_2Fe_{14}B$ grain structures	48
15. Summary of Grain and Platelet Structures.	57
16. Microstructural Parameters of Grain and Platelet Structures	57
17. Theoretical Limits of Elongated Single Domain Particles	63
18. Energy Density Products of Nanorod Matrices	77

C. References

- [1] G. Voronoi. *Nouvelles applications des paramètres continus à la théorie des formes quadratiques. Deuxième mémoire. Recherches sur les paralléloèdres primitifs.* Journal für die reine und angewandte Mathematik **1908** (134), 1908. ISSN 0075-4102, 1435-5345. doi:10.1515/crll.1908.134.198.
- [2] E. Schrödinger. *An Undulatory Theory of the Mechanics of Atoms and Molecules.* Physical Review **28** (6) 1049–1070, 1926. ISSN 0031-899X. doi:10.1103/PhysRev.28.1049.
- [3] Felix Bloch. *Über die Quantenmechanik der Elektronen in Kristallgittern.* Zeitschrift für Physik **52** (7-8) 555–600, 1929. ISSN 1434-6001, 1434-601X. doi:10.1007/BF01339455.
- [4] P. A. M. Dirac. *Quantum Mechanics of Many-Electron Systems.* Proceedings of the Royal Society A: Mathematical, Physical and Engineering Sciences **123** (792) 714–733, 1929. ISSN 1364-5021, 1471-2946. doi:10.1098/rspa.1929.0094.
- [5] Lothar Nordheim. *Zur Elektronentheorie der Metalle. I.* Annalen der Physik **401** (5) 607–640, 1931. ISSN 00033804, 15213889. doi:10.1002/andp.19314010507.
- [6] Lothar Nordheim. *Zur Elektronentheorie der Metalle. II.* Annalen der Physik **401** (6) 641–678, 1931. ISSN 00033804, 15213889. doi:10.1002/andp.19314010602.
- [7] E. Wigner, F. Seitz. *On the Constitution of Metallic Sodium.* Physical Review **43** (10) 804–810, 1933. ISSN 0031-899X. doi:10.1103/PhysRev.43.804.
- [8] J. A. Osborn. *Demagnetizing Factors of the General Ellipsoid.* Physical Review **67** (11-12) 351–357, 1945. ISSN 0031-899X. doi:10.1103/PhysRev.67.351.
- [9] Edmund C Stoner, Erich Peter Wolfarth. *Interpretation of High Coercivity in Ferromagnetic Materials.* Nature **160** (4071) 650–651, 1947.
- [10] Edmund C Stoner. *Ferromagnetism: magnetization curves.* Reports on Progress in Physics **13** (1) 83–183, 1950. ISSN 00344885. doi:10.1088/0034-4885/13/1/304.
- [11] P Rhodes, G Rowlands. *Demagnetizing energies of uniformly magnetized rectangular blocks.* Proc. Leeds Phil. Liter. Soc **6** 191, 1954.
- [12] R. Bozorth, Elizabeth Tilden, Albert Williams. *Anisotropy and Magnetostriction of Some Ferrites.* Physical Review **99** (6) 1788–1798, 1955. ISSN 0031-899X, 1536-6065. doi:10.1103/PhysRev.99.1788.
- [13] E. Frei, S. Shtrikman, D. Treves. *Critical Size and Nucleation Field of Ideal Ferromagnetic Particles.* Physical Review **106** (3) 446–455, 1957. ISSN 0031-899X, 1536-6065. doi:10.1103/PhysRev.106.446.
- [14] Junjiro Kanamori. *Theory of the Magnetic Properties of Ferrous and Cobaltous Oxides, II.* Progress of Theoretical Physics **17** (2) 197–222, 1957. ISSN 0033-068X. doi:10.1143/PTP.17.197.

- [15] F. E. Luborsky, L. I. Mendelsohn, T. O. Paine. *Reproducing the Properties of Alnico Permanent Magnet Alloys with Elongated Single-Domain Cobalt-Iron Particles*. Journal of Applied Physics **28** (3) 344, 1957. ISSN 00218979. doi:10.1063/1.1722744.
- [16] A. J. J. Koch, P. Hokkeling, M. G. v. d. Steeg, K. J. de Vos. *New Material for Permanent Magnets on a Base of Mn and Al*. Journal of Applied Physics **31** (5) S75, 1960. ISSN 00218979. doi:10.1063/1.1984610.
- [17] W. Koster, E. Wachtel. *Aufbau und Magnetische Eigenschaften der Aluminium-Mangan-Legierungen mit mehr als 25-at-Prozent Mn*. Zeitschrift für Metallkunde **51** (5) 271–280, 1960.
- [18] P. Hohenberg, W. Kohn. *Inhomogeneous Electron Gas*. Physical Review **136** (3B) B864–B871, 1964. ISSN 0031-899X. doi:10.1103/PhysRev.136.B864.
- [19] W. Kohn, L. J. Sham. *Self-Consistent Equations Including Exchange and Correlation Effects*. Physical Review **140** (4A) A1133–A1138, 1965. ISSN 0031-899X, 1536-6065. doi:10.1103/PhysRev.140.A1133.
- [20] AF Andresen, W. Hälg, P. Fischer, E. Stoll. *The magnetic and crystallographic properties of MnBi studied by neutron diffraction*. Acta Chem. Scand **21** (6), 1967.
- [21] A. Holz, A. Hubert. *Wandstrukturen in dünnen magnetischen Schichten*. Z. angew. Phys **26** 145–152, 1969.
- [22] Atsushi Iga. *Magnetocrystalline Anisotropy in (Fe_{1-x}Cox)₂B System*. Japanese Journal of Applied Physics **9** (4) 415–416, 1970. ISSN 0021-4922, 1347-4065. doi:10.1143/JJAP.9.415.
- [23] Fumiko Yonezawa, Kazuo Morigaki. *Coherent Potential Approximation: Basic concepts and applications*. Progress of Theoretical Physics Supplement **53** 1–76, 1973. ISSN 0375-9687. doi:10.1143/PTPS.53.1.
- [24] Tu Chen. *Contribution to the equilibrium phase diagram of the Mn-Bi system near MnBi*. Journal of Applied Physics **45** (5) 2358, 1974. ISSN 00218979. doi:10.1063/1.1663594.
- [25] Neil W. Ashcroft, N. David Mermin. *Solid state physics*. Holt, Rinehart and Winston, New York, 1976. ISBN 978-0-03-083993-1.
- [26] H. Göbel, E. Wolfgang, H. Harms. *Properties of MnBi compounds partially substituted with Cu, Zn, Ti, Sb, and Te. II. Stability and magneto-optic properties of thin films*. Physica Status Solidi (a) **35** (1) 89–95, 1976. ISSN 00318965, 1521396X. doi:10.1002/pssa.2210350110.
- [27] A. S. Arrott, B. Heinrich, T. L. Templeton, Amikam Aharoni. *Micromagnetics of curling configurations in magnetically soft cylinders*. Journal of Applied Physics **50** (B3) 2387, 1979. ISSN 00218979. doi:10.1063/1.326961.
- [28] K.H.J. Buschow, P.G. van Engen, R. Jongebreur. *Magneto-optical properties of metallic ferromagnetic materials*. Journal of Magnetism and Magnetic Materials **38** (1) 1–22, 1983. ISSN 03048853. doi:10.1016/0304-8853(83)90097-5.

-
- [29] J. Fidler. *Analytical microscope studies of sintered Nd-Fe-B magnets*. IEEE Transactions on Magnetics **21** (5) 1955–1957, 1985. ISSN 0018-9464. doi:10.1109/TMAG.1985.1063992.
- [30] Donald Ervin Knuth, Donald Ervin Knuth. *The TeXbook*. No. A in Computers & typesetting. Addison-Wesley, Reading, Mass, 1986. ISBN 978-0-201-13447-6 978-0-201-13448-3. URL <http://www.tug.org/>.
- [31] Leslie Lamport. *LATEX: a document preparation system*. Addison-Wesley Pub. Co, Reading, Mass, 1986. ISBN 978-0-201-15790-1. URL <http://www.latex-project.org/>.
- [32] M.H. Ghandehari, J. Fidler. *Microstructural evidence for the magnetic surface hardening of Dy₂O₃-doped Nd₁₅Fe₇₇B₈ magnets*. Materials Letters **5** (7-8) 285–288, 1987. ISSN 0167577X. doi:10.1016/0167-577X(87)90112-1.
- [33] H. Kronmüller. *Theory of Nucleation Fields in Inhomogeneous Ferromagnets*. physica status solidi (b) **144** (1) 385–396, 1987. ISSN 03701972, 15213951. doi:10.1002/pssb.2221440134.
- [34] K. Adachi, S. Ogawa. *1.1.3.2.4 MBi (M = Mn, Ni)*. In H.P.J. Wijn (ed.), *Pnictides and Chalcogenides I*, vol. 27A, 180–181. Springer-Verlag, Berlin/Heidelberg, 1988. ISBN 3-540-18751-0. URL http://materials.springer.com/lb/docs/sm_lbs_978-3-540-48175-1_43.
- [35] J. Fidler, K.G. Knoch. *Electron microscopy of Nd-Fe-B based magnets*. Journal of Magnetism and Magnetic Materials **80** (1) 48–56, 1989. ISSN 03048853. doi:10.1016/0304-8853(89)90323-5.
- [36] M. Sato, Y. Ishii. *Simple and approximate expressions of demagnetizing factors of uniformly magnetized rectangular rod and cylinder*. Journal of Applied Physics **66** (2) 983, 1989. ISSN 00218979. doi:10.1063/1.343481.
- [37] Alex Zunger, S.-H. Wei, L. G. Ferreira, James E. Bernard. *Special quasirandom structures*. Physical Review Letters **65** (3) 353–356, 1990. ISSN 0031-9007. doi:10.1103/PhysRevLett.65.353.
- [38] J. F. Herbst. *R₂Fe₁₄B materials: Intrinsic properties and technological aspects*. Reviews of Modern Physics **63** (4) 819–898, 1991. ISSN 0034-6861, 1539-0756. doi:10.1103/RevModPhys.63.819.
- [39] P. Villars, L. D. Calvert. *Pearson’s handbook of crystallographic data for intermetallic phases*. ASM International, Materials Park, OH, 2nd ed edn., 1991. ISBN 978-0-87170-416-0 978-0-87170-417-7 978-0-87170-418-4 978-0-87170-419-1 978-0-87170-420-7.
- [40] John Perdew, Yue Wang. *Pair-distribution function and its coupling-constant average for the spin-polarized electron gas*. Physical Review B **46** (20) 12947–12954, 1992. ISSN 0163-1829, 1095-3795. doi:10.1103/PhysRevB.46.12947.
- [41] X C Kou, H Kronmüller. *A micromagnetic understanding of the post-annealing process in producing sintered Nd-Fe-B permanent magnets*. Journal of Physics: Condensed Matter **6** (33) 6691–6698, 1994. ISSN 0953-8984, 1361-648X. doi:10.1088/0953-8984/6/33/016.

- [42] Akimasa Sakuma. *Electronic Structure and Magnetocrystalline Anisotropy Energy of MnAl*. Journal of the Physical Society of Japan **63** (4) 1422–1428, 1994. ISSN 0031-9015, 1347-4073. doi:10.1143/JPSJ.63.1422.
- [43] J. Bauer, M. Seeger, H. Kronmüller. *Magnetic properties and microstructural analysis of rapidly quenched FeNdBGaNb permanent magnets*. Journal of Magnetism and Magnetic Materials **139** (3) 323–334, 1995. ISSN 03048853. doi:10.1016/0304-8853(95)90010-1.
- [44] H. Kronmüller. *Micromagnetism of hard magnetic nanocrystalline materials*. Nanostructured Materials **6** (1-4) 157–168, 1995. ISSN 09659773. doi:10.1016/0965-9773(95)00039-9.
- [45] C. Bradford Barber, David P. Dobkin, Hannu Huhdanpaa. *The quickhull algorithm for convex hulls*. ACM Transactions on Mathematical Software **22** (4) 469–483, 1996. ISSN 00983500. doi:10.1145/235815.235821. URL <http://www.qhull.org/>.
- [46] J. Fidler, T. Schrefl. *Overview of Nd-Fe-B magnets and coercivity (invited)*. Journal of Applied Physics **79** (8) 5029, 1996. ISSN 00218979. doi:10.1063/1.361565.
- [47] John P. Perdew, Kieron Burke, Matthias Ernzerhof. *Generalized Gradient Approximation Made Simple*. Physical Review Letters **77** (18) 3865–3868, 1996. ISSN 0031-9007, 1079-7114. doi:10.1103/PhysRevLett.77.3865.
- [48] D. Routkevitch, A.A. Tager, J. Haruyama, D. Almawlawi, M. Moskovits, J.M. Xu. *Nonlithographic nano-wire arrays: fabrication, physics, and device applications*. IEEE Transactions on Electron Devices **43** (10) 1646–1658, 1996. ISSN 00189383. doi:10.1109/16.536810.
- [49] TG Dargam, RB Capaz, Belita Koiller. *Critical analysis of the virtual crystal approximation*. Brazilian Journal of Physics **27**, 1997.
- [50] A.E. Berkowitz, Kentaro Takano. *Exchange anisotropy — a review*. Journal of Magnetism and Magnetic Materials **200** (1-3) 552–570, 1999. ISSN 03048853. doi:10.1016/S0304-8853(99)00453-9.
- [51] X. J. Liu, I. Ohnuma, R. Kainuma, K. Ishida. *Thermodynamic assessment of the Aluminum-Manganese (Al-Mn) binary phase diagram*. Journal of Phase Equilibria **20** (1) 45–56, 1999. ISSN 1054-9714, 1863-7345. doi:10.1361/105497199770335938.
- [52] J Nogués, Ivan K Schuller. *Exchange bias*. Journal of Magnetism and Magnetic Materials **192** (2) 203–232, 1999. ISSN 03048853. doi:10.1016/S0304-8853(98)00266-2.
- [53] P. Ravindran, A. Delin, P. James, B. Johansson, J. M. Wills, R. Ahuja, O. Eriksson. *Magnetic, optical, and magneto-optical properties of MnX (X=As, Sb, or Bi) from full-potential calculations*. Physical Review B **59** (24) 15680–15693, 1999. ISSN 0163-1829, 1095-3795. doi:10.1103/PhysRevB.59.15680.
- [54] Ralph Skomski, J. M. D. Coey. *Permanent magnetism*. Studies in condensed matter physics. Institute of Physics Pub, Bristol, UK ; Philadelphia, PA, 1999. ISBN 0-7503-0478-2.

- [55] Dieter Suess. *Mikromagnetische Simulation der Keimbildung in SE-Magneten*. Ph.D. thesis, Technische Universität Wien, Wien, 1999.
- [56] Tino Weinkauff, The TeXnicCenter Team. *TeXnicCenter*, 1999. URL <http://www.texniccenter.org/>.
- [57] Tan Ming-qiu, Tao Xiang-ming, Bao Shi-ning. *Ab initio study on the electronic structure and magnetism of MnAs, MnSb, and MnBi*. Chinese Physics **9** (1) 55–60, 2000. ISSN 1009-1963, 1741-4199. doi:10.1088/1009-1963/9/1/011.
- [58] D. Suss, T. Schrefl, J. Fidler. *Micromagnetics simulation of high energy density permanent magnets*. IEEE Transactions on Magnetics **36** (5) 3282–3284, 2000. ISSN 00189464. doi:10.1109/20.908770.
- [59] D. Weller, A. Moser, L. Folks, M.E. Best, Wen Lee, M.F. Toney, M. Schwickert, J.-U. Thiele, M.F. Doerner. *High K_u materials approach to 100 Gbits/in²*. IEEE Transactions on Magnetics **36** (1) 10–15, 2000. ISSN 00189464. doi:10.1109/20.824418.
- [60] Peter Blaha, Karlheinz Schwarz, Georg Madsen, Dieter Kvasnicka, Joachim Luitz. *WIEN2k, An Augmented Plane Wave + Local Orbitals Program for Calculating Crystal Properties*. Karlheinz Schwarz, TU Wien, Vienna, Austria, 2001. ISBN 3-9501031-1-2.
- [61] D J Sellmyer, M Zheng, R Skomski. *Magnetism of Fe, Co and Ni nanowires in self-assembled arrays*. Journal of Physics: Condensed Matter **13** (25) R433–R460, 2001. ISSN 0953-8984, 1361-648X. doi:10.1088/0953-8984/13/25/201.
- [62] R Dittrich, T Schrefl, D Suess, W Scholz, H Forster, J Fidler. *A path method for finding energy barriers and minimum energy paths in complex micromagnetic systems*. Journal of Magnetism and Magnetic Materials **250** 12–19, 2002. ISSN 03048853. doi:10.1016/S0304-8853(02)00388-8.
- [63] A. K. Gushchin, L. P. Kuptsov. *Green formulas - Encyclopedia of Mathematics*, 2002. URL http://www.encyclopediaofmath.org/index.php/Green_formulas.
- [64] Michiel Hazewinkel. *Encyclopaedia of mathematics*. Springer-Verlag, Berlin; New York, 2002. ISBN 978-1-4020-0609-8. URL <http://eom.springer.de/default.htm>.
- [65] V.A. Trenogin. *Galerkin method - Encyclopedia of Mathematics*, 2002. URL http://www.encyclopediaofmath.org/index.php/Galerkin_method.
- [66] Helmut Kronmüller, Manfred Fähnle. *Micromagnetism and the microstructure of ferromagnetic solids*. Cambridge studies in magnetism. Cambridge University Press, New York, 2003. ISBN 978-0-521-33135-7.
- [67] A. G. Petukhov, I. I. Mazin, L. Chioncel, A. I. Lichtenstein. *Correlated metals and the LDA + U method*. Physical Review B **67** (15), 2003. ISSN 0163-1829, 1095-3795. doi:10.1103/PhysRevB.67.153106.
- [68] Werner Scholz, Josef Fidler, Thomas Schrefl, Dieter Suess, Rok Dittrich, Hermann Forster, Vassilios Tsiantos. *Scalable parallel micromagnetic solvers for magnetic nanostructures*.

- Computational Materials Science **28** (2) 366–383, 2003. ISSN 09270256. doi:10.1016/S0927-0256(03)00119-8.
- [69] Thomas Schrefl, Dieter Suess, Werner Scholz, Hermann Forster, Vassilios Tsiantos, Josef Fidler. *Finite Element Micromagnetics*. In Timothy J. Barth, Michael Griebel, David E. Keyes, Risto M. Nieminen, Dirk Roose, Tamar Schlick, Peter Monk, Carsten Carstensen, Stefan Funken, Wolfgang Hackbusch, Ronald H. W. Hoppe (eds.), *Computational Electromagnetics*, vol. 28, 165–181. Springer Berlin Heidelberg, Berlin, Heidelberg, 2003. ISBN 978-3-540-44392-6 978-3-642-55745-3. URL http://link.springer.com/10.1007/978-3-642-55745-3_11.
- [70] Viktor N. Staroverov, Gustavo E. Scuseria, Jianmin Tao, John P. Perdew. *Comparative assessment of a new nonempirical density functional: Molecules and hydrogen-bonded complexes*. The Journal of Chemical Physics **119** (23) 12129, 2003. ISSN 00219606. doi:10.1063/1.1626543.
- [71] Guido Van Rossum, Fred L Drake. *Python language reference manual*. Network Theory Ltd., Bristol, UK, 2003. ISBN 978-0-9541617-8-1. URL <https://www.python.org/>.
- [72] Z. Zhong. *Nanowire Crossbar Arrays as Address Decoders for Integrated Nanosystems*. Science **302** (5649) 1377–1379, 2003. ISSN 0036-8075, 1095-9203. doi:10.1126/science.1090899.
- [73] Zhongmin Chen, Y.Q. Wu, M.J. Kramer, Benjamin R. Smith, Bao-Min Ma, Mei-Qing Huang. *A study on the role of Nb in melt-spun nanocrystalline Nd-Fe-B magnets*. Journal of Magnetism and Magnetic Materials **268** (1-2) 105–113, 2004. ISSN 03048853. doi:10.1016/S0304-8853(03)00481-5.
- [74] J. Nogués, J. Sort, V. Langlais, V. Skumryev, S. Suriñach, J.S. Muñoz, M.D. Baró. *Exchange bias in nanostructures*. Physics Reports **422** (3) 65–117, 2005. ISSN 03701573. doi:10.1016/j.physrep.2005.08.004.
- [75] Christine Kapfenberger, Barbara Albert, Rainer Pöttgen, Hubert Huppertz. *Structure refinements of iron borides Fe₂B and FeB*. Zeitschrift für Kristallographie **221** (5-7/2006), 2006. ISSN 0044-2968. doi:10.1524/zkri.2006.221.5-7.477.
- [76] Heather J. Kulik, Matteo Cococcioni, Damian A. Scherlis, Nicola Marzari. *Density Functional Theory in Transition-Metal Chemistry: A Self-Consistent Hubbard U Approach*. Physical Review Letters **97** (10), 2006. ISSN 0031-9007, 1079-7114. doi:10.1103/PhysRevLett.97.103001.
- [77] David J. Singh, Lars Nordström. *Planewaves, pseudopotentials, and the LAPW method*. Springer, New York, NY, 2nd ed edn., 2006. ISBN 978-0-387-28780-5 0-387-28780-9 0-387-29684-0.
- [78] Thomas Fischbacher, Matteo Franchin, Giuliano Bordinon, Hans Fangohr. *A Systematic Approach to Multiphysics Extensions of Finite-Element-Based Micromagnetic Simulations:*

- Nmag*. IEEE Transactions on Magnetism **43** (6) 2896–2898, 2007. ISSN 0018-9464. doi:10.1109/TMAG.2007.893843. URL <http://nmag.soton.ac.uk/nmag/>.
- [79] R. Gholamipour, A. Beitollahi, V.K. Marghussian, T. Ohkubo. *Cu effects on coercivity and microstructural features in nanocrystalline Nd–Fe–Co–B annealed melt-spun ribbons*. Physica B: Condensed Matter **398** (1) 51–54, 2007. ISSN 09214526. doi:10.1016/j.physb.2007.04.087.
- [80] Andre Ribes, Christian Caremoli. *Salome platform component model for numerical simulation*. In *31st Annual International Computer Software and Applications Conference, 2007*, 553–564. IEEE, 2007. ISBN 978-0-7695-2870-0. doi:10.1109/COMPSAC.2007.185. URL <http://www.salome-platform.org/>.
- [81] Ralph Skomski. *Simple models of magnetism*. Oxford University Press, Oxford ; New York, 2008. ISBN 978-0-19-857075-2.
- [82] B. D. Cullity, C. D. Graham. *Introduction to magnetic materials*. IEEE/Wiley, Hoboken, N.J., 2nd ed edn., 2009. ISBN 978-0-471-47741-9.
- [83] S P H Marashi, A Abedi, S Kaviani, S H Aboutalebi, M Rainforth, H A Davies. *Effect of melt-spinning roll speed on the nanostructure and magnetic properties of stoichiometric and near stoichiometric Nd–Fe–B alloy ribbons*. Journal of Physics D: Applied Physics **42** (11) 115410, 2009. ISSN 0022-3727, 1361-6463. doi:10.1088/0022-3727/42/11/115410.
- [84] Chris H. Rycroft. *VORO++: A three-dimensional Voronoi cell library in C++*. Chaos: An Interdisciplinary Journal of Nonlinear Science **19** (4) 041111, 2009. ISSN 10541500. doi:10.1063/1.3215722. URL <http://math.lbl.gov/voro++/>.
- [85] Yaghoub Soumare, Cécile Garcia, Thomas Maurer, Grégory Chaboussant, Frédéric Ott, Fernand Fiévet, Jean-Yves Piquemal, Guillaume Viau. *Kinetically Controlled Synthesis of Hexagonally Close-Packed Cobalt Nanorods with High Magnetic Coercivity*. Advanced Functional Materials **19** (12) 1971–1977, 2009. ISSN 1616301X, 16163028. doi:10.1002/adfm.200800822.
- [86] M. Weickhmann. *Nd-Fe-B Magnets, Properties and Applications*. Tech. Rep., Vacuumschmelze GmbH & Co. KG, Hanau, Germany, 2009. URL http://www.vacuumschmelze.com/fileadmin/documents/pdf/fipublikationen/2009/NdFeB_Magnets__Properties_and_Applications_revised_13_03_09.pdf.
- [87] B. Biskeborn, P.-O. Jubert. *Bulletpack: A Fast, Flexible Packing Algorithm for Particulate Media*. IEEE Transactions on Magnetism **46** (3) 880–885, 2010. ISSN 0018-9464. doi:10.1109/TMAG.2009.2034370. URL <http://ieeexplore.ieee.org/lpdocs/epic03/wrapper.htm?arnumber=5286318>.
- [88] J. H. Park, Y. K. Hong, S. Bae, J. J. Lee, J. Jalli, G. S. Abo, N. Neveu, S. G. Kim, C. J. Choi, J. G. Lee. *Saturation magnetization and crystalline anisotropy calculations for MnAl permanent magnet*. Journal of Applied Physics **107** (9) 09A731, 2010. ISSN 00218979. doi:10.1063/1.3337640.

- [89] R. Skomski, Y. Liu, J. E. Shield, G. C. Hadjipanayis, D. J. Sellmyer. *Permanent magnetism of dense-packed nanostructures*. Journal of Applied Physics **107** (9) 09A739, 2010. ISSN 00218979. doi:10.1063/1.3337657.
- [90] Pengpeng Yi, Min Lin, Renjie Chen, Don Lee, Aru Yan. *Enhanced magnetic properties and bending strength of hot deformed Nd-Fe-B magnets with Cu additions*. Journal of Alloys and Compounds **491** (1-2) 605–609, 2010. ISSN 09258388. doi:10.1016/j.jallcom.2009.11.016.
- [91] G. Cherubini, R. D. Cideciyan, L. Dellmann, E. Eleftheriou, W. Haeberle, J. Jelitto, V. Kartik, M. A. Lantz, S. Olcer, A. Pantazi, H. E. Rothuizen, D. Berman, W. Imaino, P.-O. Jubert, G. McClelland, P. V. Koepppe, K. Tsuruta, T. Harasawa, Y. Murata, A. Musha, H. Noguchi, H. Ohtsu, O. Shimizu, R. Suzuki. *29.5 Gb/in² Recording Areal Density on Barium Ferrite Tape*. IEEE Transactions on Magnetism **47** (1) 137–147, 2011. ISSN 0018-9464. doi:10.1109/TMAG.2010.2076797.
- [92] Oliver Gutfleisch, Matthew A. Willard, Ekkehard Brück, Christina H. Chen, S. G. Sankar, J. Ping Liu. *Magnetic Materials and Devices for the 21st Century: Stronger, Lighter, and More Energy Efficient*. Advanced Materials **23** (7) 821–842, 2011. ISSN 09359648. doi:10.1002/adma.201002180.
- [93] Pierre-Olivier Jubert, Brian Biskeborn, Diana Qiu, Ayako Matsumoto, Hitoshi Noguchi, Osamu Shimizu. *Noise and Recording Properties of Barium-Ferrite Particulate Media Studied by Micromagnetic Modeling*. IEEE Transactions on Magnetism **47** (2) 386–394, 2011. ISSN 0018-9464, 1941-0069. doi:10.1109/TMAG.2010.2091419.
- [94] Z W Liu, H Y Huang, X X Gao, H Y Yu, X C Zhong, J Zhu, D C Zeng. *Microstructure and property evolution of isotropic and anisotropic NdFeB magnets fabricated from nanocrystalline ribbons by spark plasma sintering and hot deformation*. Journal of Physics D: Applied Physics **44** (2) 025003, 2011. ISSN 0022-3727, 1361-6463. doi:10.1088/0022-3727/44/2/025003.
- [95] Koichi Momma, Fujio Izumi. *VESTA 3 for three-dimensional visualization of crystal, volumetric and morphology data*. Journal of Applied Crystallography **44** (6) 1272–1276, 2011. ISSN 0021-8898. doi:10.1107/S0021889811038970. URL <http://jp-minerals.org/vesta/en/>.
- [96] K. R. Pirota, F. Beeron, D. Zanchet, T. C. R. Rocha, D. Navas, J. Torrejoon, M. Vazquez, M. Knobel. *Magnetic and structural properties of fcc/hcp bi-crystalline multilayer Co nanowire arrays prepared by controlled electroplating*. Journal of Applied Physics **109** (8) 083919, 2011. ISSN 00218979. doi:10.1063/1.3553865.
- [97] H. Sepehri-Amin, Y. Une, T. Ohkubo, K. Hono, M. Sagawa. *Microstructure of fine-grained Nd-Fe-B sintered magnets with high coercivity*. Scripta Materialia **65** (5) 396–399, 2011. ISSN 13596462. doi:10.1016/j.scriptamat.2011.05.006.
- [98] S Sugimoto. *Current status and recent topics of rare-earth permanent magnets*. Journal of Physics D: Applied Physics **44** (6) 064001, 2011. ISSN 0022-3727, 1361-6463. doi:10.1088/0022-3727/44/6/064001.

- [99] Manuel Vázquez, Laura G. Vivas. *Magnetization reversal in Co-base nanowire arrays*. physica status solidi (b) **248** (10) 2368–2381, 2011. ISSN 03701972. doi:10.1002/pssb.201147092.
- [100] G H Yan, R J Chen, Y Ding, S Guo, Don Lee, A R Yan. *The preparation of sintered NdFeB magnet with high-coercivity and high temperature-stability*. Journal of Physics: Conference Series **266** 012052, 2011. ISSN 1742-6596. doi:10.1088/1742-6596/266/1/012052.
- [101] Erwin Coumans, Advanced Micro Devices. *Bullet Collision Detection and Physics Library*, 2012. URL <http://bulletphysics.org>.
- [102] Zoran Samardžija, Paul McGuiness, Marko Soderžnik, Spomenka Kobe, Masato Sagawa. *Microstructural and compositional characterization of terbium-doped Nd-Fe-B sintered magnets*. Materials Characterization **67** 27–33, 2012. ISSN 10445803. doi:10.1016/j.matchar.2012.02.017.
- [103] A. Schrön, C. Rödl, F. Bechstedt. *Crystalline and magnetic anisotropy of the 3d-transition metal monoxides MnO, FeO, CoO, and NiO*. Physical Review B **86** (11), 2012. ISSN 1098-0121, 1550-235X. doi:10.1103/PhysRevB.86.115134.
- [104] Kahina Ait Atmane, Fatih Zighem, Yaghoub Soumare, Mona Ibrahim, Rym Boubekri, Thomas Maurer, Jérémie Margueritat, Jean-Yves Piquemal, Frédéric Ott, Grégory Chaboussant, Frédéric Schoenstein, Nouredine Jouini, Guillaume Viau. *High temperature structural and magnetic properties of cobalt nanorods*. Journal of Solid State Chemistry **197** 297–303, 2013. ISSN 00224596. doi:10.1016/j.jssc.2012.08.009.
- [105] J. M. D. Coey. *Magnetism and magnetic materials*. Cambridge Univ. Press, Cambridge, repr edn., 2013. ISBN 978-0-521-81614-4 978-0-521-81614-4.
- [106] P. Kharel, V. R. Shah, R. Skomski, J. E. Shield, D. J. Sellmyer. *Magnetism of MnBi-Based Nanomaterials*. IEEE Transactions on Magnetism **49** (7) 3318–3321, 2013. ISSN 0018-9464, 1941-0069. doi:10.1109/TMAG.2013.2245497.
- [107] S. H. Nie, L. J. Zhu, J. Lu, D. Pan, H. L. Wang, X. Z. Yu, J. X. Xiao, J. H. Zhao. *Perpendicularly magnetized tau-MnAl (001) thin films epitaxied on GaAs*. Applied Physics Letters **102** (15) 152405, 2013. ISSN 00036951. doi:10.1063/1.4801932.
- [108] I. Panagiotopoulos, W. Fang, K. Ait-Atmane, J.-Y. Piquemal, G. Viau, F. Dalmas, F. Boué, F. Ott. *Low dipolar interactions in dense aggregates of aligned magnetic nanowires*. Journal of Applied Physics **114** (23) 233909, 2013. ISSN 00218979. doi:10.1063/1.4849076.
- [109] N V Rama Rao, A M Gabay, G C Hadjipanayis. *Anisotropic fully dense MnBi permanent magnet with high energy product and high coercivity at elevated temperatures*. Journal of Physics D: Applied Physics **46** (6) 062001, 2013. ISSN 0022-3727, 1361-6463. doi:10.1088/0022-3727/46/6/062001.
- [110] H. Sepehri-Amin, J. Liu, T. Ohkubo, K. Hioki, A. Hattori, K. Hono. *Enhancement of coercivity of hot-deformed Nd-Fe-B anisotropic magnet by low-temperature grain boundary*

- diffusion of Nd60Dy20Cu20 eutectic alloy*. Scripta Materialia **69** (9) 647–650, 2013. ISSN 13596462. doi:10.1016/j.scriptamat.2013.07.011.
- [111] L G Vivas, Yu P Ivanov, D G Trabada, M P Proenca, O Chubykalo-Fesenko, M Vázquez. *Magnetic properties of Co nanopillar arrays prepared from alumina templates*. Nanotechnology **24** (10) 105703, 2013. ISSN 0957-4484, 1361-6528. doi:10.1088/0957-4484/24/10/105703.
- [112] N.J. Yu, M.X. Pan, P.Y. Zhang, H.L. Ge. *The Origin of Coercivity Enhancement of Sintered NdFeB Magnets Prepared by Dy Addition*. Journal of Magnetism **18** (3) 235–239, 2013. ISSN 1226-1750. doi:10.4283/JMAG.2013.18.3.235.
- [113] O. C. Zienkiewicz, Robert L. Taylor, J. Z. Zhu. *The finite element method: its basis and fundamentals*. Elsevier, Butterworth-Heinemann, Amsterdam, seventh edition edn., 2013. ISBN 978-1-85617-633-0.
- [114] E. Anagnostopoulou, B. Grindi, L. M. Lacroix, F. Ott, G. Viau. *From High Aspect Ratio Nanoparticles to Nano-Structured Permanent Magnets*. In *Proceedings of the REPM2014 Workshop*, 418–420. Anapolis, USA, 2014.
- [115] Ahmad Asali, Peter Toson, Peter Blaha, Josef Fidler. *Dependence of Magnetic Anisotropy Energy on c/a Ratio of X₂Fe₁₄B (X = Y, Pr, Dy)*. IEEE Transactions on Magnetism **50** (11) 1–4, 2014. ISSN 0018-9464, 1941-0069. doi:10.1109/TMAG.2014.2326431.
- [116] S. Bance, H. Oezelt, T. Schrefl, G. Ciuta, N. M. Dempsey, D. Givord, M. Winklhofer, G. Hrkac, G. Zimanyi, O. Gutfleisch, T. G. Woodcock, T. Shoji, M. Yano, A. Kato, A. Manabe. *Influence of defect thickness on the angular dependence of coercivity in rare-earth permanent magnets*. Applied Physics Letters **104** (18) 182408, 2014. ISSN 0003-6951, 1077-3118. doi:10.1063/1.4876451.
- [117] Alexander Edström, Jonathan Chico, Adam Jakobsson, Anders Bergman, Jan Rusz. *Electronic structure and magnetic properties of L10 binary alloys*. Physical Review B **90** (1), 2014. ISSN 1098-0121, 1550-235X. doi:10.1103/PhysRevB.90.014402.
- [118] Weiqing Fang, Ioannis Panagiotopoulos, Frédéric Ott, François Boué, Kahina Ait-Atmane, Jean-Yves Piquemal, Guillaume Viau, Florent Dalmas. *Optimization of the magnetic properties of aligned Co nanowires/polymer composites for the fabrication of permanent magnets*. Journal of Nanoparticle Research **16** (2), 2014. ISSN 1388-0764, 1572-896X. doi:10.1007/s11051-014-2265-x.
- [119] J. Fidler, A. Asali, G. A. Zickler, P. Toson, M. Hajduga, T. Schrefl. *Ab-Initio and Micromagnetic Calculations on Permanent Magnets*. In *REPM 2014 - 23 Int. Workshop on Rare Earth and Future Permanent Magnets and Their Applications*, 231-235. G. Hadjipanayis (Ed.), Annapolis, USA, 2014.
- [120] Kinjal Gandha, Kevin Elkins, Narayan Poudyal, Xubo Liu, J. Ping Liu. *High Energy Product Developed from Cobalt Nanowires*. Scientific Reports **4**, 2014. ISSN 2045-2322. doi:10.1038/srep05345.

- [121] G. Hrkac, K. Butler, T. G. Woodcock, L. Saharan, T. Schrefl, O. Gutfleisch. *Modeling of Nd-Oxide Grain Boundary Phases in Nd-Fe-B Sintered Magnets*. JOM **66** (7) 1138–1143, 2014. ISSN 1047-4838, 1543-1851. doi:10.1007/s11837-014-0980-5.
- [122] Rahul Jalan. *Permanent Magnets: Technologies and Global Markets*. Tech. Rep. AVM029B, BCC Research LLC, Wellesley, MA, USA, 2014. URL <http://bccresearch.com/report/AVM029B.html>.
- [123] J S Jiang, S D Bader. *Rational design of the exchange-spring permanent magnet*. Journal of Physics: Condensed Matter **26** (6) 064214, 2014. ISSN 0953-8984, 1361-648X. doi:10.1088/0953-8984/26/6/064214.
- [124] Kurima Kobayashi, Kimiko Urushibata, Tohru Matsushita, Satoshi Sakamoto, Shunji Suzuki. *Magnetic properties and domain structures in Nd-Fe-B sintered magnets with Tb additive reacted and diffused from the sample surface*. Journal of Alloys and Compounds **615** 569–575, 2014. ISSN 09258388. doi:10.1016/j.jallcom.2014.06.170.
- [125] Teruo Kohashi, Kumi Motai, Takeshi Nishiuchi, Satoshi Hirose. *Magnetism in grain-boundary phase of a NdFeB sintered magnet studied by spin-polarized scanning electron microscopy*. Applied Physics Letters **104** (23) 232408, 2014. ISSN 0003-6951, 1077-3118. doi:10.1063/1.4883487.
- [126] Yohei Kota, Akimasa Sakuma. *Mechanism of Uniaxial Magnetocrystalline Anisotropy in Transition Metal Alloys*. Journal of the Physical Society of Japan **83** (3) 034715, 2014. ISSN 0031-9015, 1347-4073. doi:10.7566/JPSJ.83.034715.
- [127] M D Kuz'min, K P Skokov, H Jian, I Radulov, O Gutfleisch. *Towards high-performance permanent magnets without rare earths*. Journal of Physics: Condensed Matter **26** (6) 064205, 2014. ISSN 0953-8984, 1361-648X. doi:10.1088/0953-8984/26/6/064205.
- [128] Y. Murakami, T. Tanigaki, T.T. Sasaki, Y. Takeno, H.S. Park, T. Matsuda, T. Ohkubo, K. Hono, D. Shindo. *Magnetism of ultrathin intergranular boundary regions in Nd-Fe-B permanent magnets*. Acta Materialia **71** 370–379, 2014. ISSN 13596454. doi:10.1016/j.actamat.2014.03.013.
- [129] H. Sepehri-Amin, T. Ohkubo, M. Gruber, T. Schrefl, K. Hono. *Micromagnetic simulations on the grain size dependence of coercivity in anisotropic Nd-Fe-B sintered magnets*. Scripta Materialia **89** 29–32, 2014. ISSN 13596462. doi:10.1016/j.scriptamat.2014.06.020.
- [130] K. V. Shanavas, David Parker, David J. Singh. *Theoretical study on the role of dynamics on the unusual magnetic properties in MnBi*. Scientific Reports **4** 7222, 2014. ISSN 2045-2322. doi:10.1038/srep07222.
- [131] P. Toson, W. Wallisch, A. Asali, J. Fidler. *Modelling of Packed Co Nanorods for Hard Magnetic Applications*. EPJ Web of Conferences **75** 03002, 2014. ISSN 2100-014X. doi:10.1051/epjconf/20147503002.
- [132] G. A. Zickler, K. Zagar, W. Wallisch, M. Stöger-Pollach, J. Bernardi, J. Fidler. *Nanoanalytical TEM/STEM methods for the characterisation of grain boundary phases from*

- rare earth permanent magnets*. In *4th ASEM-Workshop on Advanced Electron Microscopy*. Vienna, Austria, 2014.
- [133] Ahmad Asali. *Magnetic Anisotropy Energy of Rare Earth Permanent-Magnet Alloys: A First Principle calculation*. Diplomarbeit, Technische Universität Wien, Vienna, Austria, 2015.
- [134] Utkarsh Ayachit, Lisa Sobierajski Avila. *The ParaView guide: updated for ParaView version 4.3*. Kitware Inc., 2015. ISBN 978-1-930934-29-0. URL <http://www.paraview.org/paraview-guide/>.
- [135] Markus Däne, Soo Kyung Kim, Michael P Surh, Daniel Åberg, Lorin X Benedict. *Density functional theory calculations of magnetocrystalline anisotropy energies for (Fe_{1-x}Co_x)₂B*. Journal of Physics: Condensed Matter **27** (26) 266002, 2015. ISSN 0953-8984, 1361-648X. doi:10.1088/0953-8984/27/26/266002.
- [136] A. Edström, M. Werwinski, J. Ruzs, O. Eriksson, K. P. Skokov, I. A. Radulov, S. Ener, M. D. Kuz'min, J. Hong, M. Fries, D. Yu Karpenkov, O. Gutfleisch, P. Toson, J. Fidler. *Effect of doping by 5d elements on magnetic properties of (Fe_{1-x}Co_x)₂B alloys*. arXiv:1502.05916 [cond-mat] 2015. ArXiv: 1502.05916, URL <http://arxiv.org/abs/1502.05916>.
- [137] Tae-Hoon Kim, Seong-Rae Lee, Hyo-Jun Kim, Min-Woo Lee, Tae-Suk Jang. *Simultaneous application of Dy-X (X=F or H) powder doping and dip-coating processes to Nd-Fe-B sintered magnets*. Acta Materialia **93** 95–104, 2015. ISSN 13596454. doi:10.1016/j.actamat.2015.04.019.
- [138] K. Löwe, C. Brombacher, M. Katter, O. Gutfleisch. *Temperature-dependent Dy diffusion processes in Nd-Fe-B permanent magnets*. Acta Materialia **83** 248–255, 2015. ISSN 13596454. doi:10.1016/j.actamat.2014.09.039.
- [139] S. Liebana-Vinas, R. Salikhov, C. Bran, E. Palmero, M. Vazquez, B. Arvan, X. Yao, P. Toson, J. Fidler, M. Spasova, U. Wiedwald, M. Farle. *Magnetic hardening of Fe₃₀Co₇₀ nanowires*. Nanotechnology **26** (41) 415704, 2015. ISSN 0957-4484, 1361-6528. doi:10.1088/0957-4484/26/41/415704.
- [140] P. McGuinness, O. Akdogan, A. Asali, S. Bance, F. Bittner, J. M. D. Coey, N. M. Dempsey, J. Fidler, D. Givord, O. Gutfleisch, M. Katter, D. Le Roy, S. Sanvito, T. Schrefl, L. Schultz, C. Schwöbl, M. Soderžnik, S. Šturm, P. Tozman, K. Üstüner, M. Venkatesan, T. G. Woodcock, K. Žagar, S. Kobe. *Replacement and Original Magnet Engineering Options (ROMEOS): A European Seventh Framework Project to Develop Advanced Permanent Magnets Without, or with Reduced Use of, Critical Raw Materials*. JOM **67** (6) 1306–1317, 2015. ISSN 1047-4838, 1543-1851. doi:10.1007/s11837-015-1412-x.
- [141] D. Niarchos, G. Giannopoulos, M. Gjoka, C. Sarafidis, V. Psycharis, J. Ruzs, A. Edström, O. Eriksson, P. Toson, J. Fidler, E. Anagnostopoulou, U. Sanyal, F. Ott, L.-M. Lacroix, G. Viau, C. Bran, M. Vazquez, L. Reichel, L. Schultz, S. Fähler. *Toward Rare-Earth-Free Permanent Magnets: A Combinatorial Approach Exploiting the Possibilities of Modeling*,

- Shape Anisotropy in Elongated Nanoparticles, and Combinatorial Thin-Film Approach*. JOM **67** (6) 1318–1328, 2015. ISSN 1047-4838, 1543-1851. doi:10.1007/s11837-015-1431-7.
- [142] A. K. Pathak, M. Khan, K. A. Gschneidner, R. W. McCallum, L. Zhou, K. Sun, K. W. Dennis, C. Zhou, F. E. Pinkerton, M. J. Kramer, V. K. Pecharsky. *Cerium: An Unlikely Replacement of Dysprosium in High Performance Nd-Fe-B Permanent Magnets*. Advanced Materials **27** (16) 2663–2667, 2015. ISSN 09359648. doi:10.1002/adma.201404892.
- [143] Christian Schenk. *MiKTeX*, 2015. URL <http://miktex.org/>.
- [144] P. Toson, A. Asali, G. A. Zickler, J. Fidler. *Ab-Initio Study on the Hard Magnetic Properties of MnBi*. arXiv:1508.03208 [cond-mat.mtrl-sci] 2015. URL <http://arxiv.org/abs/1508.03208>.
- [145] P. Toson, G. A. Zickler, A. Asali, J. Fidler. *Micromagnetic Modelling of Nanocrystalline Nd-Fe-B Magnets*. Journal of Magnetism and Magnetic Materials (submitted) 2015.
- [146] P. Toson, G.A. Zickler, J. Fidler. *Do micromagnetic simulations correctly predict hard magnetic hysteresis properties?* Physica B: Condensed Matter 2015. ISSN 09214526. doi:10.1016/j.physb.2015.10.013.
- [147] Peter Toson, Ahmad Asali, Wolfgang Wallisch, Gregor Zickler, Josef Fidler. *Nanostructured Hard Magnets: A Micromagnetic Study*. IEEE Transactions on Magnetics **51** (1) 1–4, 2015. ISSN 0018-9464, 1941-0069. doi:10.1109/TMAG.2014.2359093.
- [148] G. A. Zickler, P. Toson, A. Asali, J. Fidler. *Nanoanalytical TEM studies and micromagnetic modelling of Nd-Fe-B magnets*. arXiv:1510.01958 [cond-mat] 2015. URL <http://arxiv.org/abs/1510.01958>.

Danksagung

Zuerst möchte ich mich bei Prof. Thomas Schrefl für die Einführung in die mathematischen und numerischen Grundlagen der Finiten Elemente und des Mikromagnetismus bedanken. Diese haben den Grundstein meiner wissenschaftlichen Ausbildung gelegt und mich motiviert, mein Wissen weiter im Rahmen eines Doktoratsstudiums zu vertiefen.

Mein Dank gilt Prof. Josef Fidler, der mir die Möglichkeit gegeben hat, im Rahmen internationaler Projekte auf diesem Gebiet weiter zu forschen. Er war für mich Betreuer, Vorgesetzter, Mentor und Motivator.

Vielen Dank an Prof. Peter Blaha für die Einführung in die Dichtefunktionaltheorie und das geduldige Beantworten von Fragen bei Problemen mit *Wien2k*.

Bedanken möchte ich mich bei den beiden EU Projekten REFREPERMAG und ROMEO für die finanzielle Unterstützung, die es mir ermöglicht hat, an zahlreichen Projektmeetings und internationalen Konferenzen quer über Europa teilzunehmen. Am meisten hat mich beeindruckt, dass die Simulationen auf Nanoteilchen nicht nur aus rein wissenschaftlich-theoretischen Interesse durchgeführt wurden, sondern dass die Projektpartner tatsächlich nanostrukturierte Magnete herstellen können... groß genug, dass man sie sogar "begreifen" kann!

Vielen Dank an meine Kollegen für die vielen wissenschaftlichen und nicht-wissenschaftlichen Diskussionen, oder einfach nur dafür, dass sie meine aktuellen Beschwerden über nicht funktionierende Simulationen anhören mussten. Ich möchte vor allem meine langjährigen Kollegen Wolfgang Wallisch, Ahmad Asali und Gregor Zickler erwähnen... and special shout-outs to Kristina Zagar (Jozef Stefan Institut, Ljubljana)!

Mein besonderer Dank gilt meinen Eltern, die mich immer auf diesem langen Weg unterstützt haben. Ohne Euch wäre ich nicht hier.

Curriculum Vitae

Name **Peter Toson, MSc**
born November 3, 1987
in Deutschlandsberg
Citizenship Austria
Address Rotenhofgasse 21, Hof 1
 1100 Wien
 Austria

Education

1994 – 1998 VS Gleinstätten
1998 – 2002 BRG Leibnitz
2002 – 2007 HTBLA Kaindorf, Abteilung EDV und Organisation
 Electronic Data Processing and Organisation
2007 – 2010 St. Pölten University of Applied Sciences
 Bachelor Course Communications and Simulation Engineering
2010 – 2012 St. Pölten University of Applied Sciences
 Master Course Industrial Simulation
2012 – 2015 Vienna University of Technology
 Doctoral Programme Technical Physics

Publications

1. Ahmad Asali, Peter Toson, Peter Blaha, Josef Fidler. *Dependence of Magnetic Anisotropy Energy on c/a Ratio of $X_2Fe_{14}B$ ($X = Y, Pr, Dy$)*. IEEE Transactions on Magnetics **50** (11) 1–4, 2014. ISSN 0018-9464, 1941-0069. doi:10.1109/TMAG.2014.2326431.
2. P. Toson, W. Wallisch, A. Asali, J. Fidler. *Modelling of Packed Co Nanorods for Hard Magnetic Applications*. EPJ Web of Conferences **75** 03002, 2014. ISSN 2100-014X. doi:10.1051/epjconf/20147503002.
3. J. Fidler, A. Asali, G. A. Zickler, P. Toson, M. Hajduga, T. Schrefl. *Ab-Initio and Micromagnetic Calculations on Permanent Magnets. REPM 2014 - 23 Int. Workshop on Rare Earth and Future Permanent Magnets and Their Applications*, 231-235. G. Hadjipanayis (Ed.), Annapolis, USA, 2014.

4. A. Edström, M. Werwinski, J. Rusz, O. Eriksson, K. P. Skokov, I. A. Radulov, S. Ener, M. D. Kuz'min, J. Hong, M. Fries, D. Yu Karpenkov, O. Gutfleisch, P. Toson, J. Fidler. *Effect of doping by 5d elements on magnetic properties of (Fe_{1-x}Co_x)₂B alloys*. arXiv:1502.05916 [cond-mat] 2015. URL <http://arxiv.org/abs/1502.05916>.
5. D. Niarchos, G. Giannopoulos, M. Gjoka, C. Sarafidis, V. Psycharis, J. Rusz, A. Edström, O. Eriksson, Peter Toson, Josef Fidler, E. Anagnostopoulou, U. Sanyal, F. Ott, L.-M. Lacroix, G. Viau, Cristina Bran, Manuel Vazquez, L. Reichel, L. Schultz, S. Fähler. *Toward Rare-Earth-Free Permanent Magnets: A Combinatorial Approach Exploiting the Possibilities of Modeling, Shape Anisotropy in Elongated Nanoparticles, and Combinatorial Thin-Film Approach*. JOM **67** (6) 1318–1328, 2015. ISSN 1047-4838, 1543-1851. doi:10.1007/s11837-015-1431-7.
6. Peter Toson, Ahmad Asali, Wolfgang Wallisch, Gregor Zickler, Josef Fidler. *Nanostructured Hard Magnets: A Micromagnetic Study*. IEEE Transactions on Magnetism **51** (1) 1–4, 2015. ISSN 0018-9464, 1941-0069. doi:10.1109/TMAG.2014.2359093.
7. Wolfgang Wallisch, Josef Fidler, Peter Toson, Herbert Sassik, Robert Svagera, Johannes Bernardi. *Synthesis and characterisation of (Fe,Co)₂₋₃B microcrystalline alloys*. Journal of Alloys and Compounds **644** 199–204, 2015. ISSN 09258388. doi:10.1016/j.jallcom.2015.04.179.
8. Peter Toson, Ahmad Asali, Gregor A. Zickler, Josef Fidler. *Ab-Initio Study on the Hard Magnetic Properties of MnBi*. arXiv:1508.03208 [cond-mat.mtrl-sci] 2015. URL <http://arxiv.org/abs/1508.03208>.
9. G. A. Zickler, P. Toson, A. Asali, J. Fidler. *Nanoanalytical TEM studies and micromagnetic modelling of Nd-Fe-B magnets*. arXiv:1510.01958 [cond-mat] 2015. URL <http://arxiv.org/abs/1510.01958>.
10. S. Liebana-Vinas, R. Salikhov, C. Bran, E. Palmero, M. Vazquez, B. Arvan, X. Yao, P. Toson, J. Fidler, M. Spasova, U. Wiedwald, M. Farle. *Magnetic hardening of Fe₃₀Co₇₀ nanowires*. Nanotechnology **26** (41) 415704, 2015. ISSN 0957-4484, 1361-6528. doi:10.1088/0957-4484/26/41/415704.
11. P. Toson, G. A. Zickler, J. Fidler. *Do micromagnetic simulations correctly predict hard magnetic hysteresis properties?* Physica B: Condensed Matter (in press) 2015. doi:10.1016/j.physb.2015.10.013.
12. P. Toson, G. A. Zickler, A. Asali, J. Fidler. *Micromagnetic Modelling of Nanocrystalline Nd-Fe-B Magnets*. Journal of Magnetism and Magnetic Materials (submitted) 2015.

Conference Contributions

1. Joint European Magnetic Symposia (JEMS 2013), Rhodes, Greece, 25.-30.08.2013, Talk: P. Toson, A. Asali, W. Wallisch, and J. Fidler. *Simulation of hysteresis properties of realistically packed nanorod structures*
2. Joint European Magnetic Symposia (JEMS 2013), Rhodes, Greece, 25.-30.08.2013, Poster: W. Wallisch, P. Toson, A. Asali, H. Sassik, J. Fidler. *Synthesis and analysis of $(Fe, Co)_{2-3}B$ microcrystalline alloys*
3. IEEE International Magnetism Conference (Intermag 2014), Dresden, Germany, 04.-08.05.2014, Talk: P. Toson, A. Asali, J. Fidler, R. Salikhov, M. Spasova, and M. Farle. *Magnetic Hardening of Nanorods with Antiferromagnetic Caps*
4. IEEE International Magnetism Conference (Intermag 2014), Dresden, Germany, 04.-08.05.2014, Poster: A. Asali, P. Toson, P. Blaha, J. Fidler. *Dependence of Magnetic Anisotropy Energy on c/a Ratio of $X_2Fe_{14}B$ ($X = Y, Pr, Dy$)*
5. International Conferences on Modern Materials and Technologies (CIMTEC 2014), Montecatini, Italy, 15.20.06.2014, Talk: J. Fidler, A. Asali, P. Toson, G. A. Zickler, K. Zagar. *Modelling of anisotropy and coercivity in novel hard magnets*
6. 10th European Conference on Magnetic Sensors and Actuators (EMSA 2014), Vienna, Austria, 04.-09.07.2014, Poster: P. Toson, A. Asali, W. Wallisch, G. A. Zickler, and J. Fidler. *Nanostructured Hard Magnets: A Micromagnetic Study*
7. Rare Earth and Future Permanent Magnets and Their Applications Workshop (REPM2014), Annapolis, USA, 17.-21.08.2014, Invited Talk: J. Fidler, A. Asali, G. A. Zickler, P. Toson, M. Hajduga, T. Schrefl. *Ab-Initio and Micromagnetic Calculations on Permanent Magnets*
8. Materials Science Engineering (MSE 2014), Darmstadt, Germany, 23.-25.09.2014 Invited Talk: J. Fidler, A. Asali, P. Toson, W. Wallisch, G. Zickler, K. Zagar. *Advanced Hard Magnetic Materials Based on Shape and Crystal Anisotropy*
9. 59th Annual Magnetism and Magnetic Materials Conference (MMM 2014), Honolulu, Hawaii, 03.-07.11.2014, Talk: J. Fidler, A. Asali, P. Toson, G. A. Zickler, D. Süss. *Modelling of anisotropy and coercivity in $(Pr, Dy)_2Fe_{14}B$ magnets by electronic structure and micromagnetic calculations*
10. 5th Advanced Electron Microscopy ASEM Workshop (ASEM 2015), Graz, Austria, 07.-08.05.2015, Talk: G. A. Zickler, P. Toson, A. Asali, P. Tozman, M. Venkatesan, J. M. D. Coey, J. Fidler. *Microstructural TEM-analysis of novel rare earth free permanent magnets*
11. 5th Advanced Electron Microscopy ASEM Workshop (ASEM 2015), Graz, Austria, 07.-08.05.2015, Talk: W. Wallisch, P. Toson, M. Stöger-Pollach, J. Bernardi, J. Fidler. *SEM and TEM investigation for the characterization of $(Fe, Co)_{2-3}B$ alloys*

12. 10th International Symposium on Hysteresis Modeling and Micromagnetics (HMM 2015), 18.-20.05.2015, Iasi, Romania, Invited Talk: J. Fidler, G. A. Zickler, P. Toson, A. Asali. *Do Micromagnetic Simulations Correctly Predict Hard Magnetic Hysteresis Properties*
13. International Workshop of the ARISTEIA Project: Complex Magnetic Nanostructures (COMANA 2015), Agia Marina, Greece, 02.-05.06.2015, Invited Talk: J. Fidler, P. Toson, G. A. Zickler, A. Asali. *Multiscale modelling of hard magnetic nanostructures*
14. G8 Symposium on Next Generation Permanent Magnets (ESICMM 2015), Tsukuba, Japan, 18.-19.06.2015, Talk: J. Fidler, G. A. Zickler, A. Asali, P. Toson. *Nanoanalytical TEM studies and multiscale modelling of Nd-Fe-B magnets*
15. 20th International Conference on Magnetism (ICM 2015), Barcelona, Spain, 05.-10.07.2015, Poster: P. Toson, A. Asali, G. A. Zickler, and J. Fidler. *Ab-Initio Study on the Hard Magnetic Properties of MnBi*
16. 12th Multinational Congress on Microscopy (MCM 2015), Eger, Hungary, 23.-28.08.2015, Poster: G. A. Zickler, P. Toson, A. Asali, J. Bernardi, J. Fidler. *Grain boundary chemistry of heavy rare earth free Nd-Fe-B permanent magnets*